NANYANG TECHNOLOGICAL UNIVERSITY
SINGAPORE

CONVERSION OF CARBON BASED FOOD WASTES TO ELECTRODES FOR ENERGY STORAGE APPLICATIONS

MAKHAN MAHARJAN

SCHOOL OF CIVIL AND ENVIRONMENTAL ENGINEERING

2018

CONVERSION OF CARBON BASED FOOD WASTES TO ELECTRODES FOR ENERGY STORAGE APPLICATIONS

MAKHAN MAHARJAN

SCHOOL OF CIVIL AND ENVIRONMENTAL ENGINEERING

A thesis submitted to the Nanyang Technological University

in partial fulfilment of the requirement for the degree of

Doctor of Philosophy

2018

Acknowledgements

I am highly grateful to Prof Liu Yu for taking me as a student in the limited period of my PhD candidature, and for his valuable advice and support. I appreciate and express my gratitude to my Co-supervisor Dr Tuti Mariana Lim for taking me in the middle of the study period of unforeseen circumstances with hard time that led towards begin my research in the new field. I am thankful to Prof Ng Wun Jern for his kind concerns to my research status, and for the help and advice. I would also thank Assist Prof Chang Wei-Chung, Victor for his help. I would like to express my sincere gratitude to my former supervisor Assoc Prof Wang Jing-Yuan for his guidance, encouragement and support in the first two years. I did feel missing him a lot during the period of my later days. I would pray for his good health and happy productive life.

I am highly grateful to Assoc Prof Tan Swee Ngin, National Institute of Education (NIE) for providing research facilities for accomplishing my PhD Confirmation Examination (QE) related works, and advice and support. I would like to thank Dr Ge Liya in Residues & Resource Reclamation Centre (R3C) of Nanyang Environment and Water Research Institute (NEWRI) for her guidance and valuable help to get cross my QE. I also highly appreciate her for always being ready to help and for proofreading of this thesis. My appreciation and thanks also go to Assist Prof Kalun Wong, NIE for teaching me on Nitrogen sorption results analysis, and advice.

My sincere gratitude goes to Dr Mani Ulaganathan in Energy Research Institute @Nanyang Technological University (ERI@N) for his help and advice in my research.

I am grateful to thesis advisory committee (TAC) members Assoc Prof Qingyu Yan and Assist Prof Zhou Yan for their support and feedback.

My big thank to Dr Chan Wei Ping (NEWRI-R3C) for experience sharing, willingness to discuss any time, valuable suggestion and help. I am also grateful to Dr Apostolos, Giannis, Dr Hu Cheng Cheng, Dr Amy Tan Giin-Yu, Dr Yin Ke,

Dr Pan Chaozhi, Dr Lin Wenlin Yvonne and Dr Tong Huan Huan for sharing their research experiences, help and suggestions. I appreciate Dr Vanchiappan Aravindan, Dr S. Sreejith, Eldho Edison, Dr Yu Zhang, Ms Raksha Dangol for their help. My thanks also go to Mr Nyunt Wai, Mr Arjun Bhattarai, Mr Purna C. Ghimire and Ms Moe Ohnmar Oo in ERI@N for the help in VRB related experiments.

I am thankful to Ms Wong Yuet Mun (Isabelle) and Ms Lo Siew Cheng (Priscilla) in NEWRI-R3C for their cooperation. I would appreciate Mrs. Lim Chew Wang, Mrs. Maria Chong, Ms See Shen Pearlyn, Mr Tan Han Khiang and Mr Ong Chee Yung in Environment Laboratory, CEE and Dr. Ronn Goei (NEWRI-ECMC) for their cooperation in laboratory related work.

I would express my thanks to Joo Ling, Mdm Laura, PannerSelvam, Evelyn and Yi Sing for kind concerns and chats over foods.

I would gratefully acknowledge A*STAR for providing me the Singapore International Graduate Award (SINGA) for my PhD study. I would also like to take this opportunity to acknowledge the School of Civil and Envionmental Engineering (CEE), Nanyang Technological University and NEWRI-R3C for providing research facilities for my PhD study. I would thank the staff at Graduate Studies Unit, CEE and all the senior research scholars and staff at NEWRI-R3C for their cooperation and help.

Last but not least, thanks to all my family members for taking care of the house matters in my absence and for providing me the moral support, and being there all the way of this journey.

Table of Contents

Summary

The global energy demand has escalated during last few decades due to the rapid population growth, urbanization and industrialization. On the other side, continuous exploitation of non-renewable fossil fuels has raised the concerns on environmental degradation. Further, the renewable energy sources (e.g., wind, solar) are intermittent, and power cannot be necessarily generated where or when it is needed. This necessitates developing efficient energy storage systems besides energy production to help match the supply and demand.

Carbon materials have been extensively studied as electrodes for energy storage applications. However, carbon materials used as electrodes in commercial energy storage systems at present are derived from non-renewable fossil fuels. Furthermore, fossil fuels usage has environmental hazards due to the emission of greenhouse gases, such as CO_2 and CO. Thus, there is need to explore alternative carbon precursors. This will help in reducing the sole dependency on non-renewable fossil fuels as well as creating healthy environment.

Biomass is rich in carbon content, which can be used as a low cost, easily available, abundant, renewable and environmental-friendly source. Food waste is an inevitable by-product produced in different stages of the food supply chain. Fruit peels wastes as bio-waste are neglected reusable resource. In regions with large quantities of fruits production and consumption, fruit peels pose a serious disposal problem. At the same time, bio-waste offers a big potential for employing it as precursor for the production of value-added products, such as porous carbons. Previous studies have extensively explored various biomasses as precursors for preparation of activated carbon (AC). However, the studies have mainly employed plant materials or agricultural by-products for the preparation of ACs. Studies on the use of fruit peels waste as precursors are scarce. Therefore, comprehensive study is required to evaluate the potential of employing this under-utilized renewable resource for the preparation of value-added products, such as activated carbon. In addition, investigations are also needed to evaluate the electrochemical performance of the synthesized ACs as electrodes for energy storage applications, and

development of high performance energy storage devices. This has motivated to explore bio-waste fruit peels as precursor materials for energy storage applications, such as vanadium redox flow battery (VRB) and supercapacitors in this study.

This thesis is divided into four parts. In the first part, five fruit peels waste samples, namely; orange (*Citrus sinensis*) peel, lychee *(Litchi chinensis*) peel, grapefruit (*Citrus paradise*) peel, pineapple (*Ananas comosus*) peel and Thai longan (*Dimocarpus* longan) peel were screened from 11 samples based on the high carbon contents revealed from ultimate analysis, availability in abundance and also different fruit. The selected five precursor samples were subjected to proximate analysis for knowing organic and inorganic fractions, and thermogravimetric analysis (TGA) for understanding their pyrolytic characteristics. High surface area ACs were synthesized from five screened precursors by carbonization followed by chemical activation. *For the synthesis of the ACs, different approach of precursor pre-treatment at 400 ℃ for 1 h in an inert atmosphere and then KOH impregnation of the resultant char followed by pyrolysis was done. So far, this pre-treatment approach adopted has not been reported*.

The as-synthesized ACs were subjected to extensive characterizations to reveal their physico-chemical properties. The elemental composition, textural properties, morphological features, structural features, and surface chemistry of the ACs were studied by elemental analyzer, Nitrogen adsorption-desorption studies, field emission-scanning electron microscopy (FE-SEM) equipped with electron disruptive X-ray spectroscope (EDX), transmission electron microscopy (TEM), X-ray diffraction (XRD), Raman spectroscopy, Fourier transformer infrared (FT-IR) spectroscopy and X-ray photoelectron spectroscopy (XPS). Based on the obtained characterization results, such as high surface area, well developed pore structures and favourable surface features, ACs synthesized from orange peels waste and lychee peels waste were further screened for evaluating them as electrode materials for energy storage applications. Research gaps identified from literature review (limited or no published data) were also considered in selecting these two precursors.

In the second part of this study, the orange peel-derived ACs (OP-AC with BET surface area of 1901 $m^2 g^{-1}$ and OP-AC1 with BET surface area of 1916 $m^2 g^{-1}$) were evaluated by cyclic voltammetry (CV) and electrochemical impedance spectra (EIS) studies for VRB applications. The OP-AC was studied for VRB static cell. The OP-AC1 was further subjected to simple surface modification for studying the influence of oxygen-containing surface functional groups on electrochemical performance using the surface modified OP-AC1 (T-OP-AC) for VRB applications. CV results showed that OP-AC, OP-AC1 and the T-OP-AC modified electrodes demonstrate improved electrocatalytic activity in both positive and negative side redox couples compared with the pristine bipolar plate electrode. The improved electrode activities are attributed to the high surface area of the ACs, which provide effective electrode area and better contact between the porous electrode and bipolar plate. Consequently, the performance of VRB in a static cell shows higher energy efficiency for OP-AC electrode than the pristine electrode at all current densities studied. Similarly, improvements in the electrochemical activity were observed for T-OP-AC electrode in both redox couples compared to pristine graphite and OP-AC1 electrodes. The electrochemical kinetics of the redox reactions were in the order of T-OP-AC > OP-AC1 > pristine graphite. The findings indicate that the oxygen functionalities facilitate the charge transfer processes by providing more active sites and improving the wettability of the electrode. The results suggest the OP-ACs to be promising electrodes for VRB applications, and they can be incorporated into making conducting plastics electrode to lower the VRB cell stack weight and cost.

In the third part of study, the OP-AC was evaluated for its application for fabrication of high specific energy lithium ion capacitors (LICs). The fabricated LIC using the porous OP-AC with pre-lithiated graphite (LiC_6) delivered specific energy of ~106 Wh kg^{-1}. In addition, LIC configuration with $Li_4Ti_5O_{12}$ was also fabricated and observed to be capable of delivering the specific energy of ~35 Wh kg^{-1}. Symmetric configurations of OP-AC with aqueous and organic solutions were also fabricated for comparison purpose. A systematic improvement from the specific energy of ~8 to 106 Wh kg^{-1} is noted from aqueous to LIC assembly. *For the first time, the fabrication of whole LIC assembly using OP-AC (i.e., OP-AC) to deliver*

high energy is reported. The calculated capacitance for the assembly is 112.5 F g^{-1}, which is more than twice that previously reported (51.7 F g^{-1})

In the fourth part of study, Lychee peels waste derived porous carbon (LP-AC) with BET surface area of 1601 m^2 g^{-1} was evaluated for the energy storage applications. *For the first time, LP-AC was evaluated as electrode for supercapacitors in both symmetric and asymmetric cell configurations in aqueous electrolyte.* The assembled symmetric cell configuration (Gr/PANI||LP-AC) delivered high specific energy of about 9.4 Wh kg^{-1}. The specific energy was further increased to ~50.0 Wh kg^{-1} in an asymmetric cell assembly in which LP-AC and graphene/polyaniline (Gr/PANI) composite were used as negative and positive electrodes, respectively. The asymmetric cell also exhibited good cycling stability with ~88% of the initial specific capacitance retained after 5000 cycles.

To sum up, this study successfully demonstrated the feasibility of converting selected five fruit peels waste to porous carbons, and OP-ACs (OP-AC and OP-AC1) and LP-AC as promising electrodes for energy storage applications. For the first time, this study evaluated performance of the OP-ACs and the T-OP-AC modified electrodes for VRB applications. The fabrication of whole LIC assembly using bio-waste derived AC (OP-AC) to deliver high energy was also reported for the first time. *For the first time, the porous AC synthesized from lychee peel was reported as pseudo-capacitive electrode for aqueous supercapacitors.* The utilization of these renewable resources contributes not only in waste management but also provides value-added products for promising applications, and contributes in reducing sole dependency on fossil fuels for energy.

List of Publications

Journals

First Author:

[1] **M. Maharjan**, A. Bhattarai, M. Ulaganathan, N. Wai, M.O. Oo, J.-Y. Wang, T.M. Lim, High surface area bio-waste based carbon as a superior electrode for vanadium redox flow battery, Journal of Power Sources 362 (2017) 50-56.

[2] **M. Maharjan**, M. Ulaganathan, V. Aravindan, S. Sreejith, Q. Yan, S. Madhavi, J.-Y. Wang, T.M. Lim, Fabrication of High Energy Li–Ion Capacitors from Orange Peel Derived Porous Carbon, Chemistry Select 2(18) (2017) 5051-5058.

[3] **M. Maharjan**, Y. Zhang, M. Ulaganathan, T. M. Lim, Improved electrocatalytic activity via facile surface modification of waste derived activated carbon as electrodes for all vanadium redox flow battery, Applied Surface Science, under review.

[4] **M. Maharjan**, M. Ulaganathan, T. M. Lim, High surface area activated carbon for high energy aqueous supercapacitor, ACS Applied Energy Materials, under review.

Co-Authorship:

[1] M. Ulaganathan, **M. Maharjan**, Q. Yan, V. Aravindan, S. Madhavi, β-$Co(OH)_2$ Nanosheets: A Superior Pseudocapacitive Electrode for High-Energy Supercapacitors, Chemistry – An Asian Journal 12 (2017) 2127-2133.

Conferences

[1] **M. Maharjan**, M. Ulaganathan, V. Aravindan, S. Sreejith, Q. Yan, S. Madhavi, J.-Y. Wang, and T. M. Lim. High Performance Lithium Ion Capacitors from Bio-Waste Derived Activated Carbon, ICEST 2017: 19^{th} International Conference on Energy Systems and Technologies 7-8 June 2017, San Francisco, USA (Oral presentation).

List of Tables

List of Figures

Abbreviations

AC	activated carbon
APS	ammonium persulfate
BET	Brunauer−Emmett−Teller
CE	coulombic efficiency
CV	cyclic voltammetry
DFT	Density functional theory
DMC	di-methyl carbonate
EDL	electric double layer
EDLC	electrochemical double-layer capacitor
EDX	electron disruptive X-ray spectroscope
EC	ethylene carbonate
EE	energy efficiency
EIS	electrochemical impedance spectrometry
FC	fixed carbon
FE-SEM	field emission scanning - electron microscope
FTIR	Fourier transform infrared
GCD	galvanostatic charge-discharge
GO	graphene oxide
GP	grapefruit peel powder
GP-AC	grapefruit peel derived activated carbon
HCl	hydrochloric acid
iR	internal resistance
IR	infrared
LIC	lithium ion capacitor
$LiPF_6$	lithium hexafluorophosphate
LiC_6	pre-lithiated graphite
LP	lychee peel powder
LTO	lithium titanium oxide
LP-AC	lychee peel derived activated carbon
NMP	N-Methyl-2-pyrrolidone
OCV	open-circuit voltage

OP	orange peel powder
OPC	orange peel derived char
OP-AC	orange peel waste derived porous carbon prepared from pyrolysis with OPC:KOH = 1:2
OP-AC1	orange peel waste derived porous carbon prepared from pyrolysis with OPC:KOH = 1:1.5
PANI	polyaniline
PP	pineapple peel powder
PP-AC	pineapple peel derived activated carbon
PSD	pore size distribution
PVDF	polyvinylidene fluoride
RFB	redox flow battery
RT	room temperature
SOC	state of charge
TAB-2	teflonized acetylene black
TEM	Transmission electron microscope
TGA	thermogravimetric analysis
T-OP-AC	surface modified OP-AC1
TP	Thai longan peel powder
TP-AC	Thai longan peel derived activated carbon
VM	volatile matter
VRB	vanadium redox flow battery
VE	voltage efficiency
S_{BET}	Brunauere-Emmette-Teller (BET) surface area
S_{meso}	mesopore surface area
S_{micro}	micropore surface area
V_{micro}	micro pore volume
V_T	total pore volume
XPS	X−ray photoelectron spectroscope
XRD	X−ray powder diffraction

CHAPTER 1

Introduction

1.1 Background

The global energy demand has been considerably increased during last few decades due to the rapid population growth, urbanization and industrialization. In recent years, the global concerns on depleting non-renewable fossil fuels and increasing environmental degradation have raised the need for searching renewable resources and adopting 'green' approaches. As a result, researchers all over the world have made tremendous efforts in search of alternative clean energy sources. Notably, power is not necessarily generated where or when it is needed. Further, the renewable energy sources (e.g., wind, solar) are intermittent, which are less reliable and are likely to create fluctuation in electricity generation. This has necessitates the energy storage systems besides energy production to help match the supply and demand. Therefore, there is need of efficient energy storage systems. In this regard, sustainable energy resources and efficient energy storage systems are amongst the key challenges recognized in the 21st century.

Activated carbon (AC) has been extensively studied as electrode material for energy storage applications. However, electrodes used in energy storage devices at present are mainly obtained from non-renewable resources, such as petroleum coke, coal, pitch, peat, etc. Biomass is renewable and rich in carbon content, and has drawn huge attention for AC preparation for various applications in recent years. Researchers have investigated various biomass as carbon source for producing ACs via various synthesis routes [1-7] and their use as electrodes in energy storage applications [8-13].

Food waste is an inevitable by-product in the different stages of the food supply chain, such as production, postharvest handling, processing, distribution and consumption. Food waste is expected to increase with time due to economic growth

and increase in population. More importantly, food wastes are primarily organic with high moisture content and tend to decay rapidly under ambient conditions [14]. Therefore, there exists a real challenge in management of this reusable resource. Currently, common management or treatment methods adopted for food waste are landfill, incineration, anaerobic fermentation and composting [15, 16]. However, these conventional treatment processes are not sound waste management routes due to energy-intensive, large foot print or environmental concerns.

Fruit peels derived bio-waste is under-utilized resource, which is renewable, low cost and eco-friendly. In regions with large quantities of fruits production and consumption, fruit peels pose a serious disposal problem. If this resource can be tapped for producing carbon materials as electrodes for energy storage applications, it will not only offer value-added product for promising applications, but also contribute in waste management. However, publications on the use of fruit peels waste derived AC as electrodes in energy storage applications are scarce [13, 17]. So far, fruit peels derived AC has not been investigated as electrodes in any flow battery applications. Studies are higher demanded to evaluate the potential of employing this resource as electrode for energy storage applications. This has motivated to explore bio-waste fruit peels as precursor materials for energy storage applications (supercapacitors and vanadium redox flow battery, VRB) in this study.

1.2 Objectives and scope of the study

The utilization of renewable bio-waste as an alternative precursor for producing value-added materials, and further employing the resultant products as electrode material for energy storage applications will contribute not only in waste management but also help reduce the use of limited fossil fuel reserves and environmental pollution. The general objective of this study was to evaluate the feasibility of utilizing low cost, renewable and environmental-friendly bio-waste as an alternative electrode material for energy storage applications. To achieve this goal, the following works have been carried out.

1. Synthesis and characterization of porous carbons from bio-waste for applications as electrode material for energy storage,

2. Evaluation of bio-waste derived porous carbons as electrode and improvement of electrochemical performance for VRB applications, and

3. Evaluation of the performance of the bio-waste derived porous carbon as electrode for capacitors applications.

This study consists of four parts. In the first part of this study, high surface area ACs were synthesized from the selected bio-waste precursors *via* chemical activation. The as-synthesized ACs were subjected to different characterization studies for physico-chemical properties. In the second part of this study, two synthesized ACs were evaluated for VRB applications. VRB is one of the redox flow batteries considered as a promising energy storage system. Further improvement of the electrochemical performance of the as-synthesized AC for VRB application was successfully demonstrated via simple surface modification. In the third part of study, the as-synthesized AC was evaluated for its application for capacitors, and improvement of the specific energy was achieved through fabrication of various capacitors. In the fourth part of study, one of the bio-waste derived ACs was employed for fabrication of high performance novel pseudo-capacitive electrode for aqueous supercapacitor applications.

The outline of scopes of this work determined based on the objectives proposed are provided below.

i. Synthesis and characterization of ACs from bio-waste for application as electrode material for energy storage.

    a. To utilize unrecognized renewable resource, bio-waste as precursors for preparation of value-added product, i.e., ACs.

    b. To extensively investigate the physico-chemical properties of the as-synthesized ACs aiming to know the practicality for using as electrode for energy storage applications.

ii. Evaluation of bio-waste derived ACs as electrodes and improvement of electrochemical performance for VRB applications.

a. To evaluate the performance of the bio-waste derived as-synthesized ACs as electrodes for VRB applications.

b. To modify surface chemistry of the as-synthesized AC and demonstrate improved electrochemical performance of the surface modified carbon as electrodes for VRB applications.

iii. Fabrication of high energy capacitors from the bio-waste derived as-synthesized AC.

a. To evaluate the performance of the bio-waste derived as-synthesized AC as electrode material for various capacitors configurations.

b. To fabricate high energy capacitors using the as-synthesized AC as electrode material.

iv. Fabrication of high performance capacitors from the bio-waste derived as-synthesized AC.

a. To evaluate the performance of the bio-waste derived as-synthesized AC as novel electrode material for aqueous capacitors.

b. To fabricate bio-waste derived AC based novel pseudo-capacitive electrode for aqueous supercapacitor applications.

1.3 Thesis structure

This thesis consists of eight chapters as stated below.

Chapter 1 provides a brief background, knowledge gap, research motivation, objectives and scopes, and organization of the thesis.

Chapter 2 provides literature review related to various processes used for preparation of AC, energy storage technologies and biomass as a carbon resource for energy storage applications.

Chapter 3 describes materials and methods generally used in the experiments throughout this study.

Chapter 4 presents the material characterization results of the bio-waste samples to screen the precursors for the synthesis of ACs, and characterization results of the as-synthesized ACs to help screen the ACs for further studies related to energy storage applications.

Chapter 5 provides the synthesis of ACs from orange peel waste, characterization results and the use of orange peel derived porous carbon as superior electrode for VRB application. Additionally, improved electrocatalytic activity of the synthesized carbon via its surface modification as electrodes for VRB applications is demonstrated.

In **Chapter 6**, fabrication of high performance capacitors employing orange peel derived porous carbon electrode material is presented.

Chapter 7 presents the synthesis of high surface area AC from lychee peel waste as a novel precursor for energy storage applications. Physico-chemical properties and electrochemical performance of lychee peel derived porous carbon as pseudo-capacitive electrode for aqueous supercapacitor applications are demonstrated.

Finally, **Chapter 8** summarizes the major findings from this study. Some suggestions on synthesis of porous carbon for improved textural properties and its applications for energy storage are recommended for future studies.

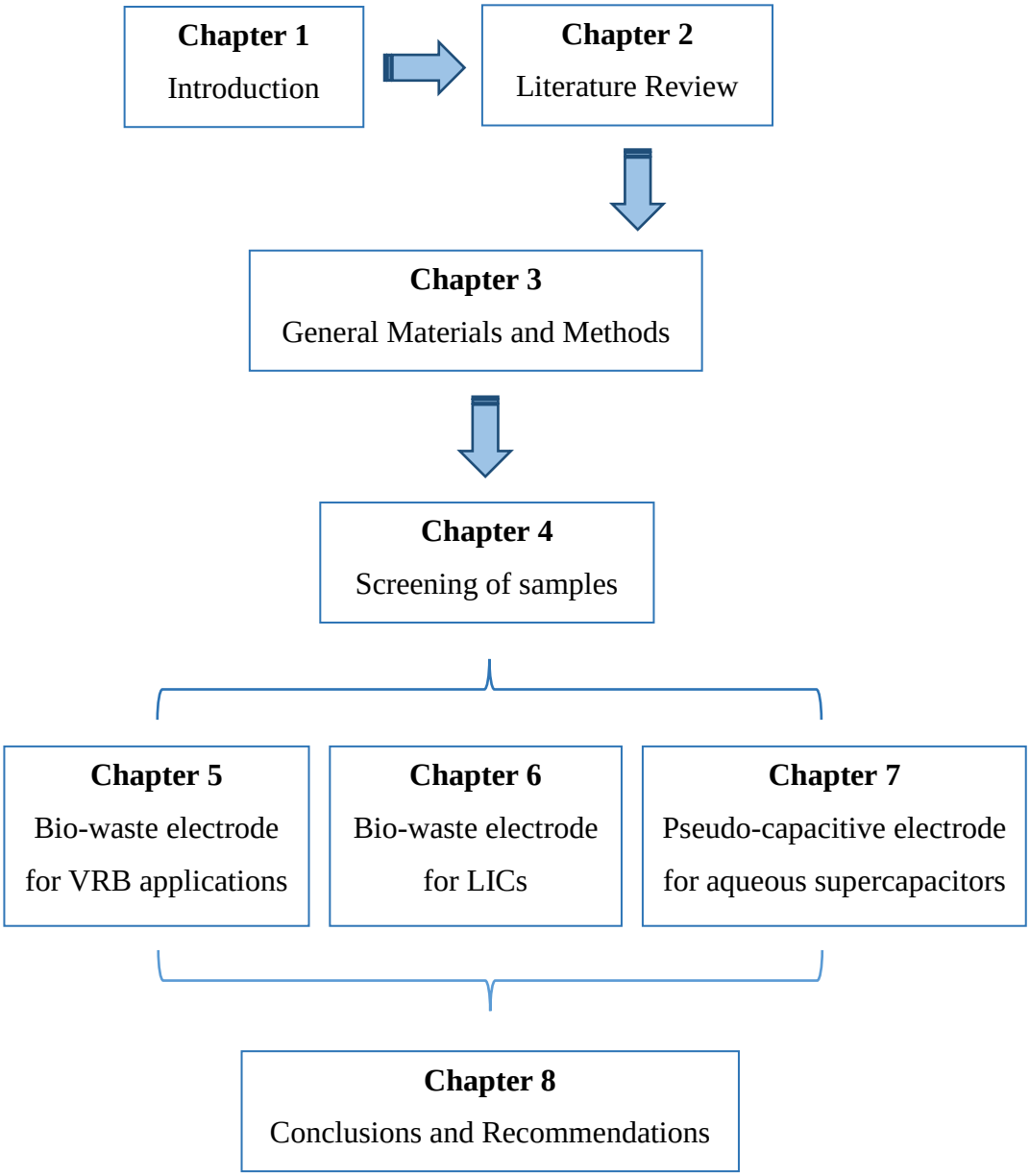

Figure 1.1. Schematic flow-chart showing structure and flow of this thesis.

CHAPTER 2

Literature Review

This chapter provides a summary of existing studies and ongoing research progress related to energy storage or conversion devices, carbon materials, and their use for energy storage applications. General introduction and comprehensive review of carbon materials with focus on biomass as sustainable precursor for synthesis of AC, and its use as electrode for vanadium redox flow battery (VRB) under redox flow batteries and supercapacitors are discussed. Based on the findings from existing literature, research gaps and current issues are summarized and specified.

2.1 Background

The world today is confronted with ever-increasing energy demand due to population growth, rapid urbanization and industrialization. Whilst, growing concerns on environmental pollution necessitate optimization of resources usage, exploring renewable resources and developing environmental-friendly technologies. The conventional energy resources (wind, solar, *etc*) are difficult to harness all the time. More importantly, these resources cannot deliver energy where and when the energy is needed. On the other hand, non-renewable sources (fossil fuels) are limited and depleting due to continuous extensive exploitation. Additionally, fossil fuels usage have growing concerns related to environmental hazards or global warming due to the emission of CO_2 and CO from the combustion of these fuels. In this perspective, there is need to find alternative sustainable eco-friendly energy resources or develop clean energy sources. This problem can be solved by exploring renewable carbon sources and developing efficient electrical energy storage devices that facilitate usage of power. Subsequently, this will help reduce the sole dependency on non-renewable fossil fuels and also contribute in creating healthy environment.

2.2 Energy storage technologies

There are different energy storage devices, such as supercapacitors, Li-ion batteries or Na-ion batteries, redox flow batteries, fuel cells, hydrogen energy storage system, and so on. In recent years, research works on energy have been focusing on exploring renewable energy resources, enhancing the efficiency of existing energy systems and developing novel energy storage technologies. Among various energy storage technologies, research interests on VRB, supercapacitors and lithium ion capacitors are growing.

2.3 Redox flow batteries

The redox flow battery (RFB) is an electrochemical system designed for energy storage which stores energy in two solutions consisting of different redox couples [18]. In RFB, the electrolytes stored in two tanks are circulated with the help of pumps. A typical electrochemical cell stack consists many cells, which are arranged in series or parallel so as to connect inert electrodes during reaction. Each cell comprises an anode and a cathode separated by an ion exchange membrane capable

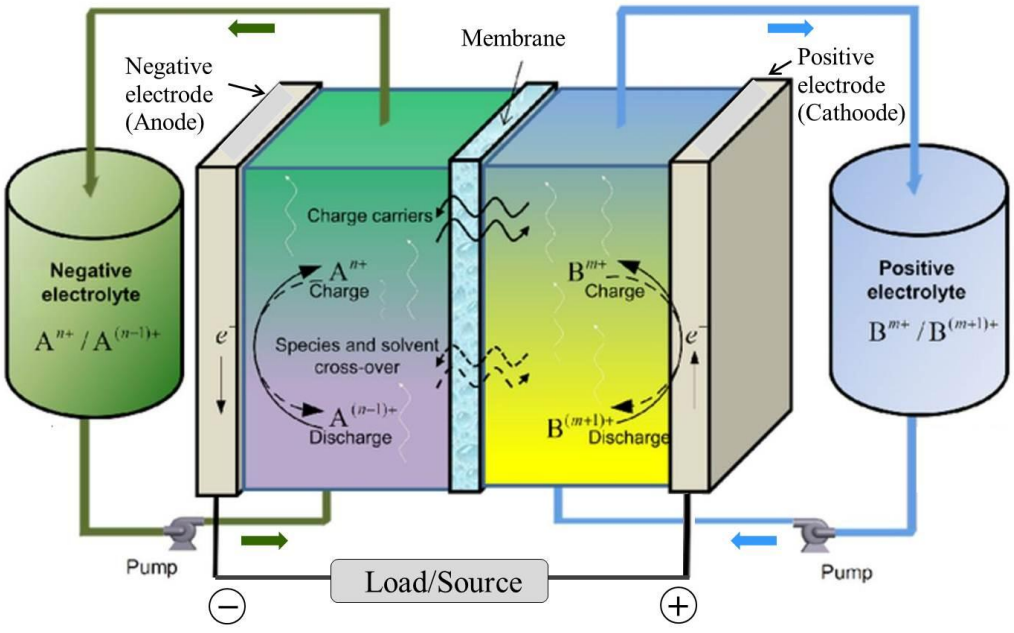

Figure 2.1. Schematic diagram of a typical redox flow battery (modified from Ref. [19]).

for diffusion of ions across it while preventing the electrolyte solutions to get cross-mixed [19]. RFBs offer many technical advantages compared with other energy storage technologies such as high energy efficiency, low capital cost and good life cycle [20]. Figure 2.1 shows schematic of a typical RFB. Comparisons of performance characteristics for various redox flow batteries are presented in Table 2.1.

Table 2.1. Comparisons of performance characteristics for various redox flow batteries (modified from Ref. [21]).

Flow cell type	Efficiency full cycle (%)	Operating temperature (°C)	Cycle life (charge/discharge)	Voltage (V)
Zn-Br	75	RT	2000	1.8
Zn-Ce	75	RT	–	2.3
PS-Br	60–75	RT	2000	1.5
Na-S	89–92	≈300	2500 +	2.0
Lead	85	RT	500–800	2.1
VRB	70–85	RT	>200 000	1.4 (50% SOC[a])
				1.6 (100% SOC)

[a]State of charge (SOC)

RT = room temperature

2.3.1 Vanadium redox flow battery

The VRB is one of the electrochemical energy storage systems gaining increased research interest in the field. The battery known as the Generation 1 VRB employs the same solution of vanadium in sulfuric acid in each half-cell and operates at ambient temperature. Figure 2.2 illustrates a schematic of the VRB system. This system has been extensively investigated in the areas of electrodes, electrolytes and membranes during the period 1985–2005 at the University of New South Wales (UNSW) in Australia led by Prof. Maria Skyllas-Kazacos, the inventor of this technology. With the charge–discharge cycling, the V^{2+}/V^{3+} redox couple in the

negative half-cell and the V^{4+}/V^{5+} redox couple in the positive half-cell are formed. The electrolytes (anolyte and catholyte) containing active vanadium redox couples get circulated. During charging, V^{3+} gets reduced to V^{2+} at the negative side whilst V^{4+} (VO^{2+}) oxidizes to V^{5+} (VO_2^+) at the positive side via the exchange of protons, and subsequent removal of a water molecule. During the charging and discharging processes, the reactions that occur are:

At positive side:

During charging: $VO^{2+} + H_2O \rightarrow VO_2^+ + 2H^+ + e^-$

During discharging: $VO_2^+ + 2H^+ + e^- \rightarrow VO^{2+} + H_2O$

At negative side:

During charging: $V^{3+} + 2e^- \rightarrow V^{2+}$

During discharging: $V^{2+} \rightarrow V^{3+} + 2e^-$

Overall reaction: $V^{2+} + VO_2^+ + 2H^+ \leftrightarrow V^{3+} + VO^{2+} + H_2O$

The standard cell potential (E°) of a VRB is 1.26 V.

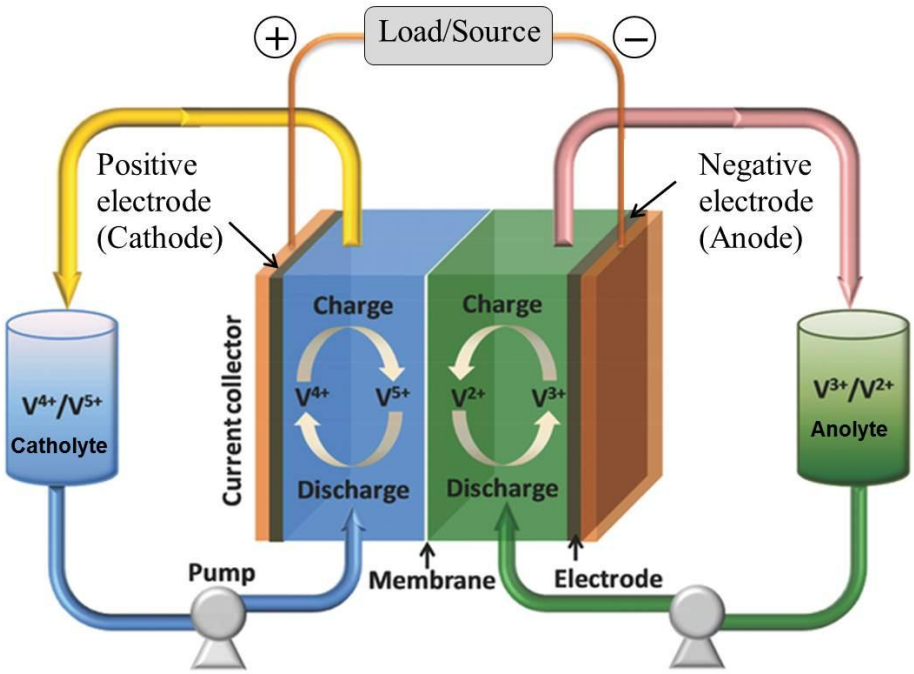

Figure 2.2. Schematic diagram of the vanadium redox flow battery (modified from Ref. [22]).

In VRB, the use of same electrolyte solution in both half-cells eliminates cross-contamination as well as electrolyte maintenance problems. Furthermore, the VRB offers unlimited capacity, design flexibility, good safety, long cycle durability, high charge/discharge efficiency and long life. The conventional design of a VRB utilizes thick porous carbon or graphite electrode in planar contact with flat sheets of graphite bipolar plates. The electrolyte, which flows through the porous electrodes, is stored in the separate electrolyte tanks, outside the battery stack. Due to the aqueous electrolyte, VRB is currently used for stationary applications such as grid energy storage, leveling out supply/demand in power plants, and emergency backup application. VRB is commercially available in the market from past few years. There are several companies working on the VRB, mainly including GILDEMEISTER energy solutions (Germany), Proxhima (Italy), Cellennium Company Limited (Thailand), Sumitomo Electric Industries, Ltd. (Japan), Golden Energy Century Ltd (China), Prudent Energy Inc. (China), Dalian Rongke Power Co., Ltd. (China), redT Energy (United Kingdom), UniEnergy Technologies (United States), H2, Inc. (Korea) and VSUN Energy Ltd **(**Australia). Those companies commercially sell VRB stack systems and their components worldwide [23-33]. The trend of increasing use of renewable energy sources and the widespread installation of solar PV and wind turbines, energy storage for grid applications will increase new servers into the rapidly growing energy storage market.

On the other hand, other redox flow batteries such as iron/chromium [34], polysulfide bromine [35] and iron/titanium [36] employ different redox couple species in each half-cell and encounter cross contamination of electrolytes due to yet no ideal membrane developed. However, low energy density that limits its use to stationary applications has been recognized as the major drawback of VRB. At present, VRB system is still considered to be expensive due to high costs related to its stack components. Thus, research on VRB has been focusing mainly on the overall cost reduction and performance improvement of the system through four aspects: 1) electrode development, 2) electrolyte optimization, 3) membrane development, and 4) optimizing the stack design [37].

2.3.1.1 VRB electrodes

In VRB, the electrodes play very important role in providing active sites for the electrochemical reaction of redox couples in the electrolytes. The energy efficiency and cycle life of any VRB system is primarily derived by the activation and concentration polarizations determined by the electrodes. The electrode provides the active sites for the redox reaction but does not participate in the reaction. It is important that the electrode material for VRB should have good electrical conductivity for fast charge transfer processes, low electrochemical activity for the gassing side reactions, electrochemically stable in the operation potential window, chemically stable in highly acidic environments and good stability during occasional overcharge. Studies have made much effort towards improving the electrochemical properties of the electrodes to make them suitable for practical applications in VRBs [38-41].

The choice of electrode materials, particularly for the positive half-cell, is very limited because of the highly acidic electrolyte used in the VRB and most metals will corrode under typical operating conditions. Various materials have been reported for investigations performed as positive and negative electrodes for the VRB, for e.g., commercial carbon, graphite, Carbon paper, carbon rods, carbon cloths, felts as well as lead, gold, platinum, platinized titanium, and iridium oxide etc [20]. However, most of these products are derived from non-renewable precursors, and in recent years there have been growing concerns on this with the need for exploring alternative environmentally-friendly resources. So far, there is no much investigations carried out on employing biomass-derived carbons as electrodes for VRB applications. Only one publication has reported about the enhanced electrocatalytic activity of coconut shell-derived mesoporous carbons as electrodes for VRB [6]. Hence, more research works are demanded for investigating the potentiality of bio-waste based carbons as electrodes for energy storage applications.

2.4 Supercapacitors

Electrochemical energy-storage devices that are capable of the fast storage and release of energy are commonly known as supercapacitors or ultracapacitors. In this study, the term 'supercapacitor' is used for this device. Unlike batteries, chemical reaction does not take place in supercapacitors when energy is being stored or discharged. The mechanism of energy storage in supercapacitors is simple charge-separation similar to that in conventional capacitors. However, the specific energy of supercapacitors is much higher than conventional capacitors. Also, supercapacitors possess relatively higher energy storage and delivery rates beyond those accessible with batteries. Additionally, supercapacitors have advantage of higher specific power compared with most batteries, but they have lower specific energy than batteries. Thus, supercapacitors deliver an intermediate value of specific power and specific energy compared with classical capacitors and batteries or fuel cells, *i.e*., higher specific power (kW kg^{-1}) than batteries or fuel cells and higher specific energy (Wh kg^{-1}) than conventional capacitors. Figure 2.3 illustrates a general sketch of Ragone plot showing power and energy outputs of different energy storage or conversion devices. The unique combination of power capability and specific energy places supercapacitors to have a functional position between conventional capacitors and batteries. Thus, supercapacitors help complement the deficiencies of batteries and fuel cells. While the supercapacitors at present are promising, there is great scope for further improvements, for example, enhanced performance at higher frequencies and higher energy density in order to contribute in meeting the escalating power demands of energy storage systems. It is possible to realize high specific energy and retain the high specific power through appropriate cell design in combination with batteries so as to make a hybrid system.

Highly reversible charge storage process of supercapacitors make them deliver longer cycle-life and faster charge/discharge rate at power densities exceeding 1 kW kg^{-1} [42]. Table 2.2 provides comparison of characteristics of supercapacitor and battery. Other studies also have reported supercapacitors to possess above discussed features [43], and high charge/discharge efficiency [44]. These features have made supercapacitors very attractive energy storage devices for

a wide range of applications, such as consumer electronics, digital communication devices, mobile phones, digital cameras, hybrid electric vehicles, uninterruptable power supplies and electric tools, pulse laser technique, space and military applications, industrial equipment (cranes, elevators and fork-lifts), industrial power management [45, 46] [47].

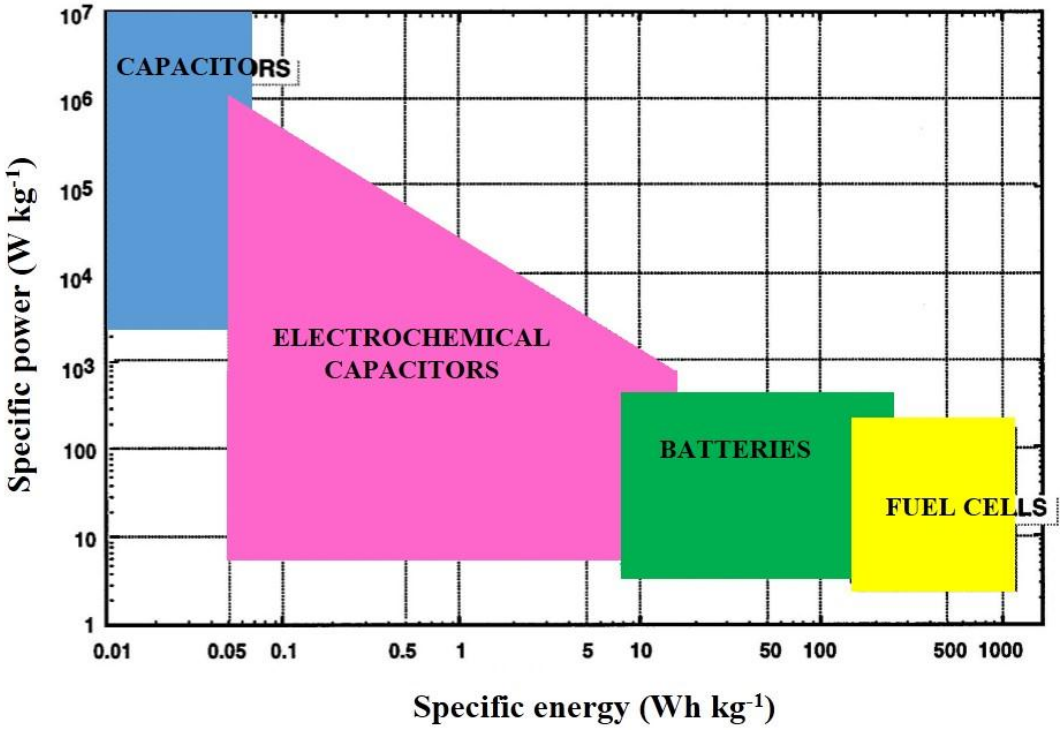

Figure 2.3. A general sketch of Ragone plot showing power and energy outputs of different energy storage and conversion devices (modified from Ref. [48]). The indicated areas show rough guide lines.

Table 2.2. General differences between battery and carbon supercapacitor (modified from Ref. [49]).

Characteristics	Battery	Carbon supercapacitor
Charge time	1 to 5 h	a few seconds to minute
Discharge time	0.3 to 3 h	a few seconds to minute
Charge / discharge efficiency	70 to 85%	85 to 98%
Specific energy (Wh kg^{-1})	10 to 100	1 to 10
Specific power (W kg^{-1})	Below 1000	500 to 10000
Cycle life (number of cycles)	~1000	Above 500000
Voltage (maximum) determinants	Thermodynamics of phase reactions	Electrode material, electrolyte stability window
Charge storage determinants	Active mass and thermodynamics	Electrode material microstructure, electrolyte
Chemicals	Highly reactive and hazardous	Environmentally-friendly

2.5 Classification of supercapacitors

Several previous studies have investigated the science and technology of supercapacitors for different configurations and the role of electrode materials in supercapacitors [48-51]. Based on the mode of charge or energy storage, supercapacitors are presently classified into three types [52-53], namely; 1) electrochemical double layer capacitor (EDLC), 2) redox supercapacitors (pseudocapacitors), and 3) asymmetric/hybrid supercapacitors.

2.5.1 Electrochemical double layer capacitor

The electrochemical double layer capacitors (EDLCs) store energy by means of charge separation in the same way as a conventional capacitor. In EDLC,

accumulation of charges occurs with formation of a layer of ions on both sides of the electrode as electric double layer between the electrode and electrolyte interface *via* non-Faradaic process [52-54]. Electric double layer formation in EDLC is illustrated in Figure 2.4. Thus, EDLCs can store significantly more energy (per unit mass or volume) compared with a conventional capacitor (by several orders of magnitude) primarily due to the following reasons:

- the opposite charges separation occurs across a negligible distance in the electrical double layer that constitutes the interphase between an electrode material and the adjacent electrolyte [50];
- large amount of charges accumulate within porous electrodes that have high surface area. The mechanism of energy storage is much faster since the process only involves movement of ions to and from electrode material surfaces.

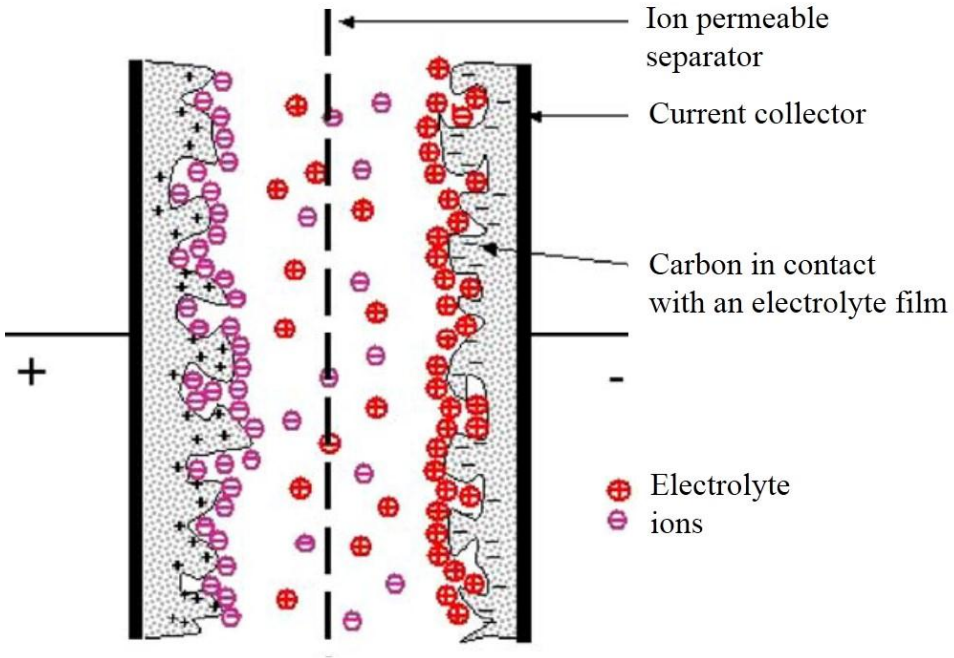

Figure 2.4. Representation of an electric double layer formation in electric double layer capacitor (modified from Ref. [49]).

These characteristics of EDLCs make them achieve a very high degree of reversibility in repetitive charge–discharge cycling resulting in longer cycle-lives even in excess of 500000 cycles [51]. In this regard, the EDLC configuration of the supercapacitor is considered to be the advanced form of electrochemical capacitor [49]. As reported, EDLCs offer high power density and ultra-long cycle-life [52] [53], speedy charging-discharging [58-60], and capability for a wide range of operational temperature [54]. In contrast, in batteries, the energy storage and delivery occur relatively slow due to the additional steps in the process such as heterogeneous charge-transfer and chemical phase changes.

2.5.2 Pseudocapacitors

In pseudocapacitors, a reversible Faradaic-type charge transfer delivers the capacitance, which is often higher. The capacitance obtained is not electrostatic in origin, hence the 'pseudo' prefix is used to differentiate from electrostatic capacitance [52-53]. With the charge storage that occurs based on a redox process, pseudocapacitor is somewhat battery-like in its behaviour. In general, the pseudo-capacitance relies on the potential difference or cell voltage applied, which is indicated by a derivative of $C = d(\Delta q)/d(\Delta V)$, where Δq is a stored charge and ΔV is a potential difference [43]. Additionally, the average capacitance of redox electrodes is calculated from the equation below:

$$C = C_{dl} + C_{\Phi}$$

where, C_{dl} is EDL capacitance and C_{Φ} is pseudo-capacitance

Research works have made tremendous efforts in exploring different types of redox materials for using in pseudocapacitors. The commonly studied pseudo-capacitive materials are transition metal oxides (e.g., RuO_2, MnO_2, NiO), metal hydroxides [e.g., $Ni(OH)_2$, $Co(OH)_2$] and conducting polymers [e.g., Polyaniline (PANI), Polypyrrole (PPy) or derivatives of polythiophene] [50, 55-57]. Studies have reported that the Faradaic reaction can occur through electro-sorption/desorption, intercalation/deintercalation or insertion/deinsertion processes and doping-dedoping processes [58-62]. For instance, the pseudo-capacitance for

MnO_2 can be delivered from electro-sorption as shown in equation 2.1 and intercalation/deintercalation or insertion/deinsertion processes as shown in equation 2.2.

$$(MnO_2)_{surface} + nX^+ + e^- \longleftrightarrow (MnOO^-X_n^+)_{surface} \quad (2.1)$$

$$MnO_2 + nX^+ + e^- \longleftrightarrow MnOO^-X^+_n \ (X = Li^+, K^+, Na^+ \text{ or } H_3O^+) \quad (2.2)$$

2.5.3 Asymmetric/Hybrid supercapacitors

The asymmetric/hybrid SCs are combination of asymmetric electrodes in a same cell similar to pseudo (or battery) type of electrodes, such as metal oxides (e.g., MnO_2, RuO_2, NiO, $LiMn_2O_4$, $MnFe_2O_4$), metal hydroxide (e.g., $Ni(OH)_2$, $Co(OH)_2$) and conducting polymer [e.g., Polyaniline (PANI), Polypyrrole (PPy)] and a capacitor-type of electrode fabricated from carbon materials (e.g., AC, carbon nanotubes, graphene) [63-65]. This device takes the advantage of both pseudo and capacitor electrodes to realize high energy density as well as high power density. The pseudo electrode delivers high energy density through its Faradaic process, and the capacitor electrode retains its high power density. Thus, hybrid supercapacitors aim to enhance the energy density closer to batteries and retain high power density.

2.6 Electrode materials for supercapacitors

Several inherited favourable properties of carbonaceous materials make them well suited for utilizing as electrode material for energy storage applications. The attraction of carbon as electrode material comprises a unique combination of several chemical and physical properties, such as high surface area, high conductivity, good corrosion resistance, high temperature stability, tailored pore structure, environmental-friendliness, low cost, processability and compatibility in composite materials [49]. Research works have made great efforts on preparation or development of various carbon materials possessing desired properties (e.g., high surface area, good pore width, low matrix resistivity) for using as electrode material [66-70]. Carbon materials in various forms have been extensively investigated and widely utilized as electrode or incorporated into the electrodes for energy storage applications [50] [71] [56]. The use of carbons in energy storage devices include:

electrode substrates, supports for active materials, electron transfer catalysts, electro-conductive additives, intercalation hosts, substrates for current leads, and as agents for the porosity, high surface-area and high capacitance [72]. Several studies have demonstrated that the performance of carbon-based energy storage devices are closely linked to the physical and chemical properties of the fabricated electrodes [43, 49, 51, 72]. Therefore, it is very important to understand carbon materials and their properties for matching carbon characteristics with different energy storage devices.

Various carbon materials and their common precursors, and the major processing conditions are shown in Table 2.3. However, the majority of currently available commercial carbon materials are derived from non-renewable precursors (e.g., coals, petroleum pitch, petroleum coke, coal pitch) by high-temperature treatment (>2500 °C) [49]. Additionally, the cost of graphite used as electrode material is higher compared with activated carbon (Table 2.4) [73-78]. The supply of graphite electrodes has decreased considerably in past couple of years. With the decreasing stock but increasing demand, graphite electrode prices have risen sharply recently [79]. The global graphite electrodes market which was valued at $ 5.04 billion in 2016 is projected to reach $ 27.5 billion by next 5 years (2022) [80]. In growing concerns to continuous use of these limited resources and environmental degradation, it has become urgent to explore alternative sustainable clean precursor materials for producing carbon materials as electrodes. This will contribute in the supply of increasing electrodes demand to some extent though not possible to replace the whole electrodes need, and also help in cost reduction in the related sector with alternative electrode material.

Table 2.3. Various carbon materials and their common precursors, and the key production conditions (modified from Ref. [71]).

	Carbon material	Common precursors	Controlling factors (production)	Structural / textural features
Gas phase	Carbon blacks	Hydrocarbon gas or liquid	High precursor concentration	Nano-size particles
	Pyrolytic carbon	Hydrocarbon gas	Deposition on a substrate	Preferred orientation
	Vapour-grown carbon fibers (carbon filaments/nanofibers)	Hydrocarbon gas	Presence of a catalyst	Catalyst particle size / shape
	Fullerenes	Graphite rod	Condensation of carbon vapour	Nano-size molecules
	Carbon nanotubes	Hydrocarbon vapour	Condensation of carbon vapour (with or without catalyst)	Armchair, zig-zag, chiral; single-wall or multi-wall
	Diamond-like carbons	Organic vapour	Condensation of organic vapour	sp^3 and sp^2 bonding
Liquid phase	Cokes (e.g., needle coke)	Coals, petroleum pitch	Shear stress	Mesophase formation and growth
	Graphite	Petroleum coke	High temperature	Mesophase formation and growth
	Carbon fibers (e.g., pitch derived)	Coal pitch, petroleum pitch	Spinning	Mesophase formation and growth
Solid phase	**Activated carbon**	**Biomass**, coals, petroleum, coke, selected polymers	**Carbonization / activation**	**Nano-size pores**
	Molecular-sieve carbons	Selected biomass, coals, polymers	Selective pore development	Nano-size pores and constrictions
	Carbon fibers (e.g., polymer derived)	Selected polymers (e.g., polyacrylonitrile)	Slow carbonization	Nano-size, random crystallites, nonporous
	Glass-like carbons	Thermosetting polymers (e.g., polyfurfuryl alcohol)	Slow carbonization	Random crystallites, impervious
	Highly oriented graphite	Pyrolytic carbon, poly-imide film	High molecular orientation	Highly oriented crystallites

Table 2.4. Comparative costs of graphite/graphite electrode and biomass-based activated carbon.

Graphite	Cost	Activated carbon	Cost
Battery Grade Flake (99.9%)	USD 5000–20000 per tonne [73]	Activated carbon (powder, wood base)	USD 1100–2400 per tonne [76, 77]
Graphite (Grain Size: 2-40 μm)	USD 2600–5900 per tonne [74]	Activated carbon (powder, coconut shell base)	USD 1300–1800 per tonne [78]
Graphite Electrodes	Upto USD 10000 per tonne [75]		

2.7 Synthesis of biomass derived activated carbons

The nature of the carbon precursors, activation methods or processing conditions (e.g., activation agent and its dosage, activation temperature and duration) are key factors affecting ultimate properties (structural and textural features, and surface functional groups) of the resultant carbons [71, 81, 82]. Researchers have explored various synthesis routes for preparing ACs with tailored pore structures and textural properties. Common methods employed for AC preparation are physical activation and chemical activation [1, 2]. Physical activation in an inert atmosphere comprises two steps: carbonization at low temperature to remove non-carbon elements, followed by high temperature treatment of the carbonized product using CO_2 [83] or steam [84] as activating reagent. In chemical activation, biomass is first treated with selected chemical reagent, and then carbonized at high temperature (400–900 °C) in an inert atmosphere [85, 86] [3] [4, 5] [87]. Chemical activation has been widely used mainly due to lower reaction temperature and larger BET surface area compared with physical activation, for example, KOH [88, 89], K_2CO_3 [90, 91], $KHCO_3$ [92], $ZnCl_2$ [93], H_3PO_4 [94] and NaOH [95]. Among these chemical reagents, studies have widely used KOH for the synthesis of ACs [88, 96, 97] due to its significant role in the porosity development. The absence of chemical activation implies that porosity of the resulting carbon is underdeveloped [98] and its use in energy storage applications show poor performance compared to carbons with

enhanced porosity [[99] [100] [101]]. Thus, textural properties of carbons should be improved for facilitating high mass transfer fluxes that result in enhanced electrochemical performance.

2.8 Biomass-derived carbon as electrode material

AC possesses attractive features such as low cost, high surface area, porous nature, good electrochemical stability and electrical conductive [11, 102]. Large surface area and higher electrical conductivity of AC facilitate the effective electrostatic adsorption of electrolyte ions for energy storage in supercapacitors. Thus, ACs have been used as electrode material for energy storage applications, and towards the effective treatment of aqueous solutions. In commercial supercapacitors, conventional non-renewable resources, such as petroleum coke, coal and tar pitches are used as carbon source. However, the limited reserves of these resources have raised the concerns for their continuous use for the large scale production of ACs and to meet the demand in future. In this perspective, biomass is a low cost, abundant, renewable and environmental-friendly resource, which can be alternative sustainable precursor for AC preparation.

In recent years, biomass-derived ACs as electrodes for energy storage applications are gaining increased attention [86, 90, 103] [104]. A wide variety of biomass-derived ACs have been investigated for their electrochemical performances. Table 2.5 presents summary of some previous studies related to biomass-derived ACs for supercapacitors. In a study, AC produced from coconut shell with steam activation delivered specific capacitance of 228 F g^{-1} at 5 mV s^{-1} in 6 M KOH [105]. AC synthesized from celtuce leaves using KOH as activating agent has surface area of 3404 m^2 g^{-1} and specific capacitance of 273 F g^{-1} at 0.5 A g^{-1} tested in 2 M KOH electrolyte [106]. Other study using potato starch as a precursor with KOH activation reported high specific capacitance of 335 F g^{-1} in 6 M KOH electrolyte for the synthesized AC with surface area of 2340 m^2 g^{-1} [38]. Similar results as that for starch are reported for NaOH treated apricot shell derived AC, which delivered surface area of 2335 m^2 g^{-1} and specific capacitance of 339 F g^{-1} in 6 M KOH electrolyte [95]. Coffee beans derived AC produced using

$ZnCl_2$ was reported to deliver even a higher specific capacitance of 368 F g^{-1} in 1 M H_2SO_4 aqueous solution [107]. Interestingly, neem leaves derived AC despite lower surface area (1230 m^2 g^{-1}) than other aforementioned precursors was reported to deliver very high specific capacitance (400 F g^{-1}) in 1 M H_2SO_4 as electrolyte [9]. Studies have also employed organic solutions as electrolytes in electrochemical measurements of ACs as electrodes for SCs. A study using wheat straw derived AC obtained by KOH activation reported surface area of 2316 m^2 g^{-1} and specific capacitance of 251 F g^{-1} in 1.2 M Methyltriethylammonium Tetrafluoroborate ($MeEt_3NBF_4$)/AN) organic electrolyte [12].

Table 2.5. Biomass-derived ACs and their electrochemical performances as electrode material.

Biomass	**Activating agent**	**Surface area (m^2 g^{-1})**	**Electrolyte**	**Specific capacitance (F g^{-1})**	**Ref.**
Cassava peel	KOH + CO_2	1352	H_2SO_4	153	[13]
Rice husk	NaOH	1890	3 M KCl	210	[10]
Rice husk	KOH	1390	3 M KCl	180	[10]
Rice straw	KOH	~1007	H_2SO_4	156	[108]
Rice husk	NaOH	1886	KCl	210	[10]
Rice husk	KOH	1392		180	[10]
Wheat straw	KOH	2316	$MeEt_3NBF_4/CH_3CN$	251	[12]
Wheat straw	KOH	2316	1.2 M $MeEt_3NBF_4$/AN	251	[12]
Coffee beans	$ZnCl_2$	1020	1 M H_2SO_4	368	[107]
			1 M $TEABF_4$/AN	134	[109]
Coffee shells	$ZnCl_2$	842	KOH	150	[110]
Waste coffee ground	$ZnCl_2$	940–1021	$MeEt_3NBF_4$/AN	100	[107, 109]
			H_2SO_4	368	
Banana fiber	$ZnCl_2$	1100	1 M $NaSO_4$	74	[111]
Banana fiber	$ZnCl_2$	686	Na_2SO_4	74	[111]
Banana fiber	KOH	1097		66	[111]

Biomass	**Activating agent**	**Surface area (m^2 g^{-1})**	**Electrolyte**	**Specific capacitance (F g^{-1})**	**Ref.**
Waste paper	KOH	416	6 M KOH	180	[112]
Corn grain	KOH	3200	6 M KOH	257	[113]
Coconut shell	KOH	1660	6 M KOH	79	[114]
Coconut shell	Steam	1532	6 M KOH	228	[105]
Coconut shell	KOH	3000	KOH	368	[115]
Apricot shell	NaOH	2335	6 M KOH	339	[95]
Sunflower seed shell	KOH	2510	30 wt.% KOH	311	[116]
Bamboo	KOH	1250	30 wt.% H_2SO_4	65	[117]
Bamboo			1 M Et_4NBF_4/PC	35	[117]
Bamboo	KOH	1413	Et_4NBF_4	15–65	[117]
Bamboo	Steam	445–1025	Non-aqueous	5–60	[118]
Firewood	Steam	1130	1 M HNO_3	142	[119]
Eucalyptus wood	KOH	2970	1 M $TEABF_4$/AN	236	[105]
Potato starch	KOH	2270	1 M $TEABF_4$/AN	180	[120]
Potato starch	KOH	2340	6 M KOH	335	[121]
Potato starch	KOH	2342	KOH	335	[121]
Neem leaves	-	1230	1 M H_2SO_4	400	[9]

Biomass	**Activating agent**	**Surface area (m^2 g^{-1})**	**Electrolyte**	**Specific capacitance (F g^{-1})**	**Ref.**
Neem leaves			1 M $LiPF_6$ in EC/DEC	88	[9]
Celtuce leaves	KOH	3404	2 M KOH	273	[106]
Corn grains	KOH	2936–3420	KOH	257	[113]
Sunflower Seed Shell	KOH	1371–2821	KOH	311	[116]
Walnut Shell	Physical/chemical	1197	KOH	292	[122]
Pistachio shells	Steam	1009	HNO_3 & H_2SO_4	60–125	[123]
Pistachio shells	KOH + CO_2	1013–2145	H_2SO_4 & $NaNO_3$	25–47	[124]
Sorghum pith	NaOH	17–35	H_2SO_4	220–320	[11]
Sugar cane bagasse	$ZnCl_2$	1788	H_2SO_4	300	[125]
Sugar cane bagasse	$ZnCl_2$ (microwaves)	1348–1465	Ionic liquid	138	[126]
Sugar cane Bagasse	NaOH	1790	1 M H_2SO_4	300	[125]
Cherry stone waste	KOH	1300	H_2SO_4	230	[127]
			1 M $(C_2H_5)_4NBF_4$/AN	120	[127]
Firewood	Steam	1016	H_2SO_4	96	[119]
Firewood	KOH	2821	$NaNO_3$	165	[128]
	KOH + CO_2		H_2SO_4	197	[123]

2.9 Food wastes – a valuable renewable resource

Food waste is defined as the mass of food lost, degraded or discarded from various sources that have not been recycled or used for other purposes [129] [130]. Based on the source, food wastes can be broadly categorized into plant or animal origin. Furthermore, food waste from plant origin may be kept under cereals, root and tubers, oil crops and pulses, fruits and vegetables. Notably, food wastes show high variability in quality based on locations, seasons and economy level. In economically developing countries, food wastes are primary generated during agricultural production and secondarily during postharvest handling or storage. Whereas food losses in the industrialized countries are shared between agricultural and consumption stages [130].

Food waste occurs at all stages of the food supply chain – production, processing, retailing and consumption. Large quantities of food wastes are generated worldwide with the volumes increasing over the years, and they are generally disposed as 'garbage'. It has been reported that, globally nearly one-third to one-half of the total foods produced including fruits get lost or wasted [130, 131]. It is necessary to manage the food wastes, which contaminate recyclables and compromises recycling efforts. In addition, food wastes, if not managed properly, may cause odour nuisance and vermin proliferation. It is recommended to adapt the food waste hierarchy as a framework for the minimization of food waste generation.

The amount of waste generation is expected to increase with the economic growth and increase in population, particularly in Asian countries. According to Waste and Recycling Statistics for 2016, the amount of total food waste generated in Singapore was 791000 tonnes**,** up by 5500 tonnes from 785500 tonnes in 2015. Food waste is about 10% of the total waste generated. However, the amount of food waste generation increased by about 40% over the past 10 years. Most of food waste is disposed of at the waste-to-energy (WTE) plants for incineration [132]. In some countries, most of food waste ends up in landfill [133].

Proper waste management is a prerequisite for sustainable resource management on the notion that **'waste is not waste but a misplaced resource'**. Research works have reported deriving of value added chemicals (such as

flavonoids, fatty acids, pectin, animal feed) from food waste. Based on the review, it can be said that food waste is a very attractive renewable resource with high potential for resources recovery [14, 134, 135].

2.9.1 Food waste management and treatment practices

Waste management practices raise several environmental concerns, and proper management of huge amount of food waste is one of the challenges faced by both economically developing and developed countries. Food by-products are usually dumped as garbage in economically developing countries which may cause environmental nuisance, whereas it is utilized for heat or energy in industrialized countries. Currently, the disposed carbon based materials (e.g., food wastes) are managed in various ways, mainly landfill, incineration, anaerobic digestion for methane production, composting and animal feeding.

Landfill is a conventional disposal method for municipal solid waste, unrecyclable residues and incineration ashes. However, the process is costly in terms of transportation costs to centralized landfill sites. Furthermore, the process poses serious environmental concerns with releases of greenhouse gases (e.g., CO_2, and CH_4), and leachates [136]. In addition, the need of large space makes the landfill not a preferred option for land-scare and densely populated areas, such as Singapore.

Incineration is thermochemical process to treat combustible wastes, which reduces the waste volume by 90% and generates energy. However, moisture content in food wastes is high and makes the process energy-intensive. Together with these, loss of chemical values, generation of harmful emissions and ash (containing heavy metals) disposal issues are challenges associated with incineration [15, 137, 138]. Flue gas scrubbing is also costly [139].

Animal feed is usually the most cost effective approach for food waste valorization. However, there are sometimes limitations associated with regulatory issues and the co-product natures in the process.

Composting is popular solid waste management practice for the production of soil fertilizer. Furthermore, it diverts wastes from landfill and reduces farmers' dependency on chemical fertilizers. High moisture content in food wastes that reduce oxygen and heat transfer may affect the biological activity in composting process [140]. Furthermore, composting has issues for high emissions of ammonia (NH_3) and it is also difficult to estimate if compost materials rich in organic matter possess ability to replace mineral fertilizers [141].

Anaerobic digestion is a suitable process for food waste treatment with biogas production. The main product biogas is used to generate energy, and the residues (digestate) utilized for compost production. However, large foot-print and digestate material disposal are issues of this process.

Based on a life cycle assessment perspective of the environmental performance of conventional waste management practices, Sonesson *et al.* reported that anaerobic digestion results in the lowest environmental impact, whereas composting is environmentally favorable compared to incineration [142]. The need of a sustainable food waste management approach has been suggested so as to make it environmentally-friendly, ensure public health safety and promote recycling of resources [16, 130] [143].

2.9.2 Fruit peels waste – a renewable carbon source

Fruit peels are sustainable eco-friendly valuable resources that are discarded in large quantities from juice processing industries and fruit juice outlets. Currently, these are generally disposed as ‘garbage’ that ends up resulting environmental nuisance. The worldwide annual production of fruits is more than 675 million metric tonnes, of which the greatest harvest occurs in Asia [144]. According to the Food and Agriculture Organization of the United Nations (FAO), citrus fruits production in 2016 was 124 million tonnes with ~67.0 million tonnes of oranges. Total citrus fruits utilization for processing was 23.5 million tonnes with the share of 18.5 million tonnes of oranges [145]. This suggests availability of a huge quantity of fruit peels bio-waste, which is renewable. However, if not properly managed, the peels from such large quantities pose a big disposal problem in regions with large

fruits production [146]. Fruit peels mainly consist cellulose, hemi-cellulose, lignin, pectin, chlorophyll pigments and other hydro-carbons [147, 148]. Due to the different OH groups in cellulose, fruit peels contain carboxyl and hydroxyl groups which play important roles in their usage such as adsorbents [148] or other applications. Of the citrus peels, a few previous studies have used orange (*Citrus sinensis*) peel waste as a precursor for the synthesis of carbon products, and the resultant products were employed as adsorbents for dyes and organic contaminants treatments [146, 149, 150]. Similarly, hydrochars produced from orange peel waste are investigated as adsorbent for removing metallic ions from aqueous solutions [99, 151-154]. A recent study reported the synthesis of fluorescent carbon dots from orange peel waste as a photocatalyst for degradation of naphthol blue-black azo dye [155]. Studies on application of orange peel waste derived ACs for energy storage applications are scarce. In a previous study, orange peel derived AC was employed as cathode for lithium ion capacitor (LIC) and achieved the capacitance value of 51.7 F g^{-1} in an organic electrolyte solution at scanning rate of 1 mV s^{-1} [156]. A study prepared orange peel based carbon nanosheets, which was used as a substrate to obtain MnO_2 nanorods composite for supacapacitors [147]. Lychee (*Litchi chinensis*) peel waste, another low cost agro bio-waste, is recently reported to possess favourable properties for its application as an effective adsorbent for the treatment of industrial effluents containing dyes [157]. One other research used lychee peel waste for investigating the corrosion inhibitory effect of its extract as an adsorbent on metal surface [158]. However, the conversion of lychee peel waste to high-value products such as AC, and its usage for energy storage applications has not been reported yet. One other study on three fruit peels (orange peel, lemon peel and banana peel) was limited to characterization studies so as to investigate the nature of the functional groups and their role in the removal of heavy metal ions from aqueous solution [159]. Table 2.6 provides summary from previous studies on fruit peels waste, suggesting limited investigations conducted on employing these low cost, renewable and eco-friendly resources for energy storage applications. The utilization of these renewable agro-wastes contributes not only waste management through reduction of volume of wastes but also generates value-added products for promising applications. At present, reports on the utilization of food waste for

carbon materials production on an industrial scale are not found. However, there is International Pectin Producers' Association (IPPA) that mentions collection of fruit residues (citrus peel and apple pomace) from juice producers for pectin production at commercial scale [160].

With these premises, this study aims to explore the potentiality of utilizing this underutilized waste resource as promising precursor for synthesis of value-added carbons, and further evaluate the feasibility of using the resultant products as electrode materials for energy storage applications. The potentiality of employing fruit peels waste as valuable resource as precursors is illustrated in Figure 2.5. This will provide multiple benefits - turn disposable waste material to value-added porous carbons, reduce the sole dependency on non-renewable fossil fuels for electrode material, and also contribute in waste management.

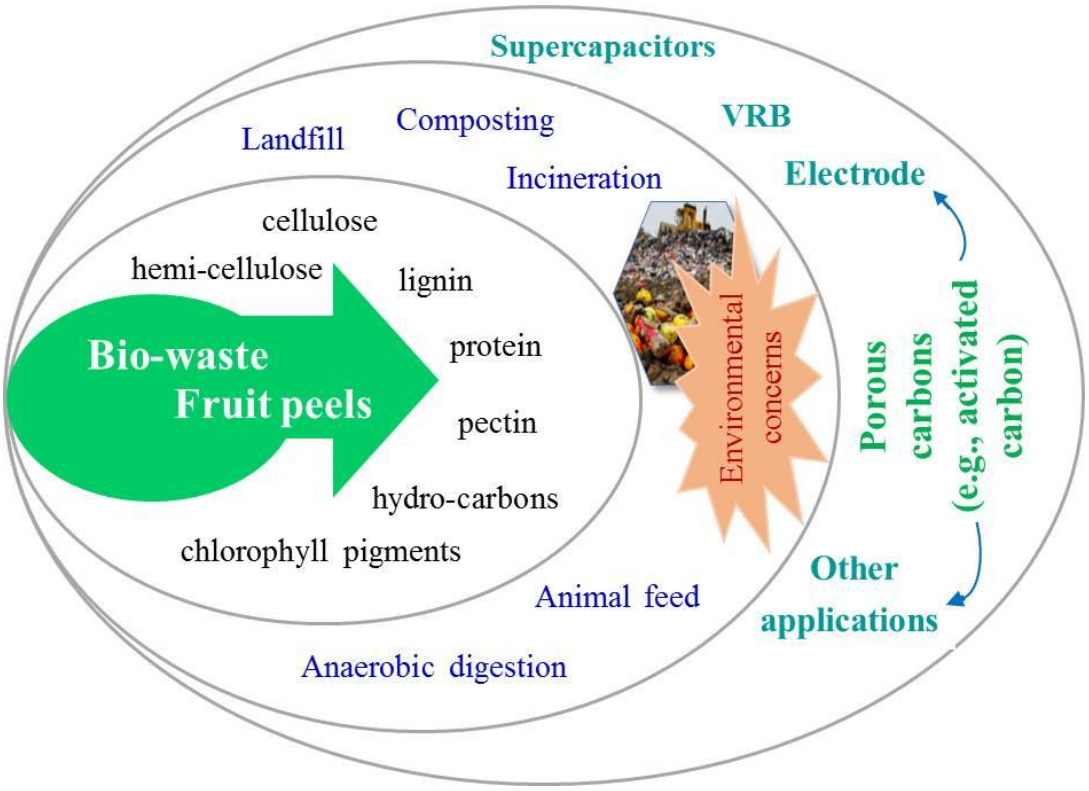

Figure 2.5. Bio-waste, fruit peels: a green resource for conversion to value-added porous carbon.

Table 2.6. Fruit peels waste based carbon products and their applications.

Precursor	Process	Activating agent	Activation	Product	BET Surface area (m^2 g^{-1})	Application	Ref.
Orange peel	hydrothermal, pyrolysis	-	300 °C and 600 °C, 6 h	biochars	-	adsorbent (cu II)	[151]
Orange peel	Pyrolysis	-	150, 200, 250, 300, 350, 400, 500, 600 and 700 °C	biochars	22.8-201	adsorbents (organic pollutants)	[161]
Orange peel	hydrothermal	citric acid	200 °C, 16 h	hydrochar	-	-	[99]
Orange peel	Chemical	H_3PO_4	hydrochar to 600 °C, 1 h	activated hydrochars	301 to 618	adsorbents	[149]
Orange peel	Chemical	H_3PO_4	475°C, 0.5 h	AC	1090	adsorbents (dyes)	[146]
Orange peel	chemical, microwave	K_2CO_3	700° C, microwave	AC	1105	adsorbents (MB)	[162]
Orange peel	hydrothermal	-	180 °C, 12 h	carbon dots	-	photocatalyst	[155]
Orange peel	Chemical	$ZnCl_2$	500 °C, 1 h	AC	1200	supercapacitors	[156]
Orange peel	Chemical	-	800 °C, 2.5 h	AC	500	supercapacitors	[147]

Precursor	Process	Activating agent	Activation	Product	BET Surface area ($m^2 g^{-1}$)	Application	Ref.
Lychee peel	-	-	-	-	-	adsorbents (dyes)	[157]
Lychee peel	-	-	-	-	-	adsorbents	[158]
Orange peel, Lemon peel, Banana peel	-	-	-	-	-	Adsorbents (heavy metal ions)	[148]

2.10 Research gaps and current issues

Literature review carried out on carbon materials, AC synthesis methods, electrode materials for energy storage applications and existing energy storage technologies revealed research gaps and current issues. The massive consumption of conventional fossil fuels as energy resources has generated a worldwide fear for depletion of this non-renewable resource. There has also been increasing concerns on global warming and its adverse impacts. Furthermore, there is ever-growing energy demand due to the rapid urbanization, industrialization and developmental activities. Therefore, the depletion of limited conventional fossil fuels and growing concerns on environmental pollution has led to explore alternative sustainable resources as potential carbon precursors. The enhancement of electrochemical performance of existing energy storage technologies and development of efficient energy storage devices / technologies are other side requirements in order to meet the energy demand.

Previous studies have extensively explored various biomass as precursors for preparation of ACs as shown in Table 2.5. The studies mainly employed plant materials and their by-products as raw materials for synthesizing AC as electrodes for energy storage applications. However, studies on the use of fruit peels waste (bio-waste) as precursors for AC preparation and their application studies are scarce (Table 2.6). Therefore, comprehensive study is higher demanded to evaluate the potential of employing this under-utilized sustainable resource for preparation of value-added useable products, such as porous carbon. Further investigations are also needed to evaluate the electrochemical performance of the as-synthesized bio-waste AC as electrodes for energy storage applications, and development of high performance energy storage devices.

CHAPTER 3

General Materials and Methods

In this chapter, the generally used materials and methods in this study are described. Materials and methods for specific studies are specified in respective chapters.

3.1 Materials

The term '*bio-waste*', in this study, is referred to *fruit peels.* A total of 11 fruits namely, apple, banana, grapefruit, orange (Mandarin), Thai longan, lychee, pineapple, water melon, honey dew and lemon were considered based on their availability in the local supermarket in Singapore. Fresh apple, banana, grapefruit, orange (Mandarin), Thai longan and lychee were purchased from Giant Supermarket, and their peels collected. Whilst peels of pineapple, water melon, papaya, honey dew and lemon were collected from a juice/fruit stall of canteen in Nanyang Technology University (NTU), Singapore. In order to avoid the variation in the feedstock, fruits purchase and peels collection were carried out only once in adequate quantities to get enough samples.

All the chemicals were of analytical grade and were used as received without further purification unless specified. Potassium hydroxide (KOH, Cat No. P162 0492, Sinopharm Chemical Reagent Co. Ltd), potassium bromide (KBr, FT-IR Grade, Sigma−Aldrich), hydrochloric acid (HCl, 37%, Merck KGaA, Germany), nitric acid (HNO_3, 65%, Merck KGaA, Germany), sulfuric acid (H_2SO_4, 98%, Merck KGaA, Germany) and ethanol (Merck KGaA, Germany) were purchased. Other materials include bipolar plate of 0.6 mm thickness (TF6, SGL Carbon, Germany), PAN based carbon felt of 4.6 mm thickness (SIGRACELL GFD 4.6 EA, SGL Carbon, Meitingen, Germany), Fluorinated anion-exchange membrane of 50 μm thickness (fumasep® FAP-450, FuMA-Tech GmbH, Bietigheim, Germany), Vanadium electrolyte (1.6 M $V^{3.5+}$ in 4.5 M total sulphate (GFE, Nuremberg, Germany) were used. Whatman paper (Cat No. 1825-045, Whatman

International Ltd Maidstone England). Carbon black, polyvinylidene fluoride (PVDF), N-Methyl-2-pyrrolidone (NMP) solution, toray paper of 0.04 mm thickness, and CR2016 coin-cell, Lithium hexafluorophosphate ($LiPF_6$), Lithium titanium oxide (LTO), ethylene carbonate (EC), di-methyl carbonate (DMC), TAB-2, graphite (Sigma-Aldrich), graphene oxide (GO), aniline monomer, ammonium persulfate (APS) were also used in the study. All the experiments were conducted using the deionized water (18.2 MΩ cm) and Milli-Q water.

3.2 Bio-waste sample powders

The collected peels and purchased fruits were thoroughly washed with tap water followed by Milli-Q water to remove adhering dirt, if any. The peels of all fruits were cut into small pieces separately, and then kept in an oven at 60 °C for 12 h. Dried peels were separately ground using ball mill and sieved (300 µm aperture) to obtain fine powders. Each powder was collected in clean dry bottles and stored in a desiccator for further studies.

3.3 Ultimate analysis

Carbon content in the samples is major constituent for activated carbon preparation. Thus, ultimate analysis of the sample powders was carried out to determine the elemental composition (carbon, hydrogen, nitrogen, sulfur contents) in the precursor materials prior to synthesis of porous AC. The synthesized ACs were also subjected to ultimate. This analysis was carried out using an elemental analyzer (vario EL cube CHNOS, Germany). The oxygen content in the samples was obtained as the difference as shown below.

$$O\% = [100 – (C + N + H + S)]\%$$

3.4 Proximate analysis

Proximate analysis of the powder samples was carried out for moisture content, volatile matter (VM), fixed carbon (FC) and ash content. The FC content was obtained from calculation based on the VM and ash experimental data. Each sample was tested three times using approximately 1 g measured in crucible.

Moisture is a ubiquitous and variable component of any biomass samples. Moisture content in the precursor samples was determined following the ASTM E 1756 method. The moisture content of a sample is considered to be the amount of mass lost during the drying of the sample at 105°C to constant mass. The procedure followed is described below:

a) For each sample, a clean beaker with lid was uniquely marked with a permanent marker and then placed in the drying oven at 105°C for one hour. The containers were cooled to room temperature in the desiccator.
b) Each beaker was weighed on the analytical balance to the nearest 0.1 mg. The weight was recorded as the tare mass, m_t.
c) In the dried beaker, 1.0 g of sample was added, and the mass of the sample plus beaker was recorded as the initial mass, m_i.
d) The beaker with the sample was placed in the drying oven at 105 ± 3°C for at 12 h (overnight). Then the sample was allowed to cool to room temperature in a desiccator. Each sample was weighed to the nearest 0.1 mg and this mass was recorded. After weighing, the samples were returned to the drying oven at 105°C for 1 h, cooled again in the desiccator, and weighed recorded again. This step was repeated until the mass of the samples varied by less than 0.3 mg from the previous weighing. This mass was recorded as the final mass, m_f.

The percent moisture content in the sample was calculated as follows:

Moisture in sample, %

$$= (m_i - m_f)/(m_i - m_t) \times 100$$

where:

m_t = tare weight of dried beaker, g,

m_i = initial sample powder weight and beaker together, g, and

m_t = dried sample powder weight and beaker together, g.

The ash content in biomass is an approximate measure of the mineral content and other inorganic residue left after ignition at 575 ± 25°C. Ash content in

the precursor samples was determined following the ASTM E 1755 method. The procedure followed is described below:

a) For each milled sample, a clean crucible (50 mL) was marked with a unique identification using a porcelain marker and then placed in the muffle furnace. Constant mass was obtained by igniting it at 575 ± 25°C followed by placing in drying oven at 105°C for one hour. The crucible was cooled to room temperature in the desiccator, and stored until used.
b) Each crucible was weighed on the analytical balance to the nearest 0.1 mg. The weight was recorded as the tare mass, m_t.
c) In the crucible, approximately 1.0 g of the pre-dried sample at 105°C according to Test Method E 1756 was weighed. The mass of the sample plus crucible was recorded as the initial mass, m_{od}.
d) The crucible with sample was placed in the muffle furnace and ignited at 550 ± 25°C for 3 h. The temperature programme in the furnace was set as to initially heat the sample to 250°C at a rate of 5 °C min^{-1} and hold for 30 min, then the temperature increase to 550 °C.
e) The test crucible with its contents was removed to a desiccator, cooled to room temperature, weighed to the nearest 0.1 mg, and recorded the mass.
f) The samples were returned to the furnace and repeated the heating for one hour periods until the mass measured constant to within 0.3 mg after cooling. The final mass of the residue (ash) was recorded ash, $m_{ash,}$ which is the container plus ash mass.

The percent ash content in the sample was calculated as follows:

Ash in sample, %

$$= [(m_{ash} - m_t)/(m_{od} - m_t)] \times 100$$

VM in biomass refers to the components released when the sample is heated at a high temperature without including moisture. It has been reported that biomass usually contain very high VM which may range from 75-90% depending on the

sample [163]. In this study, VM content of pre-dried fruit peel powders (as per ASTM E 1756) was determined following the ASTM D7582 method. The procedure followed is described below:

The procedure followed is described below:

a) Firstly, a clean test crucible was heated to 950 ^{o}C in an inert atmosphere with continuous flow of nitrogen gas (60 ml min^{-1}) using STA 449 Jupiter® (Netszch). The temperature program was set at ramp rate of 20 K min^{-1} and maintained for 7 minutes. The crucible was cooled to room temperature.
b) The cooled crucible was weighed on the analytical balance to the nearest 0.1 mg, and the weight was recorded as the tare mass, m_t.
c) In the crucible, approximately 10.0 mg of the pre-dried sample at 105°C according to Test Method E 1756 was weighed. The mass of the sample plus crucible was recorded as the initial mass, m_i.
d) The crucible with sample was placed in the furnace pan and heated as stated in (a). The test crucible with its contents was cooled to room temperature.
e) The residue mass was weighed as the final mass, m_f. The mass loss is calculated for the VM. The mass loss is also available from the instrument analysis data.

The percent VM content in the sample was calculated as follows:

VM in sample, %

$$= [(m_i - m_f)/(m_i - m_t)] \times 100$$

where:

m_t = tare weight of crucible, g,

m_i = initial sample powder weight and crucible together, g, and

m_f = residue weight and crucible together, g.

FC is the remaining mass after the release of VM and excluding moisture and ash content. In this study, FC was determined by difference from the dried sample mass by subtracting ash and VM contents for non-inorganic char residues as follows:

FC % = 100 – (Ash % + VM %)

3.5 Thermogravimetric analysis

In order to understand the carbonization behavior of the samples, thermogravimetric analysis (TGA) was carried out by Simultaneous TG-DTA/DSC Apparatus (Model: STA449 F3 Jupiter®, Netzsch) in an atmospheric pressure with nitrogen flow fixed at 60 mL min^{-1}. The weight loss (TG) of samples was recorded under dynamic-isothermal conditions to 950 °C at a heating rate of 20 K min^{-1}. These experimental runs were conducted by placing about 10 mg of samples on the same TG pan. Simultaneous thermal analysis (STA) was carried out where TGA measured mass loss data of the samples thermal degradation while simultaneously DSC measured heat transfer signals based on temperature differences between crucible with samples and reference crucible in heating chamber. Heat of pyrolysis, $\Delta H_{pyrolysis}$ was measured at main degradation region of the samples studied. Linear baseline was established for DSC signals recorded and the area under the curve was calculated as heat of pyrolysis.

About 10.0 mg of sample placed in alumina, Al_2O_3 crucible and heated using required temperature programme with constant heating rate from initial ambient temperature at 30^oC to final temperature at 950^oC. Heating rate of 20 K min^{-1} was used with reference to thermal analysis data collection procedure suggested by ICTAC Kinetics Committee [164]. Lid for crucible was not used in order to reduce secondary char formation reactions. Nitrogen with flow rate of 60 mL min^{-1} was supplied continuously to create inert atmosphere inside the heating chamber and also to remove volatile compounds that are released from heating chamber while maintaining atmospheric pressure of the system.

Systematic errors of STA system should be minimized by calibration using reference metals as well as blank run with empty crucible and initialization stage at 100^oC with nitrogen flow for 30 minutes prior to running the experiment. Temperature and DSC signals were calibrated using at least five different metals as reference compounds with distinctive melting temperature and heat of melting. In this process, selection of metals was carried out based on individual melting

temperature relative to the temperature range of experiments. Blank run with empty crucible prior to sample analysis allow background correction for buoyancy effects on mass measured. Initialization stage helps remove any residual moisture in the pre-dried samples and purge out any residual air inside heating chamber to maintain inert atmosphere.

3.6 Synthesis of activated carbons from bio-waste samples

Activated carbons (ACs) were synthesized from the selected five bio-waste samples. In the process, KOH was used as an activating agent. Firstly, the weighed amount of sample powder was heated in a reactor in a tubular furnace (Carbolite) to 400 °C (5 °C min^{-1}) under argon atmosphere (50 mL min^{-1}) with dwelling for 1 h, and allowed to cool to ambient temperature. For chemical activation, based on the literature review, each char obtained from carbonization was impregnated with KOH (KOH:char = 2:1) by weight. In brief, the weighed amount of KOH was dissolved in minimal Milli-Q water and thoroughly mixing with the weighed amount of char to form a thick paste. The paste was dried in an oven at 105 °C for overnight, and then carbonized in a tubular furnace to 800 °C (5 °C min^{-1}) with 50 mL min^{-1} argon, and dwelled for 2 h followed by cooling down to ambient temperature. The carbonized product was ground using a mortar and pestal, which was then washed with 1 M HCl for removing inorganics present. It was washed repeatedly with Milli-Q water until the washed solution measured neutral pH value. The washed product was vacuum dried at 80 °C for overnight. Additionally, AC was also synthesized from the orange peel derived char (OPC) by impregnating KOH:OPC = 1:1 (by weight) following the same procedure described above. The ACs derived from GP, LP, OP (OPC:KOH = 1:1.5), OP (OPC:KOH = 1:2), PP and TP were designated as GP-AC, LP-AC, OP-AC1, OP-AC, PP-AC, and TP-AC, respectively. All the synthesized ACs were separately collected in dry and clean bottles, and stored in a desiccator until used for further studies.

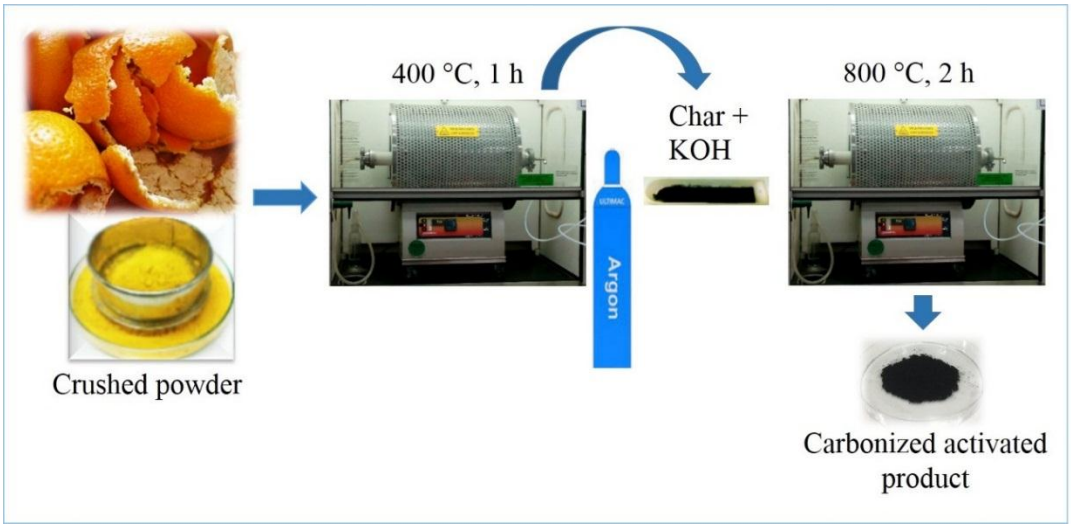

Figure 3.1. Schematic flow diagram showing preparation of AC from bio-waste, orange peel waste.

Earlier studies have also reported the use of KOH as activating agent for synthesis of porous carbons from biomass (Table 2.5). However, for the activation, different conditions, such as pre-treatment of the sample, activating agent to sample ratios, activation temperatures, are used. In this study, the precursor was pre-treated at 400 °C in an argon atmosphere for densification of the mass followed by KOH impregnation of the char produced and then pyrolysis for chemical activation. *So far, the pre-treatment approach (400 ℃) adopted in this study has not been reported in previous studies*.

3.7 Physico-chemical characterizations

3.7.1 N_2 adsorption-desorption studies

Nitrogen adsorption-desorption studies is a common practice used for gathering textural properties such as surface area, pore volume, pore size and pore size distribution of the AC samples. For nitrogen adsorption-desorption studies, ACs were firstly degassed at desired temperature (for example; 100 °C) and desired duration (h), and then exposed to N_2 gas in different pressures (P/Po = 0 to 1, where Po is adsorbate saturated vapor pressure and P is adsorbate equilibrium vapor

pressure) at -196 °C, the liquid-nitrogen temperature for several hours. While the pressure increases, the N_2 molecules adsorb on the surface of the sample. Upon adsorption equilibrium, the universal gas law is used to know the amount of N_2 gas adsorbed. Similarly, the desorption isotherm from decreasing the pressure provides desorption of the adsorbed N_2 molecules. From the resultant adsorption and desorption isotherms, textural properties are obtained using some physical models.

In this work, the AC samples were first degassed (250 °C, 18 h) and analyzed with nitrogen as adsorbate at 77.35 K using Quadrasorb Automated Surface Area and Pore Size Analyzer (Nova-3000 Series, Quantachrome). Surface area of the ACs was obtained from the Brunauer-Emmette-Teller (BET) method with the adsorption in the relative pressure (P/P_o) of 0.10. The total pore volume (V_T) was derived from the amount of nitrogen adsorbed at a relative pressure of 0.95. The micropore volume (V_{micro}) and micropore surface area (S_{micro}) were obtained from t-plot method with a relative pressure of 0.15-0.5. The pore size distribution (PSD) was measured from the desorption points using Density Functional Theory (DFT) method.

3.7.2 Morphological characterization

Scanning electron microscopy (SEM) is one of the widely used techniques to characterize the morphological features of AC samples. SEM provides information about sample morphology, composition, orientation and crystallinity. The images are captured by the emission of secondary electrons. In the examination process, the sample gets bombarded with beam of electrons which generates secondary electrons from the sample. The secondary electrons are then collected and amplified. The electron probes scan the secondary electrons over the sample surface, and the SEM image is obtained. In this study, the surface morphology of the ACs was examined by obtaining the electron micrographs using field emission - scanning electron microscopy (FESEM, JEOL-7600F) operated at 5kV. FESEM 7600F equipped with electron disruptive X-ray spectroscope (EDX, Oxford Xmax80 LN2 Free) was used for elemental mappings of the samples.

Transmission electron microscopy (TEM) is used to characterize the nanostructure of carbon materials. During analysis, an electron beam is focused on a specimen and part of the electron beam is transmitted. This transmitted portion is focused by objective lens into an image and the image is passed down through enlarge lenses and a projector lens, being enlarged all the way. In this study, TEM images of the ACs (OP-AC1, OP-AC and T-OP-AC) were further obtained using a TEM system (TEM JEOL 2100 UHR) operated at an accelerated voltage of 200 kV.

3.7.3 Structural properties

3.7.3.1 X-ray diffraction analysis

X-ray diffraction (XRD) analysis provides information related to structural properties (crystallinity or crystal structure) of carbon materials. XRD can be understood from Bragg's diffraction model. During the analysis, X-ray beam is projected to the sample and interference effect between atom of crystal and X-ray is measured. When the X-rays incident on the sample, they get reflected from lattice planes separated by the inter-planar distance (d), where the reflected X-rays interfere constructively. The reflected X-rays remain in phase because the path difference of reflected beam is equal to an integer multiple of the wavelength (λ) and then reflected X-ray experiencing constructive interference.

In this study, the crystallographic information of the ACs was obtained using a X−ray diffractometer (Bruker AXS D8 Advance) equipped with Cu-K_α (λ = 1.5418 Å) X−ray source operated at 40 kV and 40 mA. The other instrument used for samples testing was Power and Thin film Shimadzu XRD-6000 X-ray diffractometer with Cu-Kα irradiation (λ = 1.5406 Å) operated at 40 kV and 30 mA. The XRD analysis of the ACs was carried out by smearing the samples at ambient temperature for the scanning angle (2θ) ranging from 10 to 80° at a scanning speed of 10° min^{-1}.

3.7.3.2 Raman spectroscopy

Raman spectroscopy is considered to be one of the powerful techniques to investigate structural properties of carbon materials. In Raman spectra, usually the

wave number of the Raman shift (1000-2000 cm^{-1}) is plotted against the respective intensities originated from the interaction of photon with molecule vibrations (or phonon in a crystal). The monochromatic light, usually from a laser in the visible, near infrared or near ultraviolet range when incident on the sample if it gets scattered without losing any energy it is called as inelastic scattering or Raman scattering. If laser light interacts with molecule vibrations (or phonon in a crystal) in the sample, resultant energy of the laser photons could shifted up or down. This shift in energy provides information regarding the molecule vibration or phonon modes in the tested sample.

In this study, Raman spectra were obtained using a Witec Alpha300 SR (Argon Laser, 514 nm, 25 mW). Alternatively, Confocal Raman Spectroscopy (WITec, Witec alpha300 SR) was used to collect the sample surface information on chemical properties of the ACs non-destructively, with a resolution down to the optical diffraction limit (approx. 200 nm).

3.7.4 Surface chemistry

3.7.4.1 Fourier transformer infrared spectroscopy

Fourier transformer infrared (FT-IR) spectra provide data on the surface chemistry of the sample revealing the presence of surface functional groups. The FT-IR spectrum arises due to the rotational or vibrational motion of the atom in molecule. In brief, when the sample is irradiated by infrared (IR) radiation with continual frequency change, the molecules absorb certain frequencies based on the rotation or vibration motion of atom in molecules. In general, FT-IR spectrometer records the transmitted IR beams corresponding to the absorbed IR against wave number. Functional groups present on the sample surface are determined from the wave number recorded.

In this study, FT-IR spectra of sample powders and the ACs were obtained by scanning the sample pellets prepared with KBr (FT-IR grade). Briefly, weighed amounts of sample AC and KBr powder were ground into homogenous fine particles using a pestle and mortar. A constant sample to KBr amounts with ratio of 2 mg:280 mg was used so as to compare corresponding intensities of functional

groups in samples semi-quantitatively. Thin pellet was prepared from the powder using the CARVER Evacuable Pellet Dies and CARVER hydraulic lab press. The pellet was scanned from 4000 cm^{-1} to 400 cm^{-1} with a resolution of 4 cm^{-1} using a Bruker spectrometer, and the background was corrected from the spectra of samples.

3.7.4.2 X-ray photoelectron spectroscopy

X-ray photoelectron spectroscopy (XPS) analysis provides quantitative information on the top most surface layer (i.e., up to 10-12 nm) of carbon materials regarding atomic composition, oxidation state and electronic structure. In XPS analysis, inner shell electrons are ejected from the sample by irradiating X-ray beam called as energy impinges. The energy of the ejected electrons from atom is then calculated by difference in the energy of the impinging X-ray and the ejected electron that gives the binding energy of the electron to the atom. The binding energy of the ejected electron depends on the energy of the electronic orbit and the element, which can be used to identify the element involved. Additionally, the chemical structure of the atom also affects the binding energy, and this can be used to identify the valence of the atom and its accurate chemical structure.

In this study, XPS analysis of the ACs was performed to further investigate the surface functionalities. XPS analysis was carried out using Multilab 2000, Thermo Scientific, UK with monochromator and AlKα radiation (hν = 1486.6 eV). XPS analysis of the samples was also carried out using recent advanced instrument, a Kratos Axis Supra spectrophotometer with a dual anode monochromatic Kα excitation source. In the testing, all binding energies for elements of interest were corrected against an adventitious carbon C 1s core level at 284.8 eV. All XPS peaks were fitted using Shirley background together with Gaussian-Lorentzian function using CASA XPS software.

3.8 Electrode preparation

The working electrodes from the sample ACs were prepared by drop-casting method. Typically, the desired amount of active material (AC) and PVDF as a

binder with or without adding carbon black as conductive agent were thoroughly mixed and dispersed in measured amount of NMP solution to produce a homogenous slurry. The resulting slurry was then coated onto known area of the electrode supporting material – bipolar plate or toray paper. The slurry coated electrodes were dried in an oven at 60 °C for overnight.

3.9 Electrochemical measurements

The electrochemical characterization of the ACs as electrode materials was carried out by testing the fabricated devices for cyclic voltammetry (CV), Galvanostatic charge-discharge (GCD) and Electrochemical Impedance spectroscopy (EIS). All experiments were carried out at room temperature. One of the experimental set up used for electrochemical performance testing from this study is shown in Figure 3.2.

Figure 3.2. Electrochemical cell with three electrodes set up for CV and EIS measurements.

3.9.1 Cyclic voltammetry

Cyclic voltammetry (CV) is used as one of the main electrochemical tests to evaluate electrochemical properties of the electrodes. CV testing is carried out

within a specified potential window and at specific scan rate, where potential is varied linearly with respect to time and potential range is fixed to avoid the possible gas evolution. The obtained plot from scanning, *i.e*., Potential (V) vs. Current (I) is known as cyclic voltammogram, where current is a response on Y-axis. If cyclic voltammogram is rectangular shaped, it indicates a good capacitive behavior of an ideal double layer capacitor. Cyclic voltammogram in quasi-rectangular shape or showing peaks (*i.e*., redox peaks) at certain potentials suggests pseudo-capacitance behavior of pseudocapacitor due to the redox reactions.

3.9.2 Galvanostatic charge-discharge

In electrochemical measurement of energy storage devices, galvanostatic charge-discharge (GCD) is a commonly studied test. This testing is carried out at constant current charge/discharge, where the potential (V) is obtained as a response on Y-axis. In a charge/discharge plot of Time (t) *vs.* potential (E), linear charge-discharge curves with triangular shape indicates the good capacitive behavior of an ideal double layer capacitor. If sharp drop occurrence in potential, it is nothing but internal resistance (iR) drop. The result with a non-linear charge-discharge curves implies the pseudo-capacitance behavior of pseudocapacitor due to the redox reactions.

3.9.3 Electrochemical impedance spectroscopy

Electrochemical impedance spectroscopy (EIS) is a rapid technique used to study the frequency behavior and corresponding resistance values of electrodes. EIS test provides detail information on the ohmic resistance, charge transfer, diffusion, kinetics of reaction etc., and are expressed graphically in a Bode plot or a Nyquist plot. During the testing, data are usually recorded at the open-circuit voltage (OCV) via applying a small sinusoidal excitation of alternative potential (5 ~ 10 mV) to the system at certain frequency range, e.g. 1 MHz to 100 mHz.

Tests carried out for characterizations of the bio-waste samples and the ACs are shown in Figure 3.3.

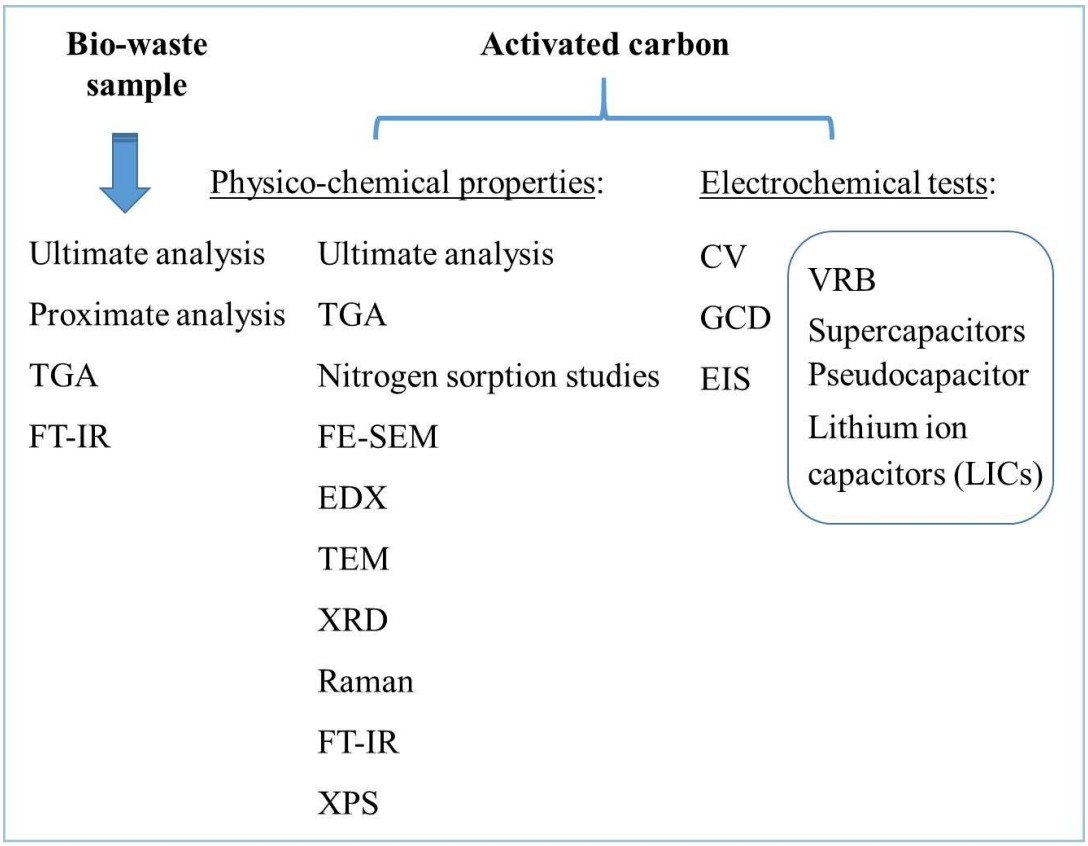

Figure 3.3. Chart showing the tests carried out for bio-waste and AC samples.

CHAPTER 4

Screening of Samples and their Physico-chemical Characterizations

4.1 Elemental composition in bio-waste samples

Table 4.1 shows the results with the highest carbon content of 43.49% for Lychee peel powder (LP), followed by Thai Longan peel powder (TP), grapefruit peel powder (GP) and orange peel powder (OP) with 42.96%, 41.57, 40.89% and 40.89%, respectively. Carbon content for papaya peel was measured as 37.25%, followed by water melon peel (36.41%). Honey Dew peel measured the lowest carbon content (34.58%) among the 11 tested samples. Five samples (OP, GP, PP, LP and TP) were screened for the preparation of ACs in consideration of higher carbon content and availability in abundance. Orange, grapefruit and lemon belong to the same citrus species, therefore lemon peel was not chosen since orange and grapefruit peels have been selected to represent the citrus species.

Table 4.1. Elemental composition of the 11 fruit peels.

Sample source	Elemental composition (wt%)			
	C	**H**	**N**	**S**
Apple *(Malus pumila)* peel	39.80	6.75	0.26	0.34
Banana *(Musa acuminata)* peel	39.16	5.90	0.91	0.36
Grapefruit *(Citrus paradise)* peel	**41.57**	6.04	0.55	0.23
Honey Dew *(Cucumis melo)* peel	34.58	5.75	1.85	0.42
Lemon *(Citrus limon)* peel	40.79	6.27	0.72	0.21
Lychee *(Litchi chinensis)* peel	**43.49**	6.07	1.10	0.29
Orange *(Citrus sinensis)* peel	**40.89**	6.09	0.77	0.22
Papaya (*Carica papaya*) peel	37.25	6.14	2.38	0.54
Pineapple *(Ananas comosus*) peel	**40.57**	6.06	0.71	0.27
Thai longan *(Dimocarpus* longan) peel	**42.96**	5.81	0.93	0.36
Water melon (*Citrullus lanatus)* peel	36.41	5.82	2.15	0.37

4.2 Proximate results of bio-waste samples

Proximate analysis of the selected bio-waste samples exhibited high contents of VM which are above 80.0% (Table 4.2). High content of VM in the sample contributes in pores development in the carbonized product with the release of gases through gasification during pyrolysis.

Table 4.2. Proximate results of five selected fruit peel powders.

Sample source	Moisture %	VM %	FC %	Ash %
Grapefruit peel	6.00	87.90	6.00	6.10
Lychee peel	12.96	83.30	12.96	3.74
Orange peel	7.85	87.66	7.85	4.49
Pineapple peel	9.35	85.77	9.35	4.88
Thai longan peel	9.19	84.08	9.19	6.72

4.3 Elemental composition in the as-synthesized ACs

Table 4.3 presents elemental composition in the ACs synthesized from KOH activation (precursor peel powder derived char:KOH = 1:2 by weight). The carbon content increased from 41.57% in GP to 67.81% in GP-AC, 43.49% in LP to 67.43% in LP-AC, 40.89% in OP to 82.83% in OP-AC, 40.57% in PP to 72.69% in PP-AC, and 42.96% in TP to 71.56% in TP-AC.

Table 4.3. Elemental compositions in the as-synthesized ACs from five selected fruit peel powders.

Sample source	Elemental composition (wt%)							
	Powder sample				Synthesized AC			
	C	H	N	S	C	H	N	S
Grapefruit peel	41.57	6.04	0.55	0.23	67.81	2.77	0.37	0.31
Lychee peel	43.49	6.07	1.10	0.29	67.43	3.00	0.29	0.30
Orange peel	40.89	6.09	0.77	0.22	82.83	1.33	0.54	0.25
Pineapple peel	40.57	6.06	0.71	0.27	72.69	3.37	0.40	0.26
Thai longan peel	42.96	5.81	0.93	0.36	71.56	3.03	0.31	0.30

4.4 Carbonization behavior of precursors

In order to understand pyrolytic characteristics of the selected bio-waste samples (OP, LP, GP, PP and TP), TGA analysis was carried out from 50 to 950° C at a heating rate of 20 K min^{-1} in an inert atmosphere with nitrogen flow throughout the experiment. TGA results revealed that all the tested samples exhibit more or less similar weight loss behaviors along carbonization temperatures as shown in Figure 4.1. It can be observed that there was gradual weight loss before 200 °C, which could be attributed to moisture or volatile gases release. The maximal weight loss occurred in the temperature range of 200 to 380°C due to the decomposition of pectin, hemicellulose and cellulose fractions in the sample powders. The weight loss further continued with the rise of temperature, and tapered above 700 °C. This could have been due to the loss of remaining organic fractions in the samples. Weight loss was minimal at temperatures above 800 °C (except that for PP), which could be due to the occurrence of carbon escaping in the process.

During carbonization, bio-waste precursors get thermally decomposed, which eliminates VMs that include heteroatoms. With further temperature rise, there occurs loss of residual VMs and remains solid carbons. With the precursor materials with good properties and optimal activation conditions, the resultant

carbons with a highly porous structure could be obtained. Based on the observed pyrolytic characteristics of the samples, pyrolysis temperature for the preparation of ACs was set at 800° C for this study.

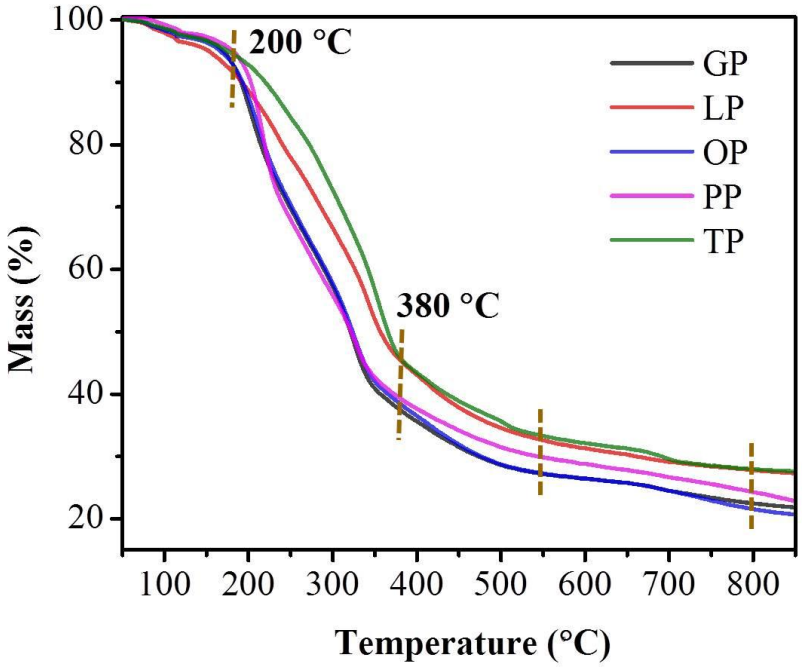

Figure 4.1. TGA curves of the five selected bio-waste powders.

4.5 Physico-chemical characterizations of the as-synthesized ACs

4.5.1 Nitrogen adsorption-desorption studies

Nitrogen sorption isotherms studies of the as-synthesized ACs were carried out to ensure the formation of porous carbons and investigate their textural properties. Figure 4.2 illustrates N_2 adsorption-desorption isotherm curves of the as-synthesized ACs. The observed curves illustrate combination of type I and type IV isotherms, indicating the presence of micropores and mesopores in the resultant ACs. The isotherm plot observed for OP-AC is different from other samples with a tiny hysterisis loop, which indicates the dominance of narrow slit pores. The observed different PSD for OP-AC than other samples is due to the higher amount of nitrogen adsorbed and also varied pore sizes. The OP-AC has higher V_T compared with other four samples. Textural properties of AC also depend on the

precursor material composition besides activation variables (temperature, time, activating agent, *etc*).

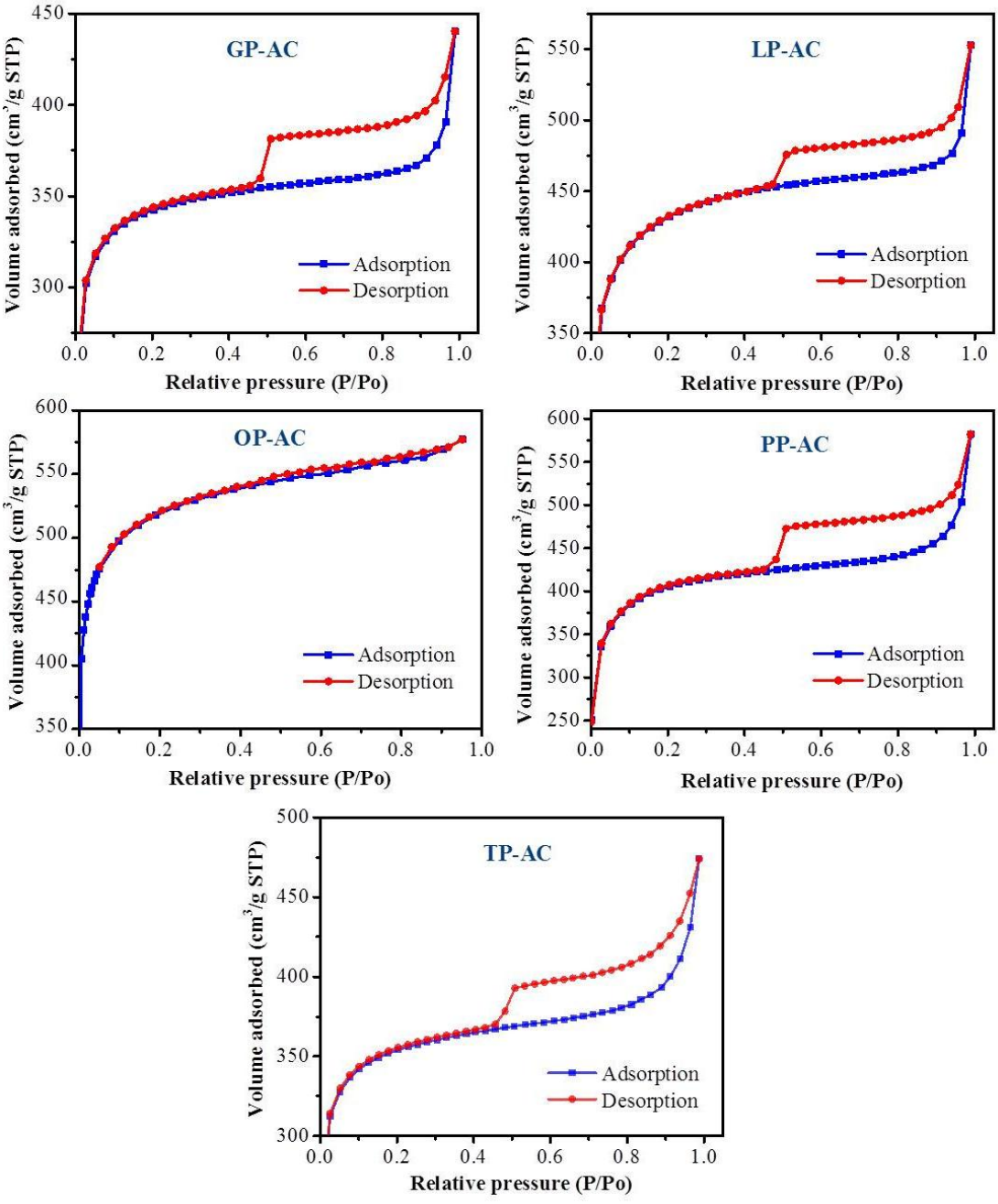

Figure 4.2. Nitrogen adsorption-desorption isotherms of the as-synthesized five ACs.

Textural properties of the as-synthesized ACs are given in Table 4.4. The as-synthesized ACs are porous with predominance of micropores, The BET surface area of 1901 $m^2 g^{-1}$ for OP-AC is the highest among the synthesized ACs, followed by 1601 $m^2 g^{-1}$ for LP-AC, 1504 $m^2 g^{-1}$ for PP-AC and 1344 $m^2 g^{-1}$ for TP-AC. Surface area of 1301 $m^2 g^{-1}$ for GP-AC is the lowest among the synthesized ACs. Other pore characteristics, such as micropore surface area, pore volumes and pore width of the ACs are presented in Table 4.4. The total pore volume (V_T) of 0.94 $cm^3 g^{-1}$ for OP-AC is the highest among the samples. Pore size is mainly concentrated in less than 2 nm for all the samples (Figure 4.3). The results infer that textural properties of the activated carbons also depend on the precursor materials besides activation variables.

Table 4.4. Textural properties of the as-synthesized five ACs.

Sample	S_{BET} [a] ($m^2 g^{-1}$)	S_{micro} [b] ($m^2 g^{-1}$)	V_T [c] ($cm^3 g^{-1}$)	V_{micro} [d] ($cm^3 g^{-1}$)	V_{micro}/V_T (%)	Pore width [e] (Å)
GP-AC	1301	1209	0.68	0.49	72.06	11.78
LP-AC	1601	1436	0.86	0.60	69.77	11.78
OP-AC	1901	1407	0.94	0.59	62.77	11.26
PP-AC	1504	1360	0.90	0.57	63.33	11.78
TP-AC	1344	1233	0.74	0.50	67.57	11.78

[a] S_{BET} (Brunauere-Emmette-Teller) surface area.
[b] Micropore surface area.
[c] Total pore volume, measured at $P/P_0 = 0.95$.
[d] Micropore volume, derived from DFT model.
[e] Pore width of most pores (mode).

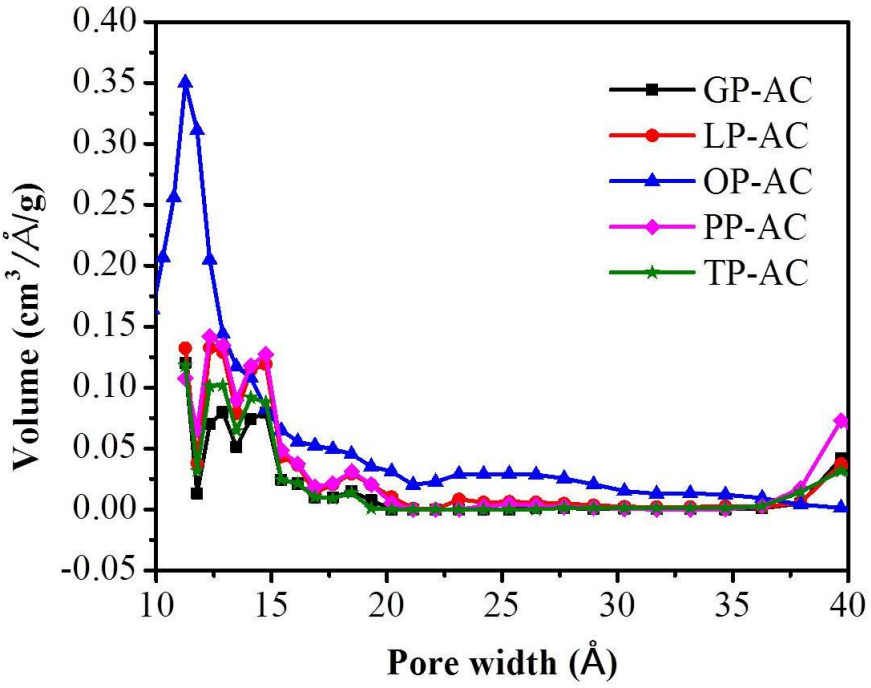

Figure 4.3. Pore size distribution of the as-synthesized ACs with KOH activation.

KOH as an activating agent play a significant role in the porosity development of ACs. In KOH activation process, the porous structure and formation of some large pores are ascribed to several simultaneous/consecutive reactions as shown in equation 1 to 5 [5, 7, 165]. At temperature above 400 °C, the reaction occurs between KOH and carbon, and the metallic K intercalate to the carbon matrix. As the activation temperature elevates above 650 °C, the metal complex contributes for further gasification (equation 2 and 3) transforming some of the micropore into mesopore. Briefly, the pore network is generated through three main activation mechanisms: (a) Etching the carbon framework by the redox reactions between various potassium compounds as activating reagents, (b) the gasification of carbon, and (c) intercalation of metallic K (equation 1, 4 and 5) into the carbon lattices of the carbon matrix. The intercalated metallic K and other K compounds get removed upon washing, whilst the expanded carbon lattices cannot return to their original nonporous structure [5].

$$6KOH + 2C \rightarrow 2K + 3H_2 + 2K_2CO_3 \qquad (1)$$

$$K_2CO_3 \rightarrow K_2O + CO_2 \qquad (2)$$

$$CO_2 + C \rightarrow 2CO \quad (3)$$

$$K_2CO_3 + 2C \rightarrow 2K + 3CO \quad (4)$$

$$C + K_2O \rightarrow 2K + CO \quad (5)$$

4.5.2 Morphological characterization

FE-SEM analysis was performed to characterize the morphological features of the as-synthesized ACs. It can be seen from the FE-SEM images in Figure 4.4 that the synthesized ACs are highly porous in nature. The pores developed are combination of small and large pores though they are mostly micropores; this has already been discussed in previous section with reference to Nitrogen sorption studies. It is crucial that the carbon materials as electrode possess interconnected porous network so that there occurs rapid ion diffusion during the electron transfer processes. Further, the high surface area of electrode materials provides more sites for electrolyte solution across the electrode/electrolyte interface and help in the electrical double layer formation.

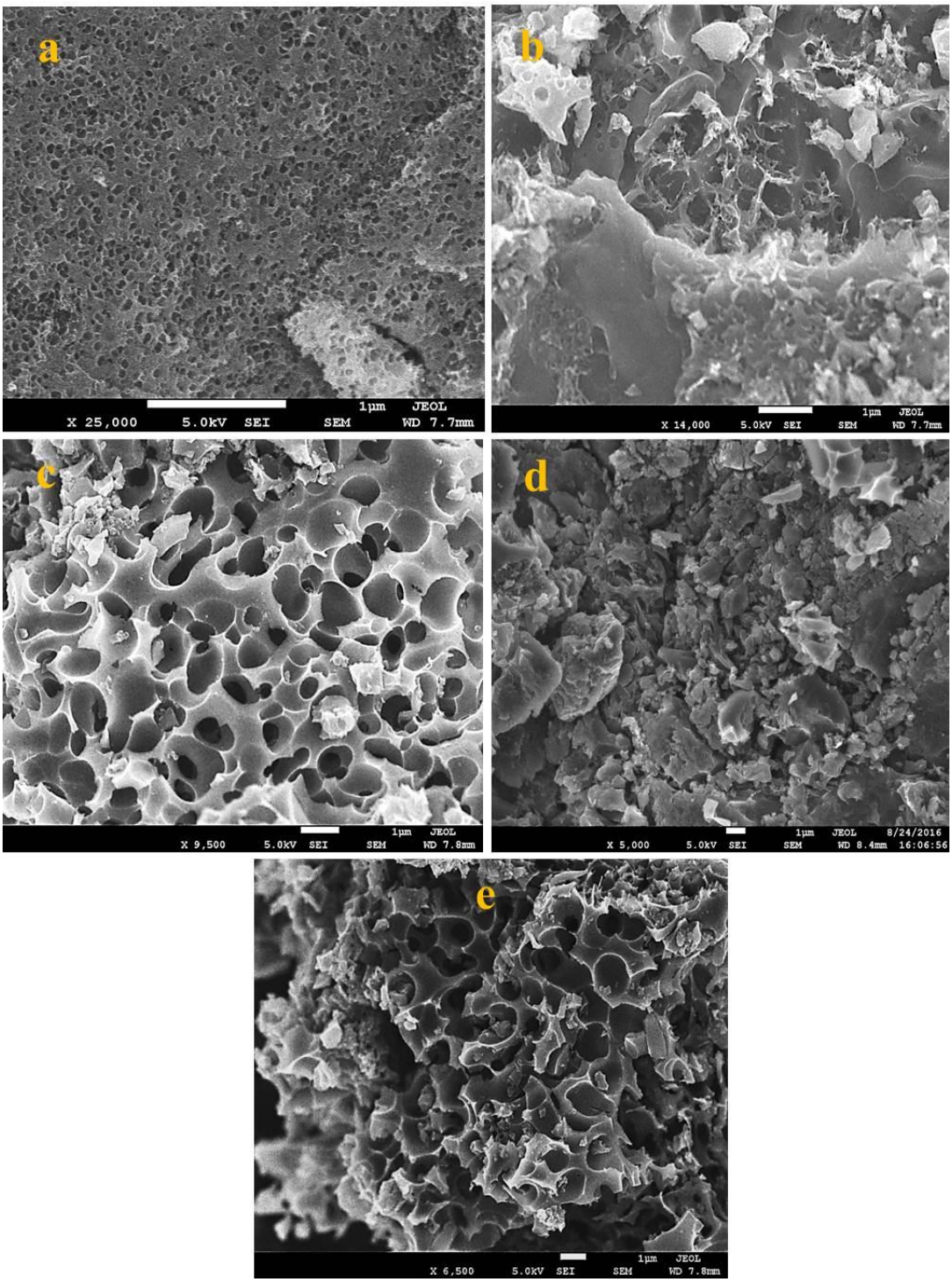

Figure 4.4. FE-SEM images of the as-synthesized ACs: GP-AC (a), LP-AC (b), OP-AC (c), PP-AC (d), and TP-AC (e).

4.5.3 Structural properties

4.5.3.1 XRD spectroscopy

The synthesized ACs were subjected to XRD analysis for checking the crystallographic features. The diffraction patterns obtained from analysis are shown in Figure 4.5. The diffraction patterns of the AC samples exhibit broad peaks, which indicate amorphous carbon. The peaks observed at 2θ values between 20 to 30° and 40 to 45° are associated with (001) and (110) planes of the graphite structure in the carbon based materials. The small hump observed at 2θ less than 20 degree in three samples GP-AC, LP-AC and TP-AC further suggest these samples consist of semi-graphitic carbon, whereas OP-AC and PP-AC without small hump are more amorphous [95, 166].

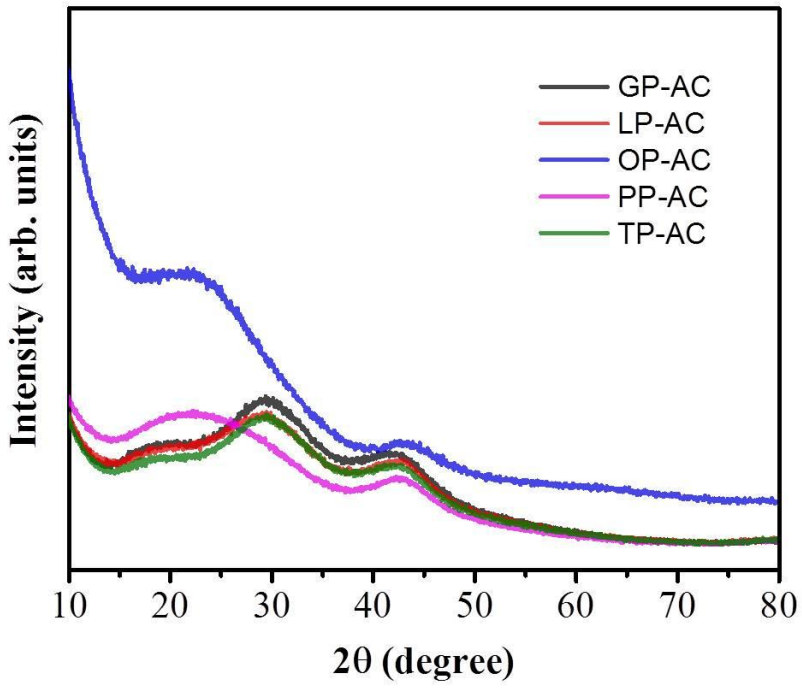

Figure 4.5. XRD spectra of the as-synthesized five ACs.

4.5.3.2 Raman spectroscopy

Raman spectroscopy provides useful information on the surface functional groups and defects in carbon materials. Figure 4.6 shows Raman spectra of all five AC samples analyzed. Characteristics features observed at ~1375 cm^{-1} and ~1604 cm^{-1}

are associated with the disorder-induced D band (D band) and the graphite band (G band), respectively. The presence of the former one is due to defects and disorder in the carbonaceous materials and the latter one corresponds to the optically allowed E_{2g} vibrations of the graphitic structure. The intensity ratio between D and G bands (I_D/I_G), a measure of defect concentration, is calculated to be 0.99. This clearly indicates that the as-synthesized ACs predominantly contain sp^2 type carbon, such high degree of sp^2 type carbon translates the higher electrical conductivity for the sample.

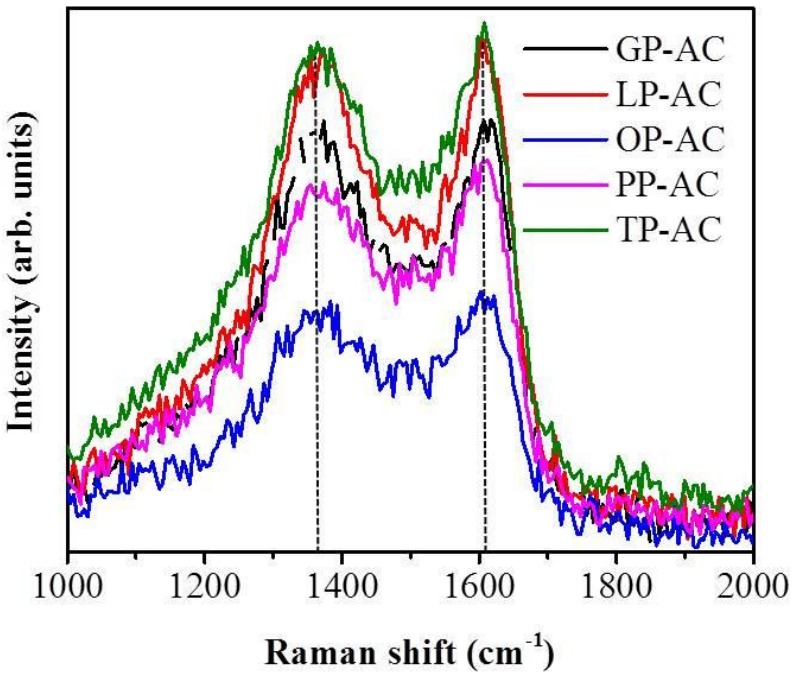

Figure 4.6. Raman spectra of the as-synthesized five ACs.

4.5.4 Surface chemistry

4.5.4.1 FT-IR analysis results

The selected five bio-waste samples and their ACs were subjected to FT-IR analysis following the procedure described in Section 3.7.4.1, Chapter 3. The obtained FT-IR spectra show the presence of various surface functional groups in all the precursors and the as-synthesized ACs (Figure 4.7). For the synthesized ACs, the spectra markedly decreased compared to their respective precursors spectra, which is due to the dehydration attributed to heat treatment and carbonization. Table 4.5

presents the IR assignment regions of functional groups identified on carbon surfaces in previous publications [167], and the assignment regions identified in the samples. The peaks observed at 3418 cm^{-1} in 3025-3776 cm^{-1} and signals at 3443 cm^{-1} correspond to stretching vibrations of alcohols or phenolic groups (O-H bend/stretch). The bands 1101, 1064 and 1028 cm^{-1}, and at 1036 cm^{-1} are possibly attributed to alcohols (C-OH stretch), alcohols and C-O in ethers (stretch). The absorptions originating from the C-H stretching vibrations of saturated hydrocarbons, ethers and lipids are exhibited at 2924, 2850, 2918 and 2928 cm^{-1}. The 1447 and 1374 cm^{-1} absorptions and the signals observed at 1432 cm^{-1} relate to carbonates. Also, the peaks at 1328 and 1265 correspond to the stretching vibrations of lactones or carbonates. The absorptions at 1638, 1626 and 1637 cm^{-1} suggest the presence of quinones. The heat treatment also resulted in loss of some functional groups, for example; the signal at 1739 cm^{-1} representing carboxylic acids (COOH) in OP was disappeared in OP-AC. At higher carbonization temperature, there may have occurred decomposition of oxygen and resulted in dehydration in the case of ACs. The functional groups, particularly oxygen groups contribute in enhancing the capacitance of carbon through favorable double layer formation, redox reactions (pseudo-capacitance) and improved wettability of the electrode by an electrolyte.

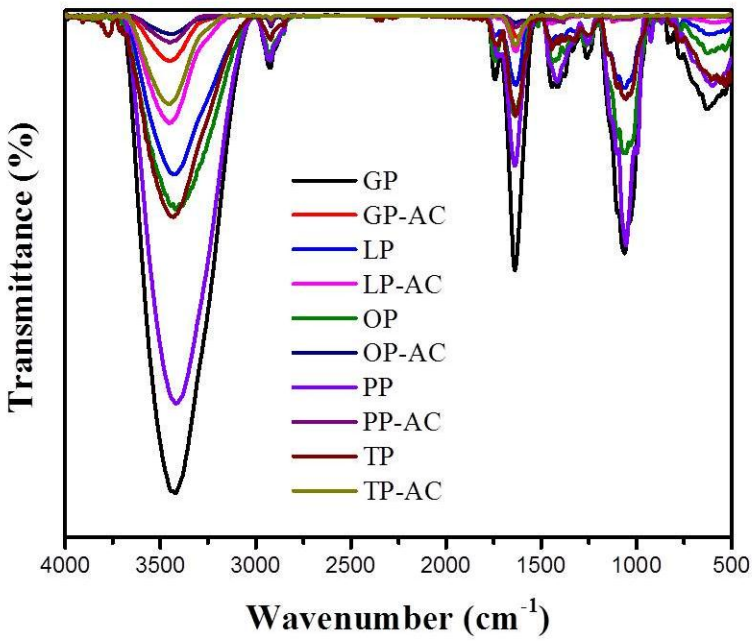

Figure 4.7. Comparative FT-IR Spectra of the five precursors and their ACs.

Table 4.5. The IR assignment regions of functional groups on carbon surfaces [167], and observed on the precursors and the as-synthesized ACs.

Functional group	Assignment region (cm^{-1})	Samples	
		Precursors	ACs
Alcohols (C-OH stretch)	1000-1220	940-1197	1004-1175
Alcohols	1049-1276		
C-O in ethers (stretch)	1000-1300		
Carboxylic acids (COOH)	1120-1200		
Carbonates	1100-1500	1208-1497	1358-1497
Lactones	1160-1370		
Quinones	1550-1680	1508-1787	1508-1690
Aromatic (C=C stretch)	1585-1600		
Carboxyl-carbonate	1590-1600		
Carboxylic acids (COOH)	1665-1760		
Lactones	1675-1790		
C-H stretch	2600-3000	2810-2993	2821-2982
Carboxylic acids (COOH)	2500-3300	3025-3776	3197-3647
Phenolic groups (O-H bend/stretch)	2500-3620		
Amines	3200-3400		
Alcohols	3200-3640		

4.5.4.2 XPS analysis results

The surface elemental compositions and a quantitative analysis of the functional groups present on the surface of as-synthesized AC samples were further studied by

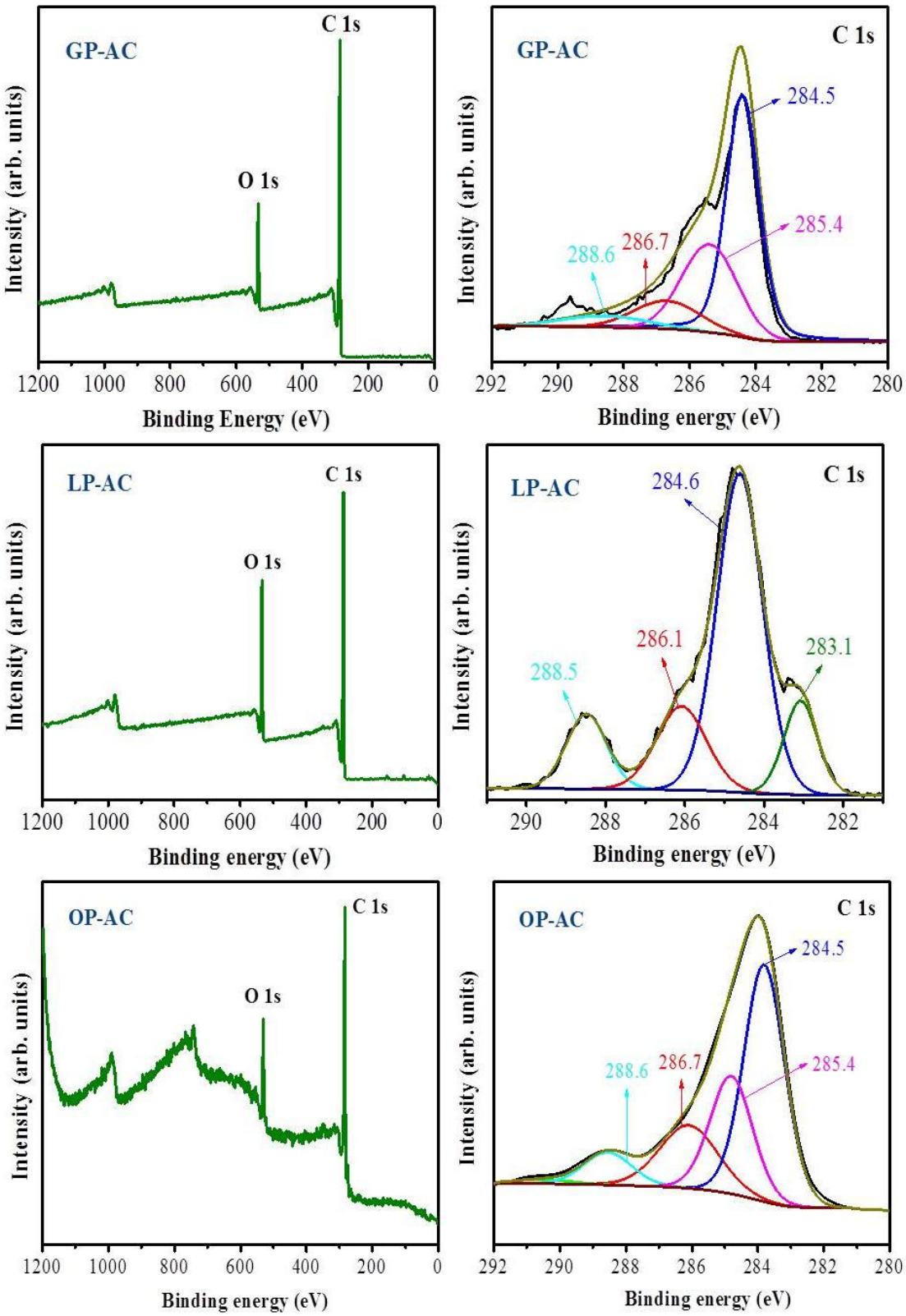
GP-AC
C 1s
O 1s
Intensity (arb. units)
1200 1000 800 600 400 200 0
Binding Energy (eV)
GP-AC
C 1s
284.5
285.4
286.7
288.6
Intensity (arb. units)
292 290 288 286 284 282 280
Binding energy (eV)
LP-AC
C 1s
O 1s
Intensity (arb. units)
1200 1000 800 600 400 200 0
Binding energy (eV)
LP-AC
C 1s
284.6
286.1
283.1
288.5
Intensity (arb. units)
290 288 286 284 282
Binding energy (eV)
OP-AC
C 1s
O 1s
Intensity (arb. units)
1200 1000 800 600 400 200 0
Binding energy (eV)
OP-AC
C 1s
284.5
285.4
286.7
288.6
Intensity (arb. units)
292 290 288 286 284 282 280
Binding energy (eV)

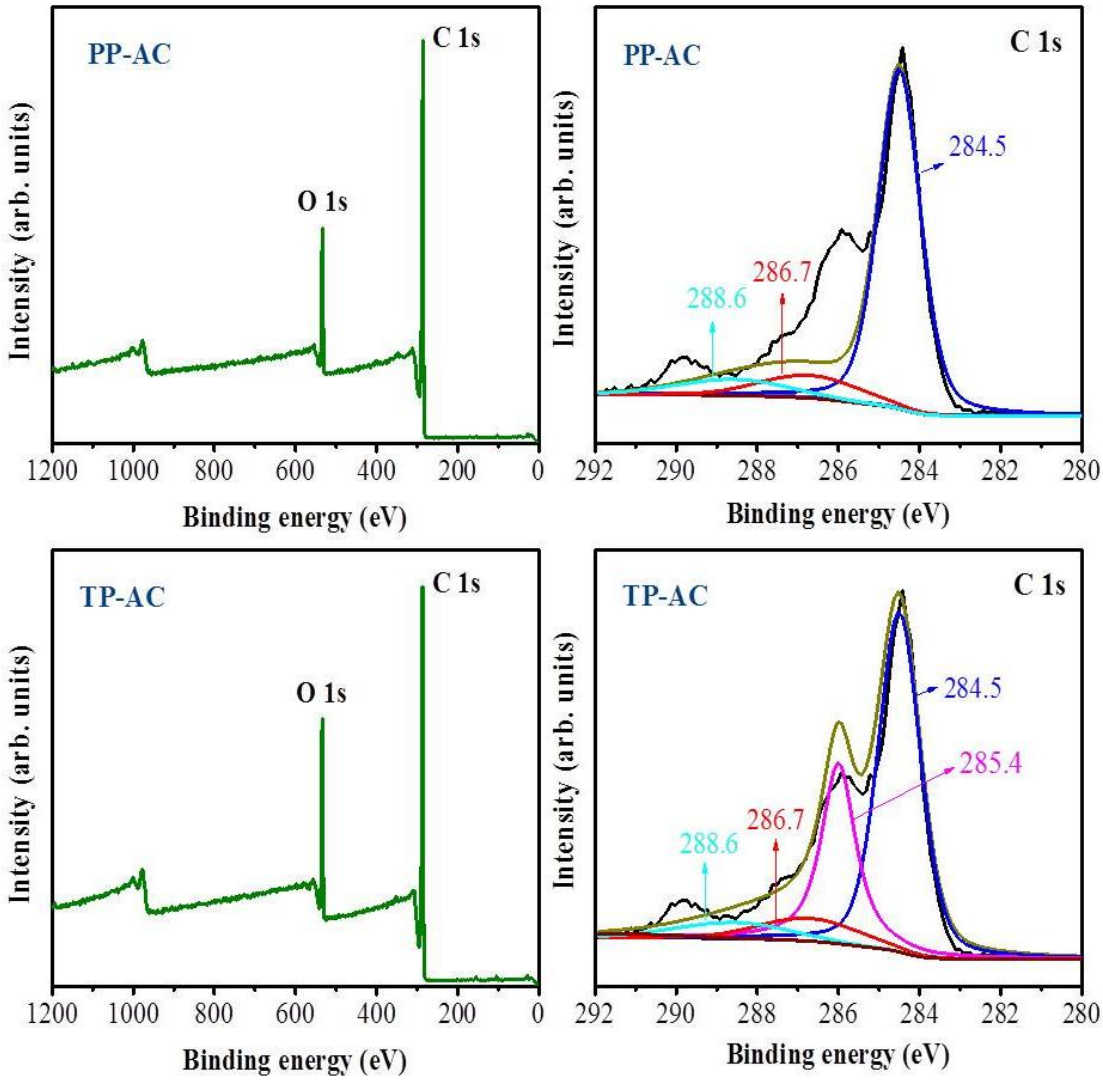

Figure 4.8. XPS analysis results of the as-synthesized five ACs: XPS survey spectra (Right side) and curve fitting of C 1s spectra (Left side).

XPS analysis as described in Section 3.7.4.2, Chapter 3. Wide survey spectra of all the ACs obtained from analyses are presented in the binding energy range of 0 to 1200 eV in Figure 4.8. All the spectra of GP-AC, LP-AC, OP-AC, PP-AC and TP-AC show the presence of carbon (C) and oxygen (O) as major elemental compositions.

Table 4.6 presents the normalized C and O atomic compositions of the five AC samples. The OP-AC exhibits a higher percentage of O/C ratio (0.15) compared

Table 4.6. The elemental quantification of the XPS measured bio-waste derived ACs.

Sample	Elemental concentration (atomic %)		
	C	O	O/C ratio
GP-AC	88.8	11.2	0.13
LP-AC	87.4	12.6	0.14
OP-AC	87.2	12.8	0.15
PP-AC	88.7	11.3	0.13
TP-AC	86.0	14.0	0.16

Table 4.7. Surface functional groups (%) obtained from curve fitting of C 1s XPS spectra.

Sample	C=C (sp^2) 284.6 eV[#]	C–C (sp^3) 283.1 eV[#]	C–O 286.1 eV[#]	C=O 288.5 eV[#]
GP-AC	53.7	29.3	11.2	5.8
LP-AC	58.3	12.1	16.8	12.8
OP-AC	58.0	18.9	12.0	11.1
PP-AC	80.2	-	11.2	8.6
TP-AC	61.5	24.6	11.5	2.4

[#] The binding energy for LP-AC.

with other samples except that for TP-AC (0.16). Furthermore, in order to identify the surface functionalities on the synthesized AC samples, high resolution de-convoluted C 1s spectra are obtained from curve fittings. The C1s spectra of the samples are fitted by three to four individual component peaks. Referring to previous study [168], for four ACs (GP-AC, OP-AC, PP-AC and TP-AC) the peak at 284.5 eV is assigned to sp^2 C=C and the peak at 285.4 eV to sp^3 C–C. Other peaks at 286.7 and 288.6 eV are assigned to C–O and C=O, respectively. Similarly, referring to earlier studies [169, 170], the peaks for LP-AC are assigned to sp^2 C=C (284.6 eV), C-O (286.1 eV), C=O (288.5 eV) and sp^3 C-C (283.1 eV). The

percentages of surface functionalities calculated are specified in Table 4.7. It can be seen that the ACs contain a large number of oxygen functionalities (11.2 to 16.8%), and the presence of these surface oxygen groups is favourable for better performance of electrodes.

4.6 Conclusions

Based on the higher carbon contents, fruit types and availability, five samples (OP, LP, GP, PP and TP) were screened for the synthesis of ACs from initially collected 11 samples. Porous ACs were synthesized via chemical activation from the five selected samples (GP, LP, OP, PP and TP), and the as-synthesized ACs were subjected to extensive characterization in order to investigate the physico-chemical properties, which play crucial roles in electrochemical performance. Based on the obtained characterization results (high surface area, suitable morphology, well developed pore structures and favourable surface chemistry), two ACs synthesized from OP and LP were further screened for evaluating them as electrodes for energy storage applications. In addition, research gaps identified from literature review were also considered in selecting these two precursors, for example; limited or no published data for energy storage applications.

CHAPTER 5

Bio-waste Derived Porous Carbon as Electrode for Vanadium Redox Flow Battery

A part of findings in this chapter were published as an original research paper: M. Maharjan, A. Bhattarai, M. Ulaganathan, N. Wai, M.O. Oo, J.-Y. Wang, T.M. Lim, High surface area bio-waste based carbon as a superior electrode for vanadium redox flow battery, Journal of Power Sources 362 (2017) 50-56.

Other results are included in the original research paper: M. Maharjan, Y. Zhang, M. Ulaganathan, T. M. Lim, Improved electrocatalytic activity via facile surface modification of waste derived activated carbon as electrodes for all vanadium redox flow battery, Applied Surface Science, under review.

5.1 Introduction

Energy storage systems, such as flow batteries, supercapacitors (Li-ion and Na-ion), etc. play an important role in renewable energy integration. The technical and financial constraints, however, have limited extensive utilization of all these systems [171, 172]. Redox flow batteries are considered to be promising candidates for large scale energy storage and have higher cycle efficiency and long-life. Among the redox flow batteries, the vanadium redox flow battery (VRB) has drawn huge interest in recent years due to its unique advantages, such as use of the same V ion in both half-cell solutions that does not have the issue of the cross-mixing of two half-cell electrolytes, higher efficiencies, ambient temperature operation, longer cycle life and environmentally-friendly technology [20, 173]. However, at present, VRB is considered expensive, mostly due to the costs of stack-related components [174] and electrolyte. Commercial graphite bipolar plates used in VRB stack at present are mainly obtained from non-renewable resources, and they are also heavy in weight and expensive. This has given opportunities to investigate VRB in several aspects, such as development of cost effective and efficient electrodes [6, 38, 175],

and others [176, 177]. Thus, it is essential to search low cost alternative materials to help reduce the cost of VRB system. It is also equally important to investigate and develop efficient materials (such as, electrode) for performance enhancement.

The electrode, that provides reaction sites for the redox reactions, is one of the key components of battery. The properties of electrode play crucial roles in determining electrochemical performance of energy storage devices, such as supercapacitors, lithium ion capacitors, redox flow batteries, etc. For energy storage applications, various materials have been investigated as electrode, such as activated carbon (AC), graphene, carbon nanotubes, carbon fibers, metal oxides (MnO_2, MnO, NiO, Fe_3O_4, RuO_2), etc [178]. Nevertheless, carbon-based electrode is more commonly used in industry than other materials due to its low cost and environmental friendliness. However, the current carbon-based electrodes are produced from non-renewable sources. Thus, in light of growing concerns on limited fossil fuel reserves and increasing environmental pollution, significant efforts have been made to search promising sustainable precursors for carbon based electrode preparation for energy storage applications [7, 104].

AC possesses attractive features (e.g., high surface area, good conductivity, low cost) towards the effective treatment of aqueous solutions and improvement of electrochemical performance, among others. Researchers have extensively investigated AC preparation with tailored textural properties via various synthesis routes, and have also explored different precursors [86, 90, 103]. Biomass is a low cost, abundant and environmentally-friendly renewable resource, which has drawn huge attention for AC preparation in recent years. Numerous literatures are available on the use of AC as electrode in supercapacitors for energy storage applications or for other purposes [9, 106, 178, 179]. However, studies on the use of bio-waste derived AC as electrode in VRB application are scarce [6]. As a low cost, environmentally-friendly and sustainable product, a study on the potential of using bio-waste derived AC as electrode in electrochemical devices (such as VRB) is needed. According to the Food and Agriculture Organization of the United Nations (FAO), citrus fruits production in 2016 was 124 million tonnes with ~67.0 million tonnes of oranges [145]. This shows availability of a huge quantity of fruit peels

bio-waste, which is renewable. In regions with large orange production, the peels pose a serious disposal problem [146]. Studies have reported the use of orange peels for producing hydrochars as adsorbent for metallic ions from aqueous solutions [99, 151-154], and ACs as adsorbents for dyes and organic contaminants [146, 149, 150]. In the present work, orange (*Citrus sinensis*) peel waste was employed as a precursor for the preparation of AC in consideration of its low cost, abundance and environmental-friendliness.

In VRB, graphite or carbon-based bipolar plates are commonly used as supporting electrodes, and graphite felts serve as active electrodes. The use of thick bipolar plates increases the weight of the stack, which limits power capability of the VRB system. Due to this reason, carbon-based conducting plastics are proposed for graphitic electrodes in commercial systems. Again, such plastics have concerns of poor conductivity that deliver lower cell efficiencies. There have been enormous attempts to catalyze charge transfer reactions for improving overall VRB performance [40, 180-182]. An earlier study reported the enhanced electro-catalytic activity of AC (derived from coconut shell) modified toray paper electrode in VRB with multicouple reactions [6]. Reports on the use of biomass-derived AC as electrode in VRB application are scarce [6]. *So far, orange peel derived AC has not been studied as electrodes in any flow battery applications*.

In order to meet the ever-increasing energy demand, researchers have devoted intensive efforts toward the development of efficient energy storage systems as well as performance enhancement of energy storage technologies [40, 181, 183]. [182]. Studies have investigated surface functionalization of carbonaceous materials through various approaches to improve the performance of these materials as electrodes [184-186]. Chemical activation, heat treatment and plasma treatment have been performed to enhance the electrochemical performance via the surface functionality [39, 187-189]. According to previous studies, acid treatment of carbon materials creates surface oxygen functional groups, such as hydroxyl, carboxylic, etc., which increase the polarity and hydrophilicity resulting in better electrochemical activity [39, 190, 191].

However, most of surface functionalization studies have used commercial carbon products, such as AC, carbon nanotubes, carbon fibers, and graphene [40, 191-193], and mainly focused on supercapacitors [189, 192, 194, 195]. So far, efforts have not yet been made to employ surface modified bio-waste derived AC for applications in any type of redox flow batteries.

In this work, high surface area ACs were synthesized from bio-waste orange peel. For pores formation, KOH was used as an activating agent. Furthermore, surface modification of one of the as-prepared ACs was done via simple acid treatment. The as-synthesized ACs and the surface modified AC were subjected to detail characterization for the composition, structure and electrochemical properties by various analyzes. *For the first time, performance of the orange peel derived AC modified bipolar plate electrodes and the effect of surface modified orange peel derived AC as electrode were evaluated for VRB applications.*

5.2 Experimental

5.2.1 Precursor material

The orange peels were collected from oranges purchased in a local supermarket, Singapore. Yellow colored fine orange peel powder (OP) was obtained following the procedure described in Section 3.1, Chapter 3. The sample powder was collected in clean dry bottles, and stored in desiccators until used.

5.2.2 Synthesis of porous activated carbon

High surface area ACs were synthesized from OP. The OP was charred to yield OP derived char (OPC), and porous ACs were synthesized impregnating OPC with KOH (OPC:KOH = 1:2 and OPC:KOH = 1:1.5) following the procedures described in Section 3.6, Chapter 3. The resultant products were designated as OP-AC for OPC:KOH = 1:2 and OP-AC1 for OPC:KOH = 1:1.5, and stored in desiccators for further studies.

5.2.3 Surface Modification of the as-synthesized AC

Surface modification of OP-AC1 was performed employing the chemical oxidizing agent, 65 wt% HNO_3 solution. Briefly, the mixtures of various mass ratios of AC and acid were shaken under constant rate of 130 oscillations per minute for 4 h at 65 °C. After cooling to room temperature, they were thoroughly washed with Milli-Q water until pH of the filtrate reached neutral, and then vacuum-filtered through 0.2 μm Millipore polycarbonate membrane. The acid treated resultant products were vacuum dried at 80 °C overnight.

FT-IR spectra of five ACs treated at different mass ratios of acids as described above are illustrated in Figure 5.1. The nomenclature indicates sample:acid ratio and the duration of treatment, for example, T-1-4 refers to acid treated AC with AC:65 wt% HNO_3 = 1:1 and kept at 65 °C for 4 h (shaken at constant rate of 130 oscillations per minute). It can be clearly seen that amongst acid treated five ACs, the peaks for T-1-4 are prominently increased compared to others. Thus, the optimal mass ratio for surface modification in this study is determined to be OP-AC1:65 wt% HNO_3 = 1:1 based on the FT-IR analysis results. The surface modified OP-AC1 is denoted as T-OP-AC hereafter.

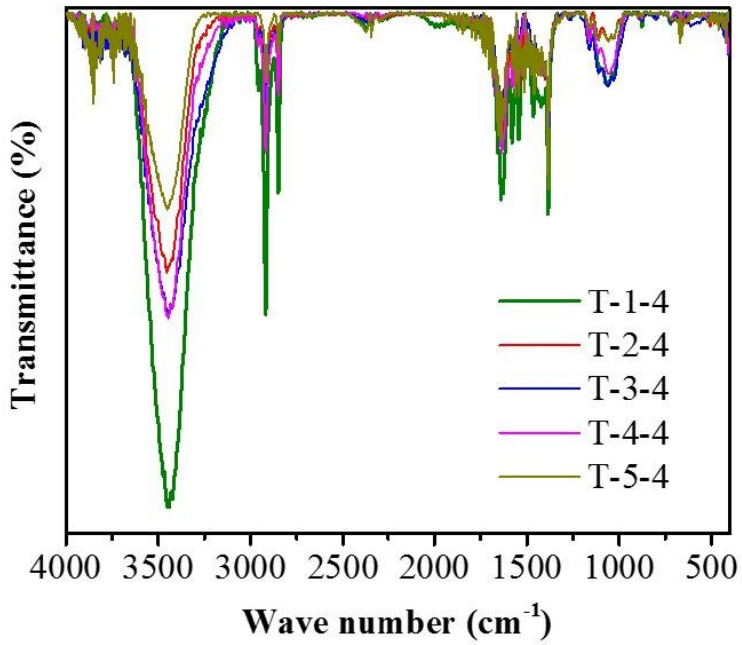

Figure 5.1. FT-IR spectra after acid treatment at different mass ratios.

5.2.4 Material characterization

Characterization of the samples was carried out for the elemental contents, physical, textural, morphological and structural properties, and surface chemistry. The tests performed were elemental analysis, proximate analysis, thermogravimetric analysis (TGA), Nitrogen sorption studies, field emission-scanning electron microscopy (FE-SEM) equipped with electron disruptive X-ray spectroscope (EDX), Transmission electron microscopy (TEM), X-ray diffraction (XRD), Confocal Raman Spectroscopy (WITec, Witec alpha300 SR), Fourier transformer infrared (FT-IR) spectroscopy and X-ray photoelectron spectroscopy (XPS) following the procedures described in relevant sections in Chapter 3. The surface areas were obtained from the BET method with the adsorption in the relative pressure (P/P_o) of 0.10. The total pore volume (V_T) was derived from the amount of nitrogen adsorbed at a relative pressure of 0.95. The micropore volume (V_{micro}) and micropore surface area (S_{micro}) were obtained from t-plot method with a relative pressure of 0.15-0.5. The PSD was measured from the desorption points using DFT pore size distribution.

5.2.5 Electrochemical measurements

5.2.5.1 Electrodes preparation

Firstly, OP-AC (90 wt%) and polyvinylidene fluoride (PVDF) as binder (10 wt%) were thoroughly mixed and homogenous slurry was made by dispersing the mixture in measured amount of N-Methyl-2-pyrrolidone (NMP) solution. For electrochemical measurements, the modified electrodes were prepared with a coat of slurry onto one surface of bipolar plates. The electrodes with coat areas of 4.0 cm^2 (2.0 cm x 2.0 cm) was used for a VRB static cell testing, and with 1 cm^2 (1 cm x 1 cm) was used for cyclic voltammetry (CV) and Electrochemical Impedance spectroscopy (EIS) studies. In both cases, the coated amount of slurry onto bipolar plate surface was 30 µL cm^{-2}. The slurry loaded plates were dried in an oven at 60 °C for overnight.

Similarly, the modified graphite plate electrodes of OP-AC1 and T-OP-AC were prepared for CV and EIS measurements. The electrodes preparation process

was same as described above for OP-AC with a slurry coating onto one surface of graphite plates of length 1 cm and width 1 cm. Results from this testing are aimed for studying the effectiveness of acid treatment of the as-synthesized AC as electrode for VRB applications.

5.2.5.2 Cell assembly

In the assembly, PAN based carbon felt and bipolar plate were used. The OP-AC coating had a thickness of ~0.3 mm. The thickness of the carbon felt (4.6 mm) reduced to ~3.0 mm after compression. Therefore, the OP-AC coating layer was about 10% of the total thickness. The OP-AC coated bipolar plate was in contact with the porous graphite felt and the other side of the plate was in contact with the copper plate, similar to a conventional VRB configuration. An anion exchange membrane (FAP-450) was used to separate the two half-cells. In the assembly, a stainless steel plate was kept at the end of both half-cells for tightening. The electrolyte concentration was 1.6 M $V^{3.5+}$ in 4.5 M total sulphate. For all tests, identical bipolar plates, felts, electrolytes and membrane were used, so the effect of coating on both half-cells was supposed to be equal. The arrangement of the cell components in a half-cell is shown in Figure 5.2.

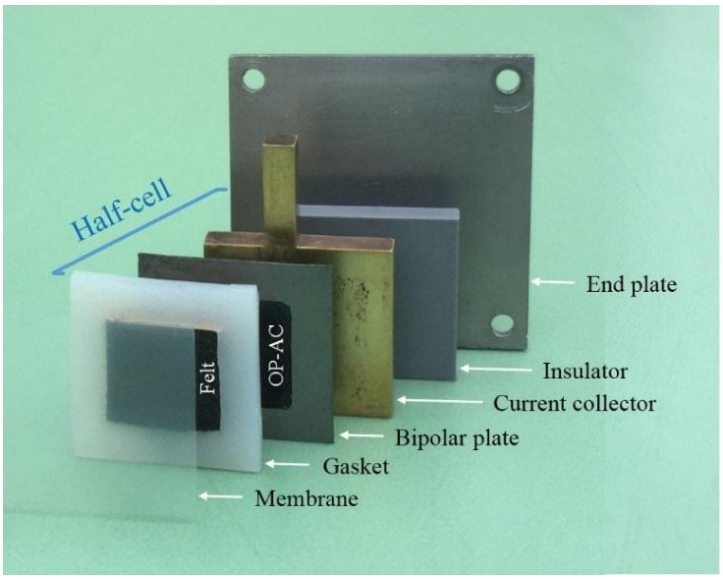

Figure 5.2. A half-cell arrangement of components used in static cell test.

5.2.5.3 Electrochemical measurements

The electrochemical performances of OP-AC, OP-AC1 and T-OP-AC were assessed by CV along with EIS using a multi-channel potentiostat (VMP3, Bio-Logic Science Instruments, France). The measurements were performed in an electrochemical cell using the bipolar plate electrode (both coated and non-coated), platinum wire and saturated calomel electrode (SCE) as working, counter and reference electrodes, respectively. The electrode was dipped into the electrolyte (mixture of 50% V^{3+} and 50% V^{4+}) and the non-coated side was connected to potentiostat probe to make it working electrode. CVs were obtained within the voltage window of -1.0 to 1.6 V (vs. SCE) at various scan rates. Similarly, EIS sudies were performed separately for each electrode for both redox couples at 50% state of charge (SOC) and were measured in the frequency range from 100 kHz to 100 mHz at ac signal of 10 mV.

The performance of OP-AC coated bipolar plate was further evaluated in a VRB static cell described in Section 5.2.5.2 using 1.6 M $V^{3.5+}$ in 4.5 M total sulphate as electrolyte at room temperature with a Battery Testing System (NEWARE, China). The charge-discharge cycles were carried out at different current densities of 5, 10, 15 and 20 mA cm^{-2} (5 cycles for each current density) with cut-off voltage between 1.6 and 0.9 V. The coulombic, energy and voltage efficiencies of the cell were calculated from the charge-discharge profiles.

5.3 Results and Discussion

5.3.1 Elemental composition

The major constituents of OP have been reported to be protein, pectin, cellulose, and pigments [159]. Table 5.1 presents the elemental composition of OP, OP-AC and OP-AC1 from this study, and values reported in some previous studies. The carbon content measured for the precursor (OP) in this study is slightly low (40.9%) compared with reported values of 43.0% [146] and 44.1% [149]. The difference in the observed values may be due to the orange types. The C content is doubled in the OP-AC (82.8%) as compared with the precursor value (40.9%), and is comparable

with the previously reported value of 82.5% [146].The C content is higher in OP-AC (82.8%) than OP-AC1 (62.0%).

Table 5.1. Elemental composition of OP and ACs (wt%).

Sample	C%	H%	N%	S%	O%[a]	Reference
OP	43.0	5.9	0.9	0.0	50.2	[146]
OP-AC	82.5	2.5	0.9	0.0	14.1	[146]
OP	44.1	5.8	0.8	-	49.3	[149]
OP	40.9	6.1	0.8	0.2	52.0	This study
OP-AC	82.8	1.3	0.5	0.2	15.2	This study
OP-AC1	62.0	3.9	0.2	0.2	33.7	This study
T-OP-AC	57.6	3.7	0.4	0.1	38.2	This study

[a]Estimated by difference

5.3.2 Proximate results

The proximate analysis of OP showed the moisture content of 7.85%, volatile matter (VM) of 87.66%, ash of 4.49% and fixed carbon (FC) of 7.85%. The high VM and low ash contents of OP suggest that the precursor material as biomass is suitable for its conversion into AC.

5.3.3 Thermogravimetric analysis (TGA)

KOH increased thermal stability of the OPC and KOH mixture. TGA illustrates combustion behavior, which provides useful information for further thermal experiments. The weight loss (TG) curves of OP and OPC impregnated with KOH are shown in Figure 5.3. The profile of OP exhibited a little weight loss from 50 to 128 °C which could be attributed to moisture release. A significant mass loss is observed from 128 to 357 °C (~60% by weight) due to the release of volatiles, and the minimal weight loss occurred at temperatures above 560 °C. TGA profile of

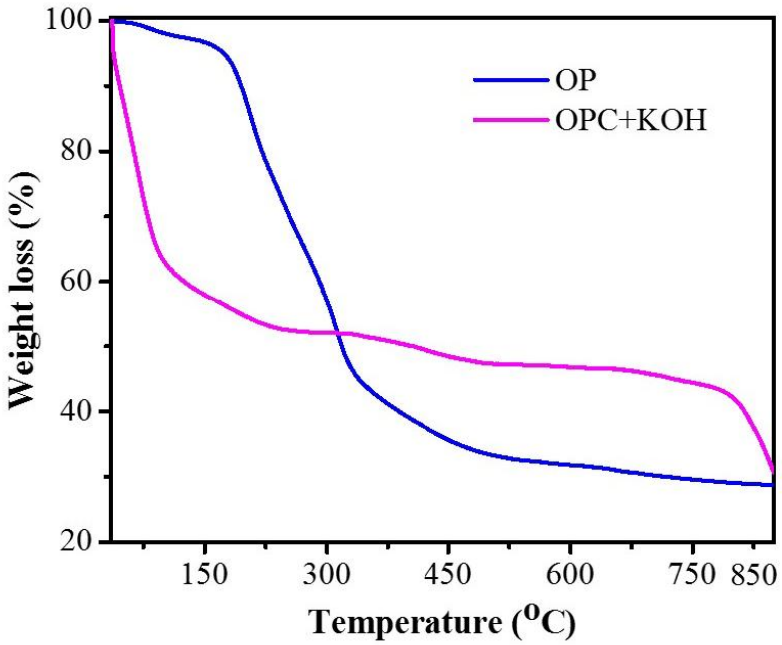

Figure 5.3. TGA curves: OP (a), and OPC impregnated with KOH (b).

OPC impregnated with KOH shows a significant weight loss between 50 to 271 °C (27.6% by weight), which is attributed to moisture loss. This sample constitutes KOH (melting point = 360 °C) mixed with OPC in weight ratio of 2:1 (KOH:OPC). There is a gradual weight loss from 271 to 335 °C, and minimal weight loss is observed at temperatures above 335 to 800 °C. The overall weight loss of OP (79.9%) is more than two-fold of OPC impregnated with KOH (35.6%), which is expected since OPC is charred product of OP.

5.3.4 Functionalized AC

TGA of the as-synthesized OP-AC1 and T-OP-AC was also carried out in order to corroborate the surface modification. TGA curves in Figure 5.4a illustrate the weight loss for OP-AC1 and T-OP-AC. The weight loss up to 150 °C is negligible for both samples, which is due to the pre-dried samples. However, it can be clearly seen that the weight loss (Δm) after that is faster for T-OP-AC than OP-AC1. The speedy mass loss of T-OP-AC is due to the defective carbon or presence of carbon associated functional groups which are easily decomposed. This is indication of the

successful surface modification of OP-AC1. The lower residual content in T-OP-AC (29.0%) than OP-AC1 (32.5%) implies that possibly some inorganics present hydroxyl, quinine, and lactone groups [13]. The increase in stretching vibrations and boosted peaks in the spectrum of T-OP-AC indicates that the

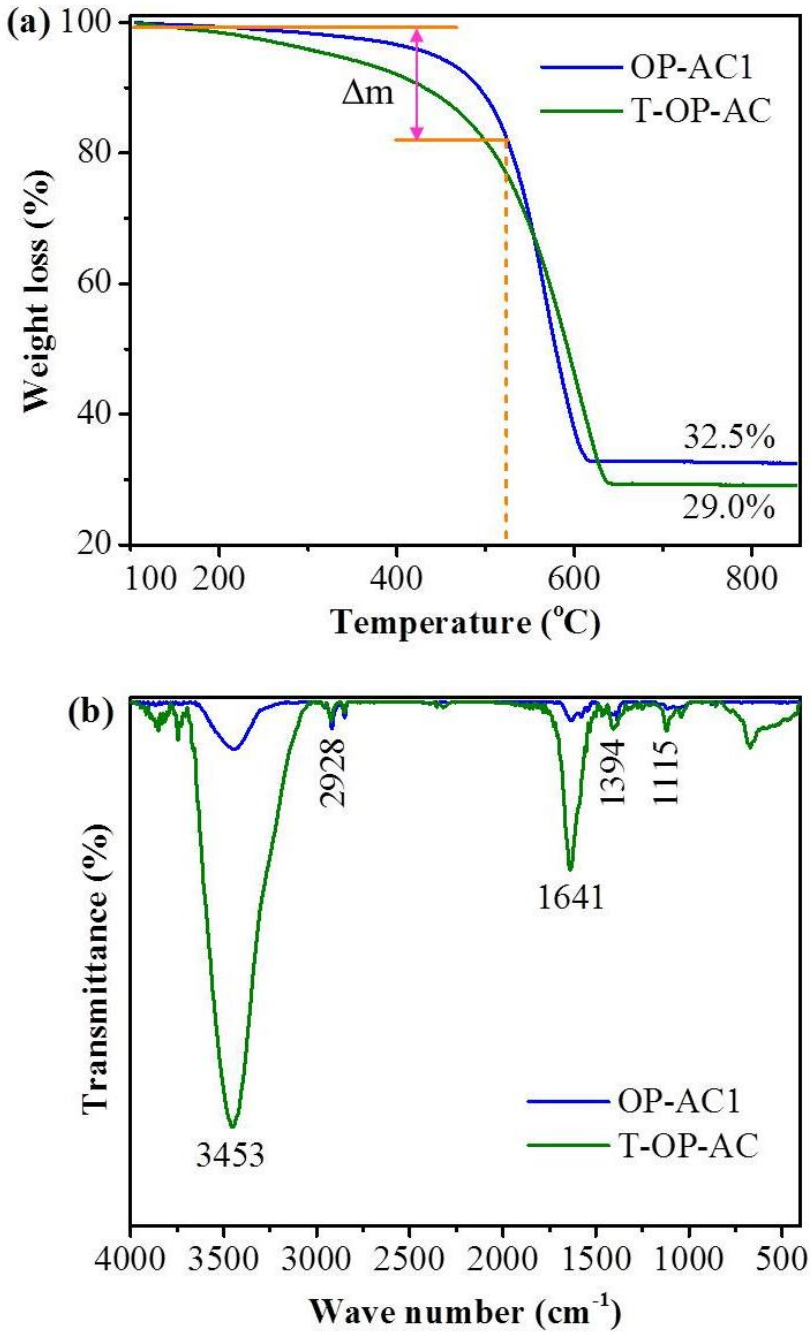

Figure 5.4. TGA curves (a), and FT-IR spectra (b) of OP-AC1 and T-OP-AC under constant air flow.

treatment developed functional groups on the sample surfaces. Some oxygen functional groups, such as hydroxyl, carboxyl, carbonyl and quinone provide positive effects on the performance of AC based electrodes [82, 195]. The observed FT-IR results for T-OP-AC confirm the successful surface modification of OP-AC1.

5.3.5 Textural properties

Nitrogen adsorption-desorption studies of OP-AC depict a combination of both type I and IV isotherms (Figure 5.5a) [196]. The Nitrogen adsorption at very low relative pressure reflects the predominance of micropores, and a tiny hysteresis loop indicates the existence of some mesopores. The BET surface area, micropore surface area and mesopore surface area are calculated to be 1901, 1407 and 494 m^2 g^{-1}, respectively. The total pore volume is 0.94 cc g^{-1} with micropore volume of 0.59 cc g^{-1}. It is observed that the pore size of the pores varied widely, however, majority of the pores have 11.26 Å pore width. The inset in Figure 5.5a shows pore size distribution (PSD) of the pores in OP-AC.

Figure 5.5b presents the comparative Nitrogen adsorption-desorption isotherms of OP-AC1 and T-OP-AC, which indicate similar textural properties as that for OP-AC. Both samples have pore structure of a combination of micropore and mesopore with the predominance of micropores. This is also supported by the relatively narrow PSD with pore width of 11.75 Å for the majority of pores as illustrated in Figure 5.5c. Pore characteristics of OP-AC1 before and after acid treatment are summarized in Table 5.2. The BET surface area decreased from 1916 m^2 g^{-1} to 1405 m^2 g^{-1} after the acid treatment. The pore volumes also reduced for T-OP-AC, however, pore width for majority of pores remained nearly the same. These changes in pore characteristic are likely due to the etching effect of the acid. The etching effect may have caused removal of some carbon networks inside the OP-AC1 particles leading to larger pores that changed pore characteristic, but maintaining pore width of most pores almost the same. Previous studies have also reported changes in pore characteristic with reduced surface areas and pore volumes after surface functionalization of ACs [13, 191].

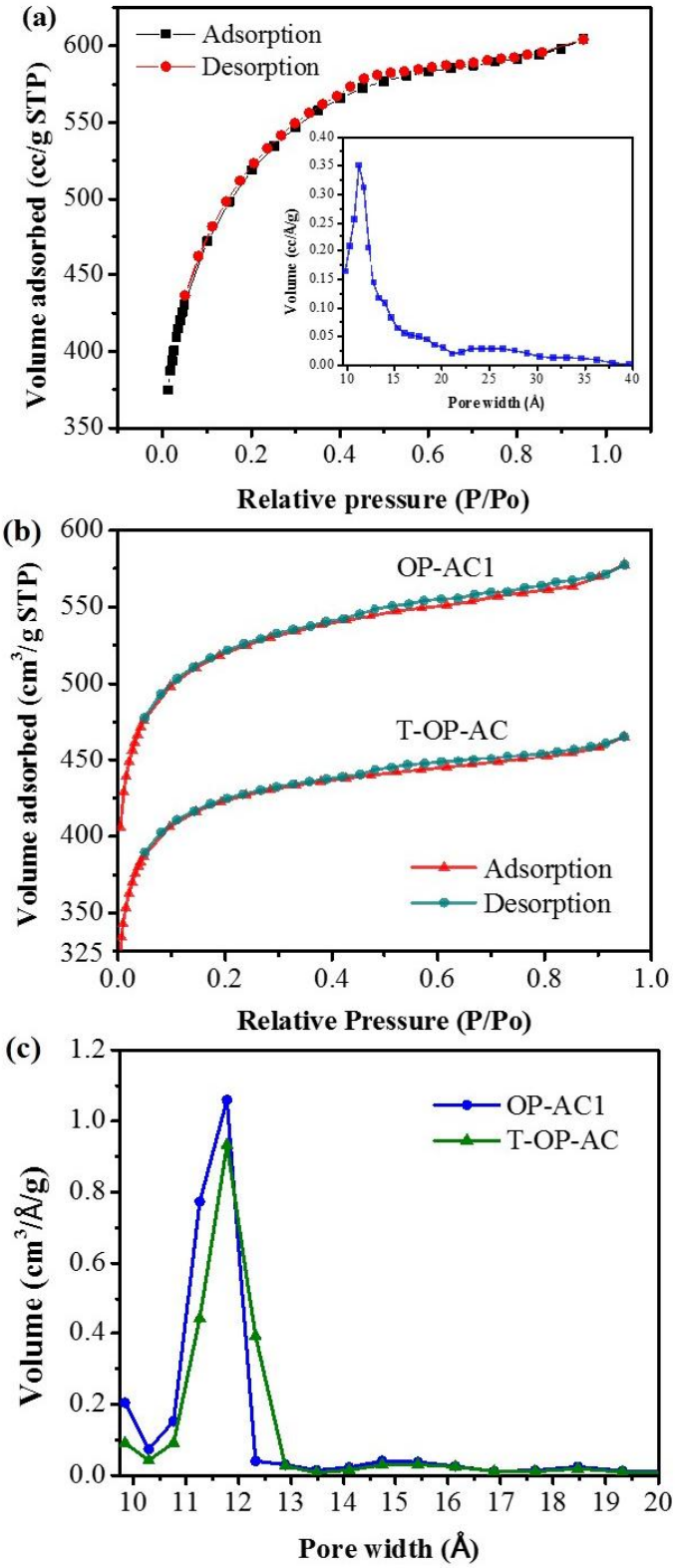

Figure 5.5. Nitrogen adsorption-desorption isotherm and pore size distribution (inset) of OP-AC (a), Nitrogen adsorption-desorption isotherms of OP-AC1 and T-OP-AC (b), and pore size distribution of OP-AC1 and T-OP-AC (c).

Table 5.2. Pore characteristic of OP-AC1 before and after acid treatment.

Sample	S_{BET} [a)] ($m^2\ g^{-1}$)	S_{micro} [b)] ($m^2\ g^{-1}$)	V_T [c)] ($cm^3\ g^{-1}$)	V_{micro} [d)] ($cm^3\ g^{-1}$)	$V_{micro}\ /\ V_T$ (%)	Pore width [e)] (Å)
OP-AC1	1916	1715	0.90	0.72	80.00	11.78
T-OP-AC	1405	1283	0.72	0.61	84.72	11.78

[a)] BET (Brunauere-Emmette-Teller) surface area.
[b)] Micropore surface area.
[c)] Total pore volume, measured at $P/P_0 = 0.95$.
[d)] Micropore volume, derived from DFT model.
[e)] Pore width of most pores (mode).

5.3.6 Morphological properties

Figure 5.6a and b illustrate FE-SEM image of OP-AC with well-developed pores and porous network like structure. The obtained different values of typical pore width in two tests are due to the pores with a width of 11.26 Å that are invisible in Figure 5.6a and b, however, their quantity is significantly more than the quantity of pores with a width of 1 μm. The EDX mapping indicates the major constituents in the OP-AC are carbon and oxygen elements (Figure 5.6c and d). Further, porous nature of the synthesized AC is evident from the nanostructure of the pores obtained from TEM examination shown in Figure 5.6e.

In the process of pyrolysis during AC preparation, some large pores might have formed due to the enlargement of small pores with more gasification during the activation process as described in Section 4.4, Chapter 4. The creation of interconnected pores with high surface area is attributed to intercalation of K^+ ions into the lamellae of the crystallites during activation. The porous network allows fast ion diffusion and the high surface area makes available of more active sites for the electrical double layer formation across the electrode/electrolyte interface.

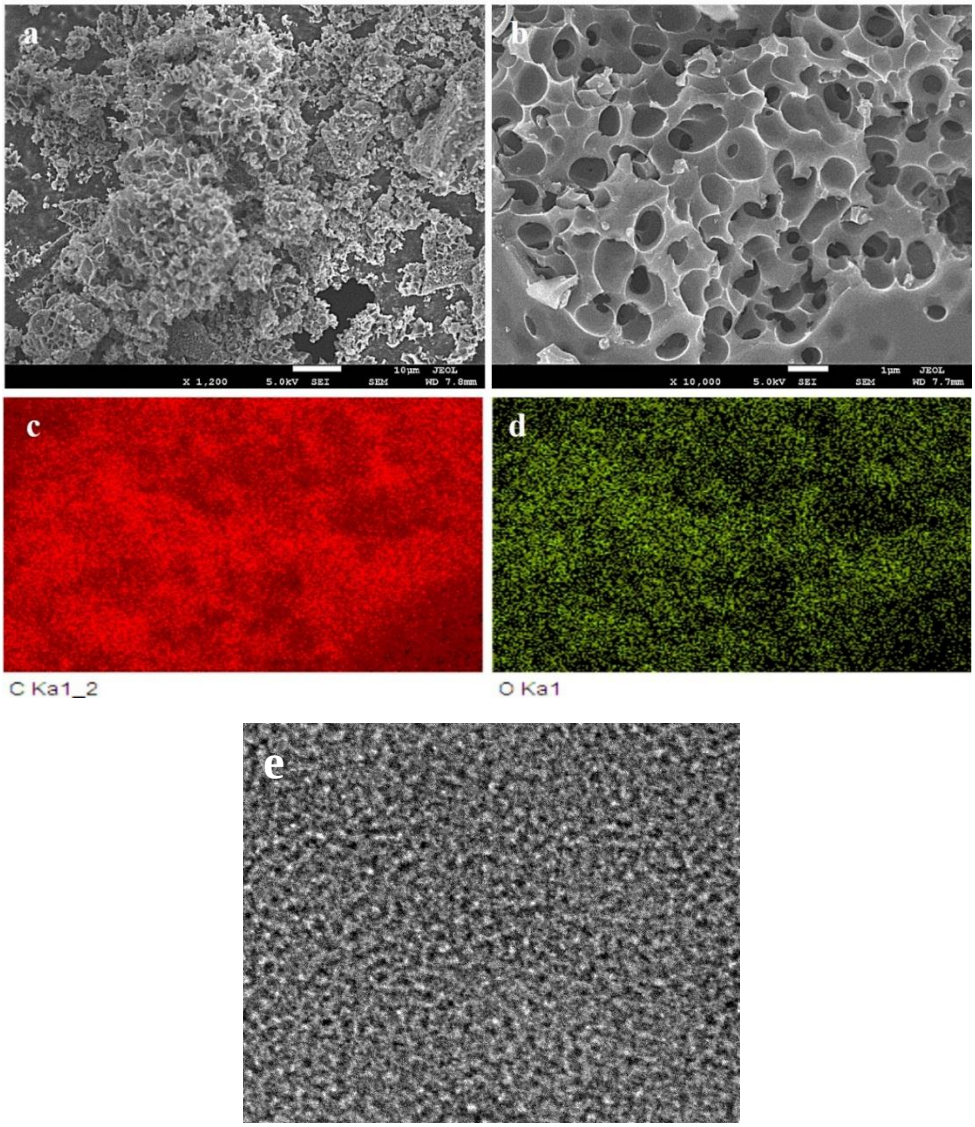

Figure 5.6. FE-SEM images at low and high magnifications (a and b), EDX mappings of carbon and oxygen (c and d) and TEM image of OP-AC (e).

Similarly, FE-SEM images of OP-AC1 before and after surface modification are illustrated in Figure 5.7a and b, respectively. Both samples depict similar surface morphologies, however, the surfaces of the acid treated sample are cleaner than the untreated sample. The interconnected porous network allows rapid ion diffusion, and the high surface area provides more sites for electrolyte across the electrode/electrolyte interface. Furthermore, the nanoporous structure of the samples without any distinct observable difference is clearly evident from the TEM images (Figure 5.7c and d). EDX analysis results of the samples are presented in

Figure 5.8. It can be seen that OP-AC1 mainly contains C and O elements though trace amount of noises observed (Figure 5.8a, c and e). The contents in T-OP-AC are also C and O elements but noises are not present (Figure 5.8b, d and f). This implies that the HNO_3 treatment aimed to modify surface chemistry of AC sample also purifies the sample surface by removing contaminants that may hinder charger transfer.

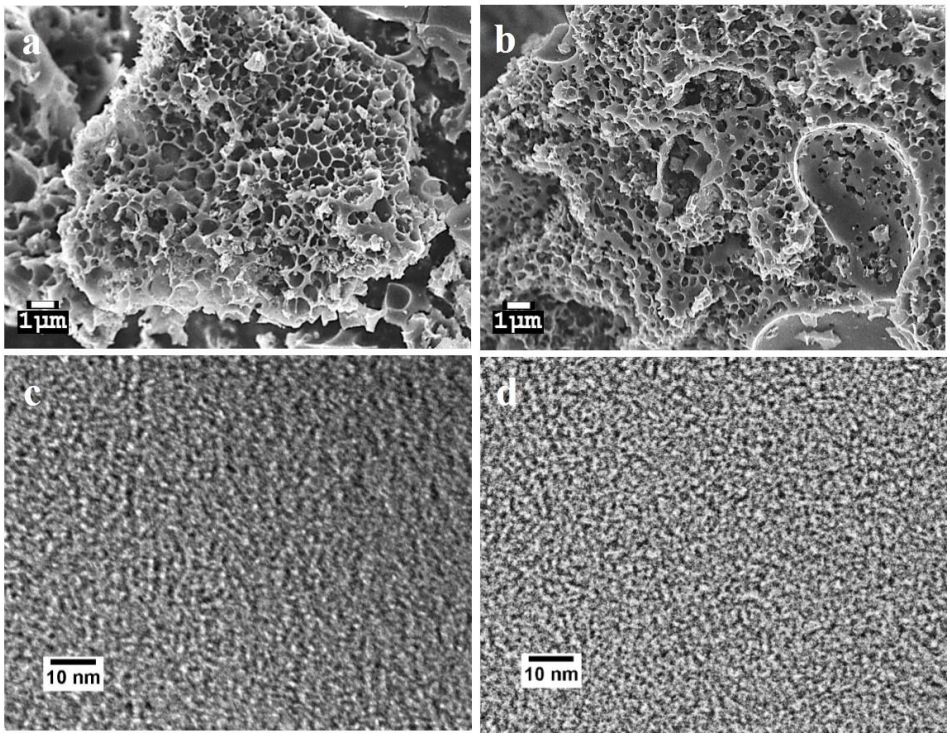

Figure 5.7. FE-SEM images and TEM images of OP-AC1 (a and c), and T-OP-AC (b and d).

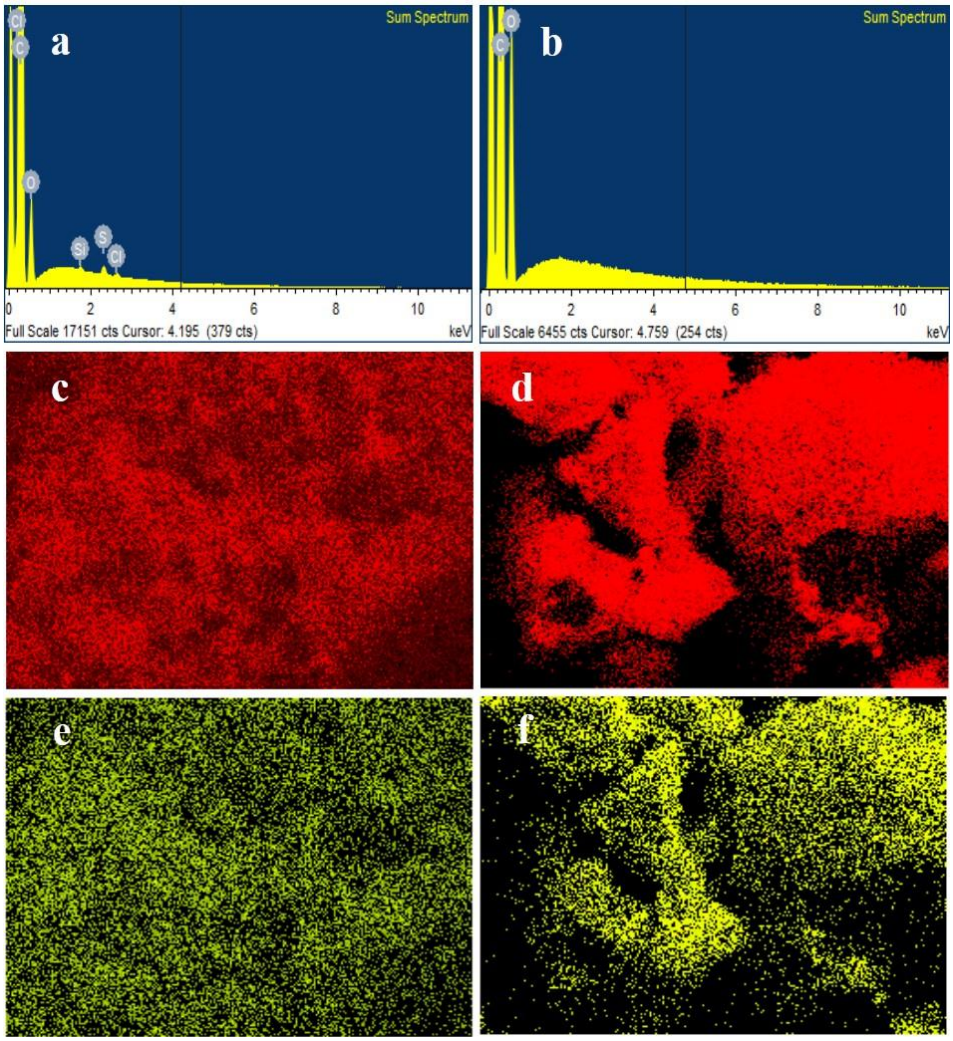

Figure 5.8. EDX spectrum of elements and mapping of C and O of OP-AC1 (a, c and e) and T-OP-AC (b, d and f).

5.3.7 Structural and surface properties

Figure 5.9a presents the diffraction patterns of OP-AC obtained from crystallographic study by XRD. There are two broad peaks around 2θ values of 29.5° and 43.0°, which match to the (002) and (110) planes of the graphite structure in the carbon based materials, respectively. The observed peaks refer to amorphous semi-graphitic carbon [95, 166]. Raman spectroscopy is considered as a non-destructive technique commonly used to elucidate ordered, defective or disordered crystal structures of carbon. Figure 5.9b displays Raman spectrum of OP-AC; there are two main peaks that correspond to different features of carbon materials. The

D band (at ~1371 cm^{-1}) is attributed to the disorder or defect intervened zone-edge (near K-point) phonons. The G band (at ~1604 cm^{-1}) is associated to the in-plane vibration of sp^2 atoms present in carbon materials. The ratio between the intensities of the D and G bands (I_D/I_G) is used to predict the presence of defects within the samples. The I_D/I_G ratio is calculated to be 0.99, indicating the existence of substantial amounts of defects and disordered structures in the sample [11, 197].

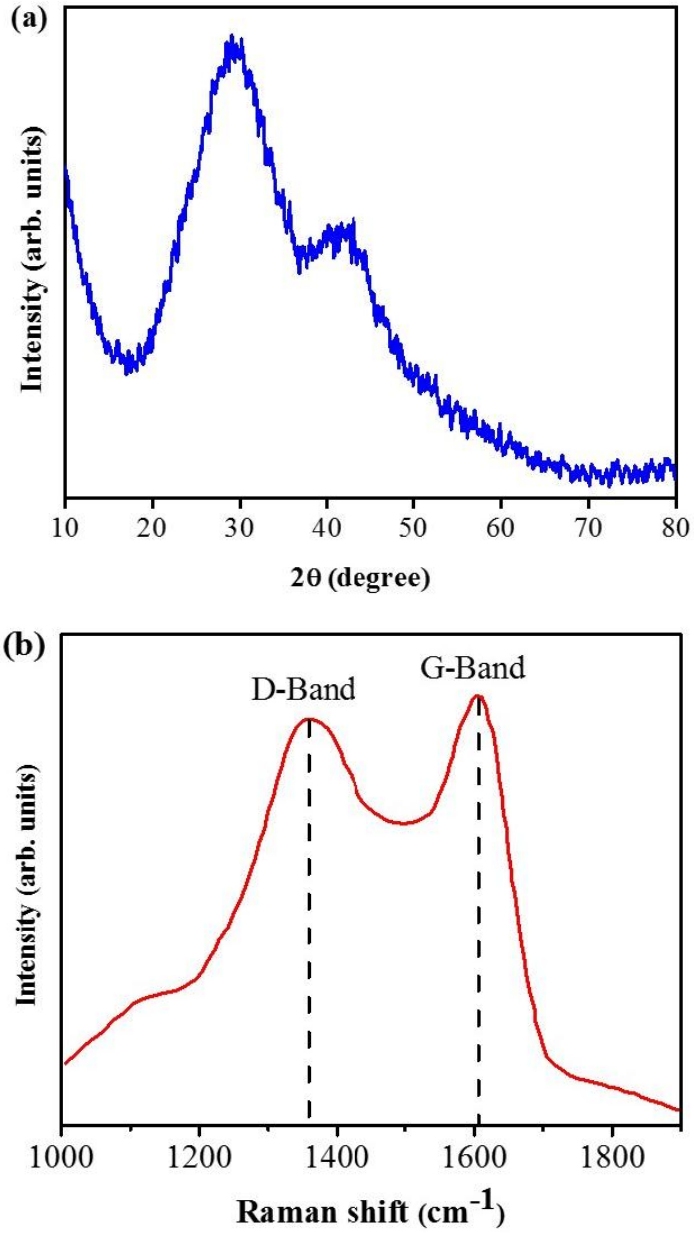

Figure 5.9. XRD spectra (a), and Raman spectra (b) of OP-AC.

Similarly, crystallographic information of OP-AC1 and T-OP-AC was obtained. Figure 5.10a illustrates the diffraction patterns of OP-AC1 and T-OP-AC. It can be seen that there are two broad peaks with low intensities around 2θ values of 22.2° and 43.1° for OP-AC1, and similar peaks present around 2θ values of 23.0° and 43.1° for T-OP-AC. The observed peaks in both samples match to the (002) and (110) planes of the graphite structure in the carbon based materials, which indicate amorphous natured semi-graphitic carbons [166].

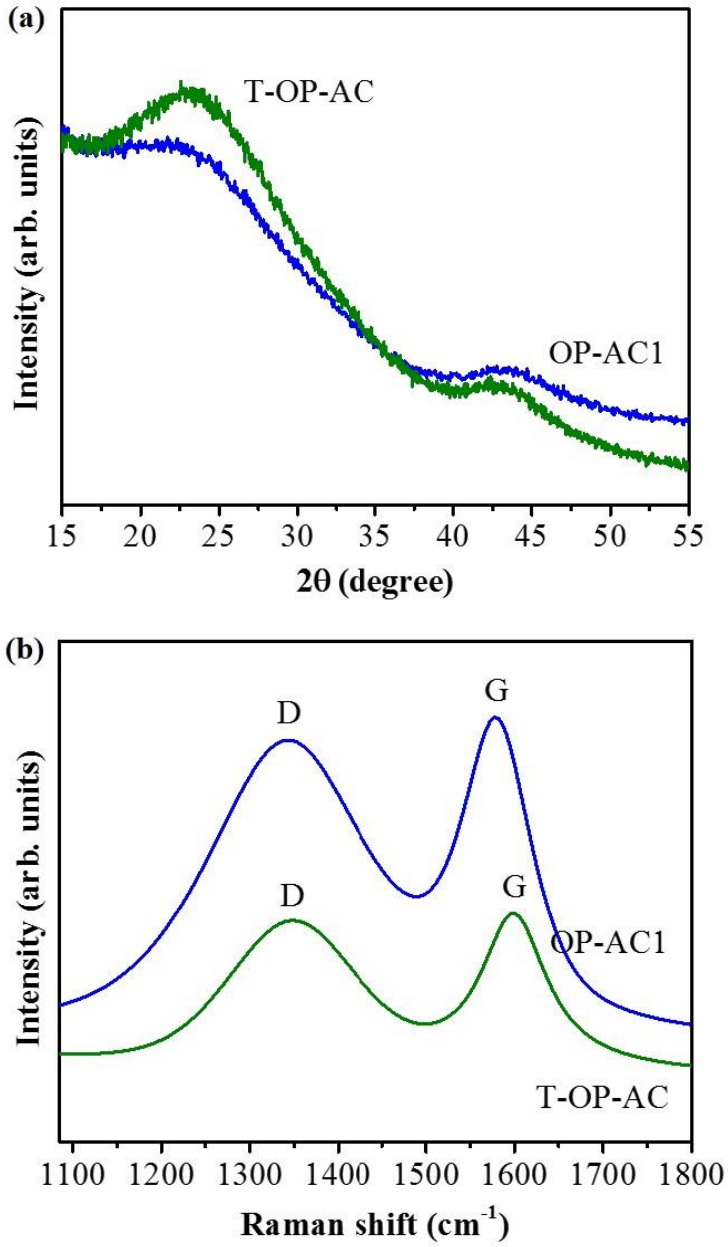

Figure 5.10. XRD spectra (a), and Raman spectra (b) of OP-AC1 and T-OP-AC.

In addition, Raman spectra of OP-AC1 and T-OP-AC in Figure 5.10b display two major peaks that correspond to different features of carbon materials. As mentioned earlier, the D band reflects disorder or defect intervened zone-edge (near K-point) phonons, whilst the G band is associated to the in-plane vibration of sp^2 atoms present in carbon materials [198]. The D band and G band for OP-AC1 are at ~1343 cm^{-1} and ~1580 cm^{-1}, respectively, and their positions for T-OP-AC are at ~1347 cm^{-1} and ~1599 cm^{-1}, respectively. The I_D/I_G ratios for OP-AC1 and T-OP-AC are calculated to be 0.85 and 0.84, respectively, which infers predominant sp^2 type carbon in the samples [11, 197].

The functional groups on the surface of OP-AC were also studied by XPS analysis. The wide survey spectra of OP-AC are illustrated in Figure 5.11a, which reveals the existence of carbon and oxygen. Figure 5.11b shows the existence of different functionalities on the sample along with the corresponding high resolution de-convoluted C 1s band spectra. The C1s spectra of the samples are fitted by five individual component peaks. The peaks at 284.5 and 285.4 eV are assigned to sp^2 C=C and sp^3 C–C, while the peaks at 286.7, 288.6 and 291.4 eV correspond to C–O, C=O and π-π*, respectively [168]. The sp^2 configuration forms π-π* bands, whereas sp^3 creates σ-σ* spectra from the localized density of states formation. The percentage of sp^2 C=C and sp^3 C–C are calculated to be 58.0% and 18.9%, followed by 11.6%, 11.1% and 0.5% for C=O, C–O and π-π* groups, respectively. The results show the presence of a large number of oxygen containing functional groups (C=O and C-O) on the surface of OP-AC, which are beneficial for better electrochemical processes.

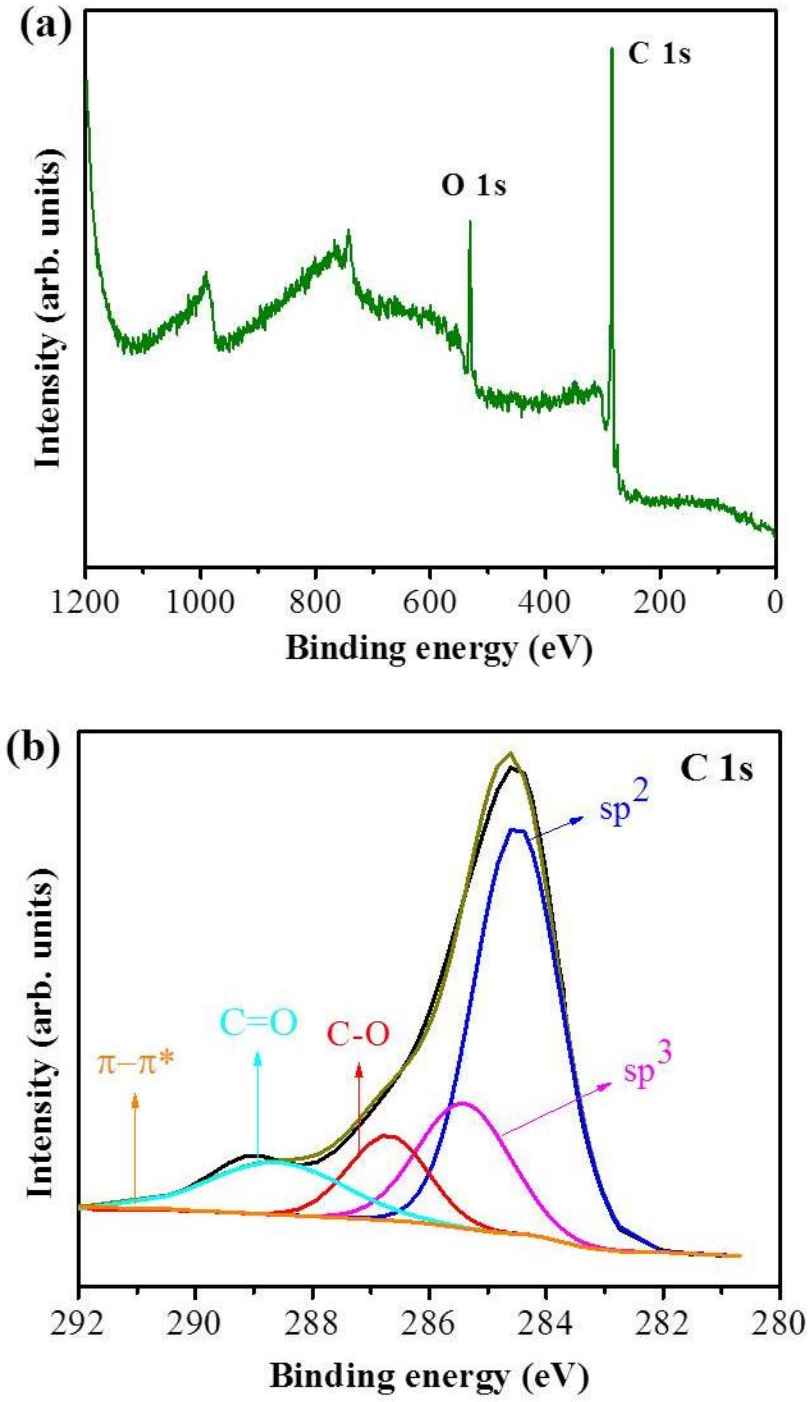

Figure 5.11. XPS survey spectra (a), and C 1s spectra (b) of OP-AC.

Similarly, surface features of OP-AC1 before and after surface modification were further explored by XPS analysis. Figure 5.12a and b illustrate wide survey spectra of OP-AC1 and T-OP-AC in the binding energy range of 0-1200 eV. However, this study focuses on peaks related to C 1s and O 1s spectra. Table 5.3

shows increase of O content from 11.4 atomic% in OP-AC1 to 16.4 atomic% in T-OP-AC. The higher O/C ratio (0.20) in surface modified sample compared with untreated one (0.13) clearly indicates the enrichment of oxygen functional groups after acid treatment. The well resolved peaks in the core-level high resolution de-convoluted C 1s spectra are shown in Figure 5.12c and d. The peaks positioned at binding energies of 284.4, 285.2. 286.2, 287.6 and 288.7 eV are assigned to sp^2 C=C, sp^3 C-C, C-O, C=O and O-C=O, respectively [40]. Table 5.4 presents the respective percentage of the surface functional groups. It was observed that total fraction of oxygenated carbon is higher for the surface modified AC (35.6%) than the as-prepared AC (28.1%), suggesting enrichment of oxygen functionalities from acid treatment. The concentrations of C-O and C=O groups in T-OP-AC are more than double compared to OP-AC, which are beneficial for the vanadium species

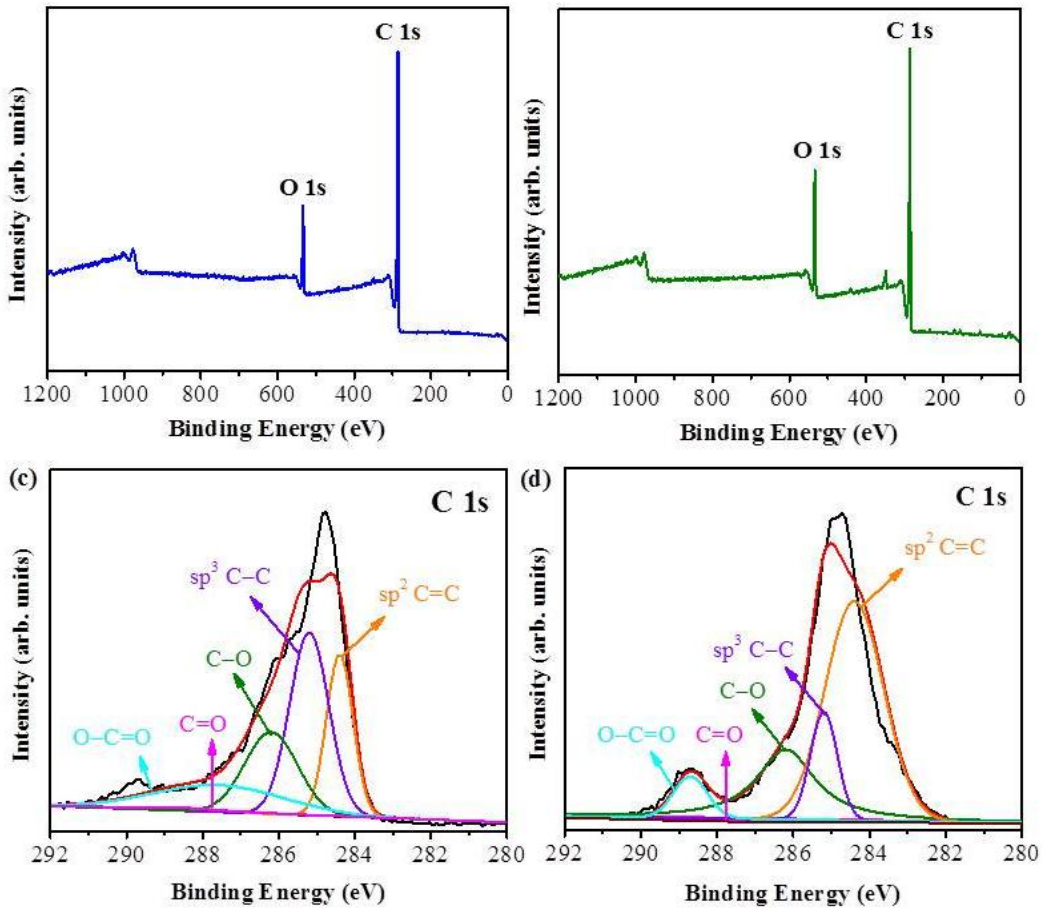

Figure 5.12. XPS survey spectra and the core-level C 1s spectra of OP-AC1 (a and c), and T-OP-AC (b and d).

reactions in VRB. A previous study on functionalized carbon nanotubes had reported that the presence of large concentration of oxygen-containing functional groups on the surface of the electrode material facilitate charge transfer processes by generating more active sites for the reactions [199].

Table 5.3. The elemental quantification of the XPS measured OP-AC1 before and after acid treatment.

Sample	Elemental concentration (atomic %)		
	C	O	O/C ratio
OP-AC1	88.6	11.4	0.13
T-OP-AC	83.6	16.4	0.20

Table 5.4. Surface functional groups (%) obtained from curve fitting of C 1s XPS spectra.

Sample	C=C (sp^2) 284.4 eV	C–C (sp^3) 285.2 eV	C–O 286.2 eV	C=O 287.6 eV	O–C=O 288.7 eV
OP-AC1	49.4	22.6	11.6	1.8	14.7
T-OP-AC	52.5	11.9	24.6	5.3	5.7

5.3.8 Electrochemical behavior

Figure 5.13 depicts CV curves of both pristine and OP-AC coated bipolar plate electrodes in 1.6 M $V^{3.5+}$ in 4.5 M total sulphate solution as electrolyte at a scan rate of 5 mV s^{-1}. The CV curves exhibit two redox couples V^{2+}/V^{3+} and V^{4+}/V^{5} on negative and positive sides, respectively. Higher anodic and cathodic peak currents are observed in OP-AC coated electrode than the pristine electrode, indicating higher electro-catalytic activities for both redox couples. This is likely due to the increase of surface area and the presence of oxygen-containing functional groups on the surfaces of the OP-AC. Additionally, the presence of oxygen containing

functional groups in OP-AC enhances hydrophilic properties, thus improving the wettability of the electrode in the aqueous electrolyte and faster electron transfer.

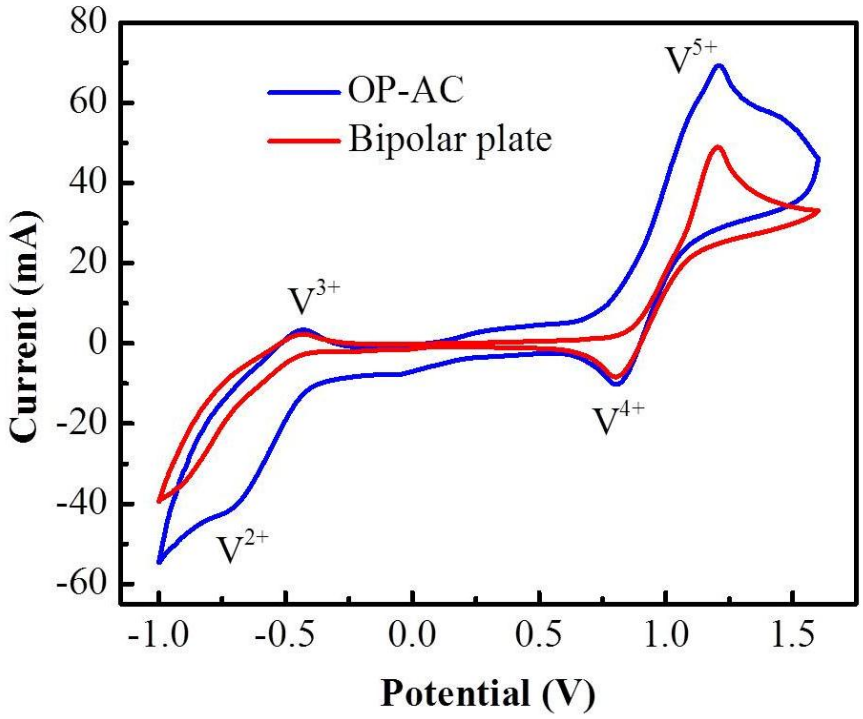

Figure 5.13. Cyclic voltammogram (CV) with or without OP-AC onto bipolar plate as working electrodes in 1.6 M $V^{3.5+}$ in 4.5 M total sulphate at a scan rate of 5 mV s^{-1}.

Similarly, Figure 5.14 illustrates the CV curves of pristine graphite, OP-AC1 and T-OP-AC electrodes in 1.6 M $V^{3.5+}$ in 4.5 M total sulphate solution as electrolyte at a scan rate of 5 mV s^{-1}. There are two redox couples V^{2+}/V^{3+} and V^{4+}/V^{5} on negative and positive sides, respectively. It is clearly shown that the anodic and cathodic peak currents for OP-AC1 and T-OP-AC electrodes are significantly higher compared with the pristine electrode. The peak currents are slightly higher for T-OP-AC than OP-AC1. More importantly, upon surface modification of OP-AC1, the peak potential separation corresponding to redox couple V^{4+}/V^{5+} is decreased by 76 mV, and a clear peak is also exhibited for V^{2+}/V^{3+} redox couple for T-OP-AC which is not present for both OP-AC1 and graphite. Higher peak currents and lower oxidation potentials contribute in

enhancing energy efficiency of the cell as it implies a lower charge voltage for the VRB. The results infer electrocatalytic activity in the order of T-OP-AC > OP-AC1 > Graphite. The better electrochemical properties of OP-AC1 than graphite is attributed to the presence of oxygen functional groups on its surface. While, the further improved electrocatalytic activity of T-OP-AC compared with OP-AC1 is due to the presence of rich concentration of oxygen functional groups as evidenced from Table 5.4. The existence of a large concentration of surface oxygen groups in T-OP-AC play role in generating more active sites, and this facilitates charge transfer reactions [190, 191, 200].

In order to gain more understanding on the electrochemical processes, EIS was performed for the fabricated electrodes. Figure 5.15 presents the EIS results for both pristine and OP-AC coated bipolar plates. The Nyquist plots comprise a semi-circle part at high frequencies that arises from the charge transfer process

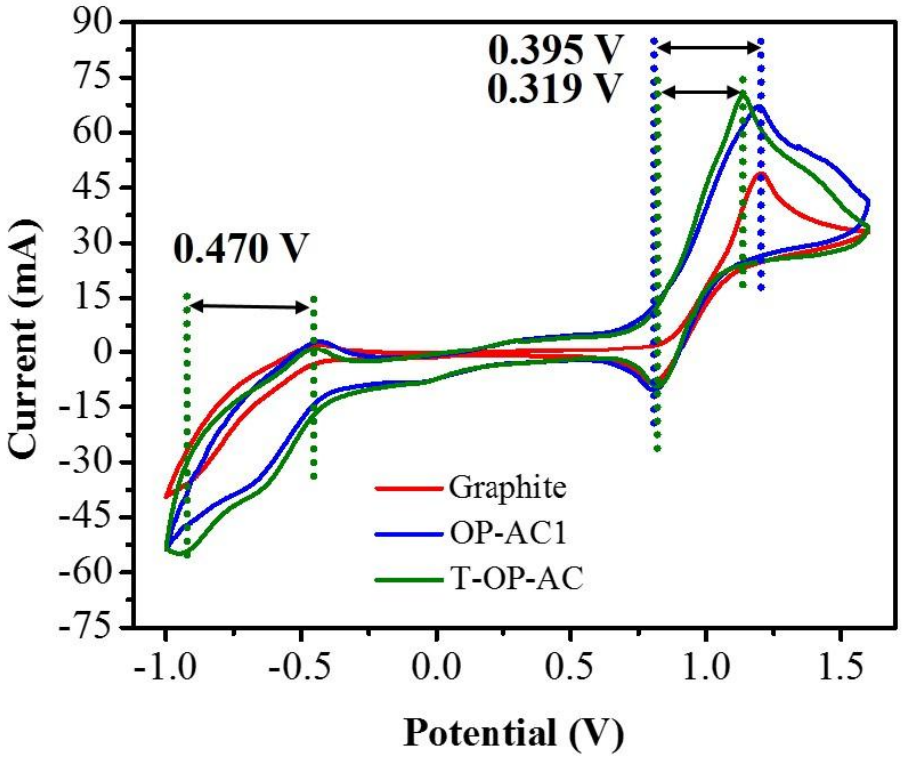

Figure 5.14. CV curves of the graphite, OP-AC1, and T-OP-AC in the electrolyte of 1.6 M $V^{3.5+}$ in 4.5 M total sulphate at a scan rate of 5 mV s^{-1}.

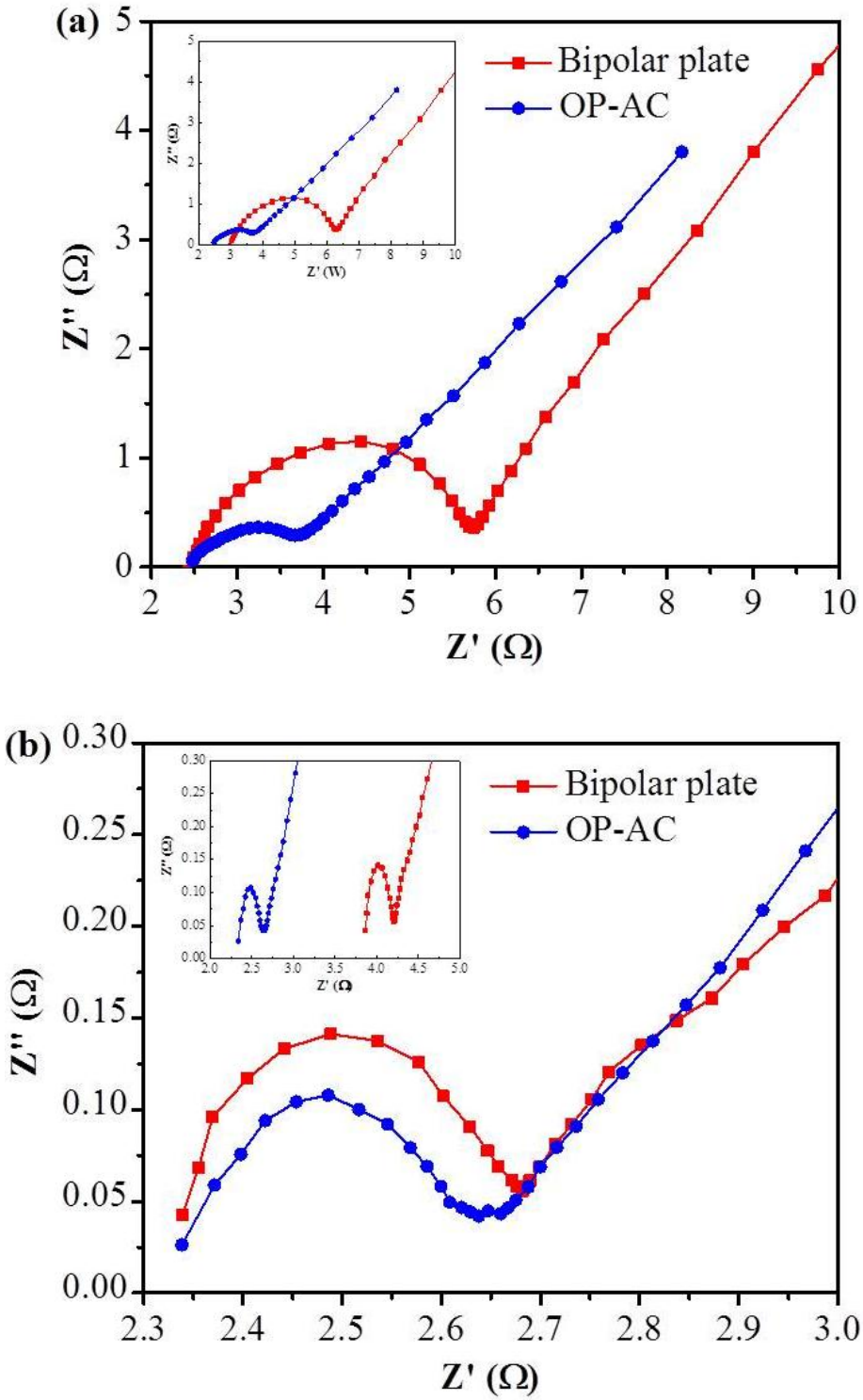

Figure 5.15. Nyquist plots of pristine and OP-AC coated bipolar plates recorded in frequency range of 100 kHz to 100 mHz at ac signal of 10 mV in in $V^{2.5+}$ solution (a), and in $V^{4.5+}$ solution (b). The inset diagram in Figure 5.16a and Figure 5.16b shows the spectra without moving the high frequency intercept.

(electrolyte/electrode interface) and a linear part in the low frequency region that relates to the diffusion of vanadium ion through pore channel of the electrode [175]. To compare the charge transfer resistance between pristine and OP-AC coated bipolar plates, the high frequency intercept are moved to the same point. The inset diagram in each figure shows the original spectra prior to moving the high frequency intercept. The high frequency for the OP-AC coated electrodes is clearly much lower than the pristine electrode, indicating contact improvement at the interface between the porous felt and bipolar plate. The impedance results show that the charge transfer resistance for the pristine electrode (3.60 Ω) is nearly two-fold compared with OP-AC coated bipolar plate (1.83 Ω) in negative (V^{2+}/V^{3+}) electrolyte (Figure 5.15a). Similarly, the charge transfer resistance are calculated to be 0.30 and 0.25 Ω in positive (V^{4+}/V^{5+}) electrolyte for pristine and OP-AC coated bipolar plates, respectively (Figure 5.15b). The lower charge transfer resistance of OP-AC improves the electrochemical reaction. Overall, CV and EIS results indicate that the improved electro-catalytic activity, and reduced charge transfer resistance of OP-AC can be ascribed to the synergistic effect of high surface area and the presence of oxygen-containing functional groups on the surface of OP-AC. The ac impedances for the pristine and OP-AC modified electrodes are fitted with the equivalent circuit given in Figure 5.16.

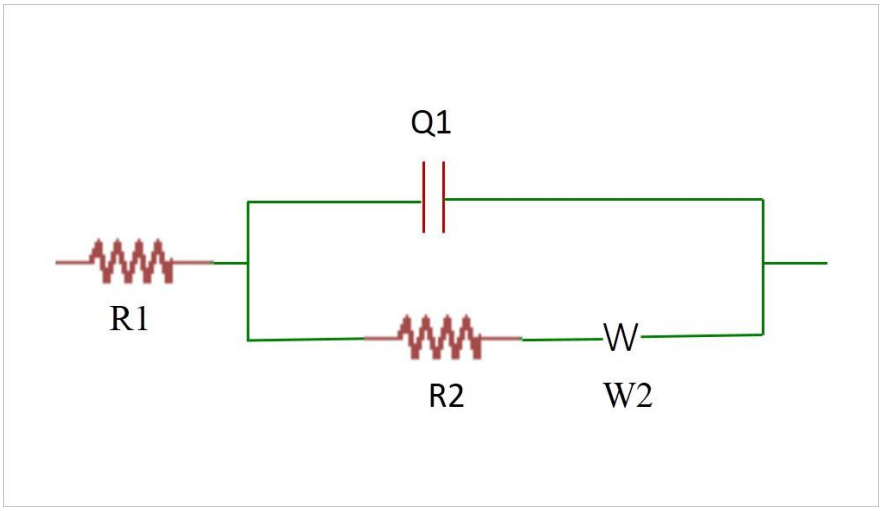

Figure 5.16. Equivalent circuit for the electrodes test in VRB.

In the given equivalent circuit above,

R1 = ohm resistance, composed of electrolyte resistance and electrode resistance,

R2 = charge transfer resistance across electrode/electrolyte interface,

Q1 = the constant-phase element which represents the electric double layer capacitance of electrode/electrolyte interface, and

W2 = the constant-phase element, which represents the diffusion capacitance attributed by the diffusion process of vanadium ions in the electrodes.

EIS studies of pristine graphite, OP-AC1 and T-OP-AC were also performed, and the results are presented in Figure 5.17. The Nyquist plots comprise a semi-circle part and a linear part, indicating the redox reactions are mix-controlled by charge transfer and diffusion. The semi-circle part at high frequencies relates to the charge transfer resistance across electrode/solution interface, and the linear part at low frequencies reflects the diffusion processes in pore channel of carbon electrode. The intercept on the X-axis refers to the ohmic impedance of the cell that arises from the resistance composed of solution resistance and electrode resistance [201]. However, in the present work, only charge transfer resistance is studied as it relates to kinetics of the electrode. The OP-AC1 and T-OP-AC are morphologically similar in terms of pores and surface structures. However, they have differences in the concentrations of surface oxygen functionalities (higher in T-OP-AC), which play crucial role in electrocatalytic activity towards the vanadium redox couples reactions. The original spectra prior to fitting the high frequency intercepts are shown in the inset diagrams (Figure 5.17a and 5.17b). The numerical fitting results on the basis of impedance measurement indicate that the charge transfer resistances are 2.941, 1.694 and 1.476 Ω, respectively, for graphite, OP-AC1 and T-OP-AC electrodes in negative (V^{2+}/V^{3+}) electrolyte (Figure 5.17a). Similarly, the charge transfer resistances are in the order of Graphite > OP-AC1 > T-OP-AC with 0.391, 0.256 and 0.223 Ω, respectively, in positive (V^{4+}/V^{5+}) electrolyte (Figure 5.17b). The lower charge transfer resistance enhances the electrochemical reaction. Previous studies have reported the catalytic role of surface oxygen groups on redox reaction kinetics thereby enhancing overall VRB performance [40, 180, 202].

Further studies are in progress to improve the textural properties and enhance the effectiveness of the bio-waste based AC for VRB applications.

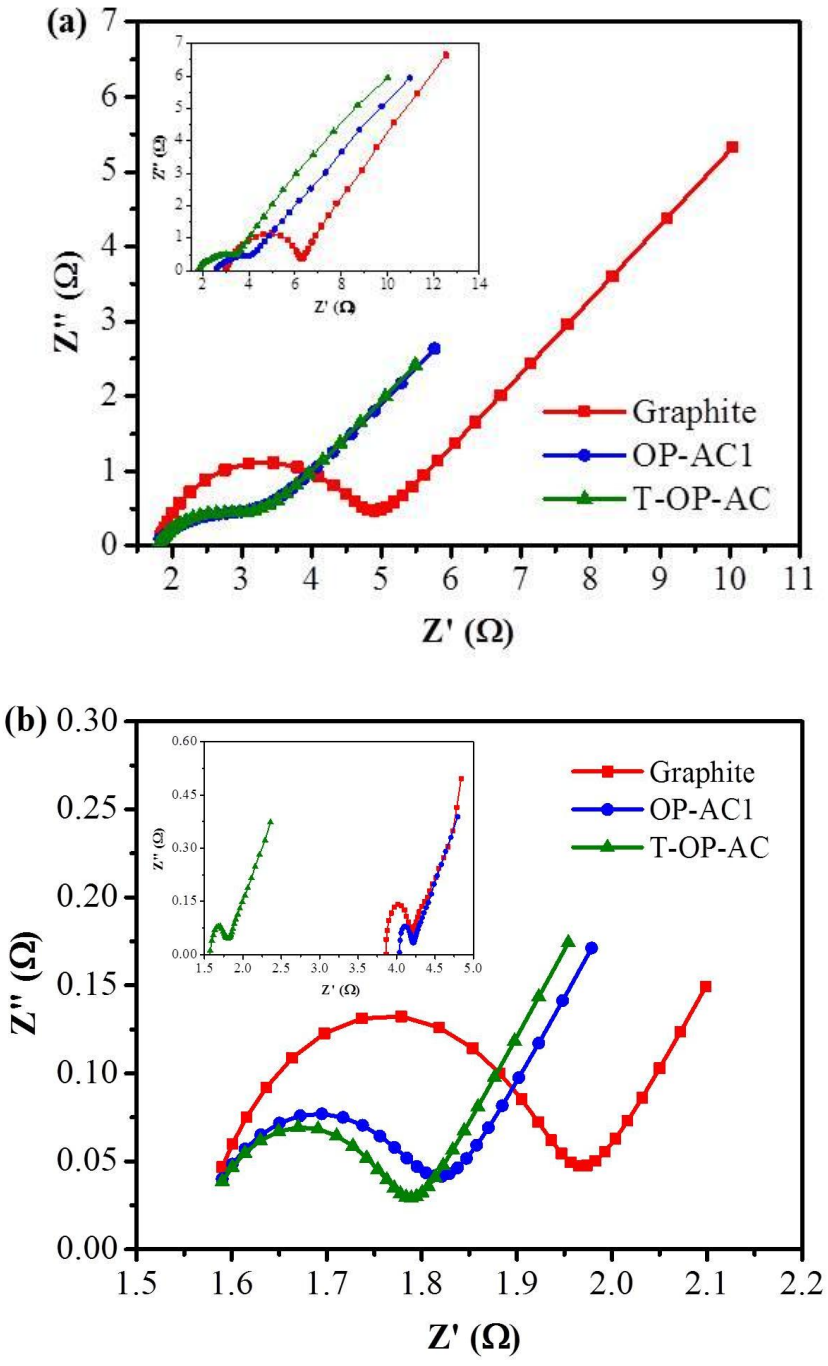

Figure 5.17. Nyquist plots of pristine, OP-AC1, and T-OP-AC coated bipolar plates recorded in frequency range of 100 kHz to 100 mHz at ac signal of 10 mV in $V^{2.5+}$ solution (a), and in $V^{4.5+}$ solution (b).

The proposed catalytic mechanism for the improved activity of T-OP-AC in VRB is illustrated in Figure 5.18. During the charging, VO^{2+} gets oxidized to VO_2^+ in the positive electrolyte, whilst V^{3+} gets reduced to V^{2+} in the negative electrolyte. For the positive electrolyte, based on the mechanism, C-OH functional group on the electrode surface acts as the active site for the oxidation of VO^{2+}. Firstly, VO^{2+} diffuses from the bulk solution to the electrode surface, and ion exchange occurs between the VO^{2+} ions and H^+ ion from the phenolic groups on the carbon surface (Figure 5.18a-1). In second step, transfer of electron from VO^{2+} to electrode along –C-O-V- bond and transfer of one oxygen atom from C–O group take place to form VO_2^+ (Figure 5.18a-2). Finally, ion exchange takes place between VO_2^+ ions and H^+ ion from the solution, and diffuses to bulk solution (Figure 5.18a-3). Whereas during discharge, the reaction occurs slowly in opposite direction due to the bulky VO_2^+ ion attached with C–O functional group. Hence, the process on positive electrode is associated with transfer of oxygen atom, which is likely to be the rate determining step. Nevertheless, this can be overcome by surface modification of carbon materials for increasing the concentration of oxygen functionalities. In the negative electrolyte, during charging process, diffusion of V^{3+} takes place from bulk solution to the electrode surface. Initially, ion exchange takes place between V^{3+} ions and H^+ ion from the phenolic groups (Figure 5.18b-1), followed by electron transfer from electrode to V^{3+} along –C-O-V- bond forming V^{2+} (Figure 5.18b-2). Finally, ion exchange occurs between V^{2+} and H^+ from the solution, and diffuses to bulk solution (Figure 5.18b-3). The discharge process is reversed of the charging process.

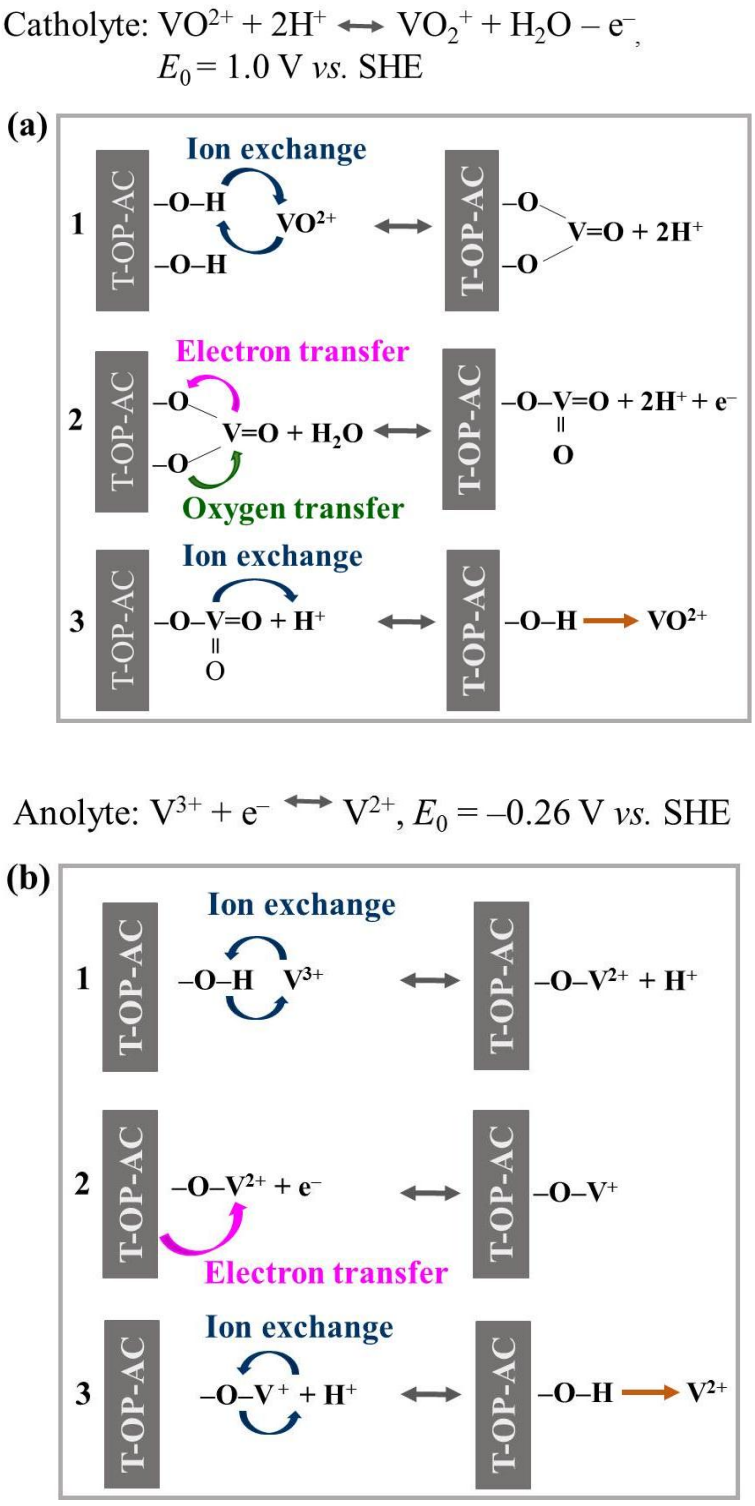

Figure 5.18. Schematic illustration of the redox reaction mechanisms for: VO_2^+/VO^{2+} redox couple in positive electrolyte (a), and V^{2+}/V^{3+} redox couple in negative electrolyte (b) (based on the mechanism proposed by Sun and Skyllas-Kazacos [200]).

5.3.9 VRB cell performance

Figure 5.19 presents the charge-discharge profiles of the cell with pristine and OP-AC coated bipolar plates at current density of 5 mA cm^{-2}. As can be seen, the OP-AC coated bipolar plate maintains stable charge-discharge performance and exhibits enhanced capacity compared with the pristine electrode. Comparison of voltage and energy efficiencies of the cells with bipolar plate and OP-AC coated bipolar plates at different current densities are shown in Figure 5.20a and b, respectively. The cell employing OP-AC coated bipolar plate exhibits higher energy and voltage efficiencies at all current densities tested, which can be due to the improved electrochemical activity, and better contact between porous felt and bipolar plate interface.

The porosity of the graphite felt was reduced to about 87% after compression. Considering the 10% contribution of OP-AC coated layer with respect to total thickness of active layer and 66% porosity against 87% porosity of graphite

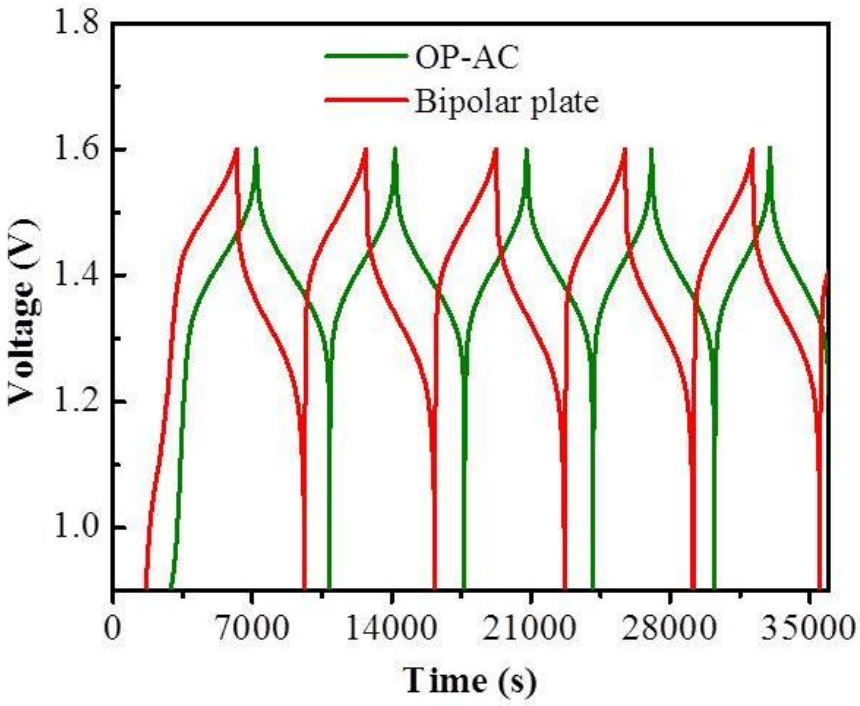

Figure 5.19. Comparison of pristine and OP-AC coated bipolar plates: Typical charge-discharge profiles at current density of 5 mA cm^{-2}.

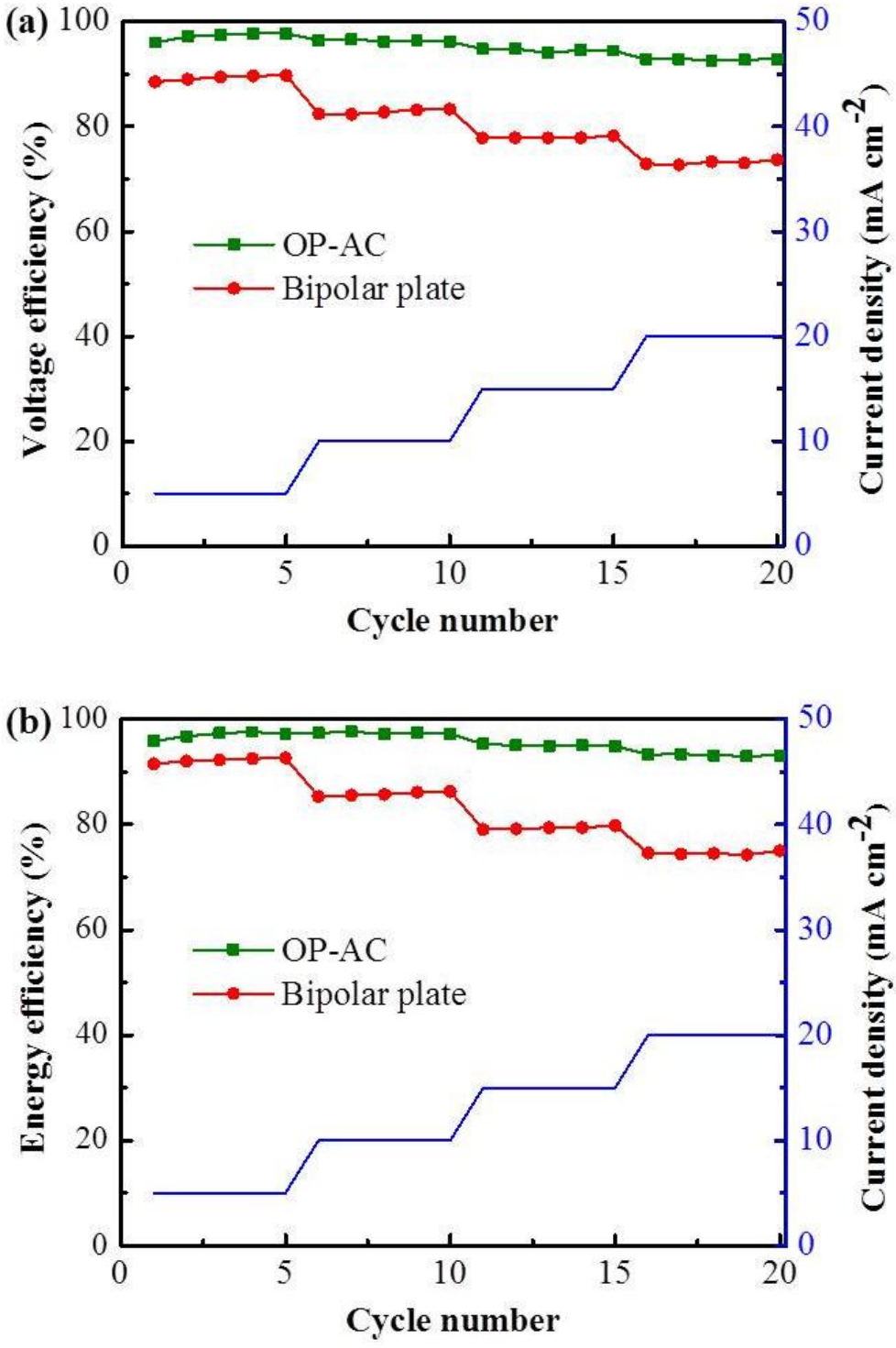

Figure 5.20. Comparison of voltage efficiency (a), and energy efficiency (b) at different current densities for pristine and OP-AC coated bipolar plates.

felt, the electrolyte volume of about 8% would likely reach the OP-AC coated layer effectively resulting in improved electrochemical reaction, as indicated in the CV result. In addition, the presence of rich oxygen functional groups as evidenced by XPS results should also contribute to the improved electrochemical performance. It should be noted that the estimated 8% of electrolyte reaching the coating layer is valid as electrolyte was contained in the porous electrode in a static cell. In a conventional flow cell, the permeability will further reduce according to Carman-Kozeny equation for porous media flow. Therefore, the electrochemical contribution might be negligible in a flow cell; however, the contribution of the improved contact resistance will still be effective.

In order to assess the performance stability, the cells were further tested at a constant current density of 20 mA cm^{-2} for 100 cycles (Figure 5.21). The OP-AC coated layer remained intact without peel off after long term test. Table 5.5 presents the average coulombic efficiency (CE), energy efficiency (EE) and voltage efficiency (VE) values at different current densities. The voltage and energy efficiencies decrease at higher current densities, which are due to the increased iR drops with increase in current densities. A slight decreasing of energy efficiency

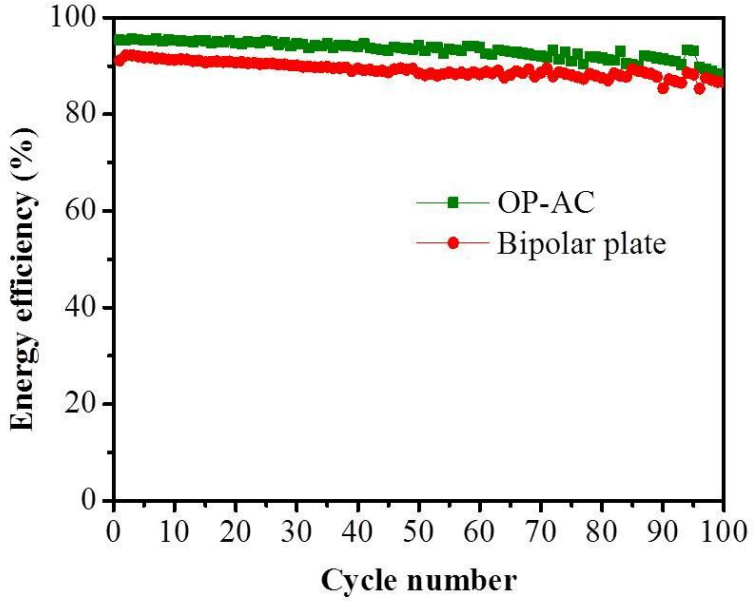

Figure 5.21. Long term performances with pristine and OP-AC coated bipolar plates at a constant current density of 20 mA cm^{-2}.

Table 5.5. Average coulombic, energy and voltage efficiencies of pristine and OP-AC coated bipolar plates in VRB.

Current density (mA cm^{-2})	Bipolar plate (Pristine)			OP-AC		
	CE%	EE%	VE%	CE%	EE%	VE%
5	97.8	95.2	97.3	99.9	97.8	97.8
10	98.0	93.6	95.5	99.7	97.4	97.6
15	98.2	91.9	93.6	99.8	95.5	95.6
20	98.7	90.5	91.7	99.9	94.3	94.4
20[#]	97.9	89.2	91.1	99.6	93.1	93.5

Each average value is obtained from 5 charge-discharge cycles unless mentioned, and repeated twice.

[#]Efficiency values are average of 100 charge-discharge cycles.

with time during long-term cyclic operation was possibly due to side reactions, collector surface passivation, etc. [203, 204]. The cell performance in present study are superior to the previously reported study with coconut shell derived AC [6].

It should be noted that the advantage of energy efficiency of approx. 4 % of the OP-AC reduced after 100 cycles. The faster drop of energy efficiency with OP-AC electrode was mainly due to the effect of longer cycle (charging and discharging) time as compared to that of pristine bipolar electrode. As both cells were tested in a constant voltage cut-off mode, therefore, longer cycle time (or higher SOC) was obtained for the cell with OP-AC electrode, due to the higher voltage efficiency. The longer cycle time of OP-AC increased cross-over, i.e. increased electrolyte imbalance, which resulted in the higher reversible drop of energy efficiency and capacity.

5.4 Conclusions

High surface area activated carbons have been synthesized from abundantly available bio-waste orange peel to be used as potential electrodes for VRB. The OP-AC and OP-AC1 coated bipolar plates exhibited improved electrochemical properties toward both the V^{2+}/V^{3+} (the negative half-cell) and V^{4+}/V^{5} (the positive half-cell) redox couples of the VRB compared with the pristine electrode.

The VRB performance in a static cell delivers higher voltage and energy efficiencies for OP-AC electrode compared with the pristine electrode at all current densities tested. The concentrations of some surface oxygen functional groups increased after acid treatment of the as-synthesized orange peel waste derived AC (OP-AC1). The surface modified OP-AC1 (T-OP-AC) based electrode is found to exhibit better electrochemical properties toward the vanadium redox couple reactions compared with graphite and OP-AC1 electrodes with the electrochemical kinetics of the redox reactions in the order of T-OP-AC > OP-AC1 > graphite. The improved activity of T-OP-AC is attributed mainly to the increased concentration of C–O and O–C=O groups. The findings indicate that the oxygen functionalities facilitate the charge transfer processes by providing more active sites and improving the wettability of the electrode. Textural properties (such as surface area, pore size distribution) of carbon materials also play important roles in electrochemical performance. High surface area accommodates more ions in the electrodes and its well-developed porous structure facilitates fast transport of ions, which subsequently offer positive effects in the electrochemical performance. Both surface area and oxygen-containing surface functional groups of carbons play crucial roles on the electrode performance.

The findings open up the possibility for utilizing this renewable bio-waste as potential precursor for AC preparation, and further improving the performance of the as-synthesized AC as electrode via facile surface modification by treating with the oxidative agent, 65 wt% HNO_3 solution for the VRB and other novel applications. The as-synthesized bio-waste derived ACs can also be considered as potential precursors to produce conducting plastics to lower the VRB stack cell weight and cost. In VRB, new design approaches are also equally explored. To

reduce the through plane resistivity, thin electrodes (paper electrodes) are being investigated. However, such thin electrodes suffer from poor electrochemical surface area. Therefore, embedding the as-synthesized high surface area carbon on the carbon paper will increase the surface area of the thin paper electrodes.

CHAPTER 6

Bio-Waste Derived Porous Carbon as Electrode for Lithium Ion Capacitors

The findings in this chapter were published as an original research paper: M. Maharjan, M. Ulaganathan, V. Aravindan, S. Sreejith, Q. Yan, S. Madhavi, J.-Y. Wang, T.M. Lim, Fabrication of High Energy Li–Ion Capacitors from Orange Peel Derived Porous Carbon, ChemistrySelect 2(18) (2017) 5051-5058.

6.1 Introduction

Energy storage devices, such as supercapacitors, have potential applications in electric vehicles, uninterruptable power supplies, low-energy industrial equipment, consumer electronics, power grid etc. In supercapacitors also called as electrical double layer capacitors (EDLC), electric double layer is formed at the interface between porous carbon and electrolyte solution. This electric double later store up the electric energy, and charge and discharge of electrical energy occur without faradaic reaction. Supercapacitors have drawn considerable attention as a clean energy storage system due to longer cycle life and higher power density than conventional rechargeable batteries [205]. However, limited specific energy is considered as the major issue for supercapacitors [53, 206]. Batteries, on the other hand, have poor power capability and limited cycle life, which are considered as main drawbacks for rechargeable batteries. Increasing the power capability of secondary batteries for the practical application is hindered due to the limited ion diffusion kinetics *via* Faradaic reactions. Research works have made tremendous efforts and have taken various approaches to advance the electrochemical performances in the areas of energy storage applications [207-209]. Enhancing the specific energy of supercapacitors is possible by employing organic electrolyte in place of aqueous electrolyte or fabricating the supercapacitors in asymmetric fashion with either pseudo-capacitive or insertion type electrodes [210-212]. Thus,

there has been growing research interest on the development of high energy supercapacitors for practical applications.

Activated carbon (AC) has been extensively studied as electrode material for supercapacitor applications irrespective of symmetric or asymmetric assemblies. AC possesses several favorable properties towards the construction of high performance supercapacitors. High specific surface area, tailored meso-/micro-porosity, good electrical conductivity, appreciable physico-chemical stability, low cost and environmental-friendliness are attractive features of AC [102, 206]. Researchers have explored various synthesis routes for preparation of ACs with tailored porosity towards supercapacitor applications [3-5, 86, 90]. According to the energy storage mechanism of EDLCs, specific surface area of AC plays an important role in delivering the higher specific EDLC capacitance. However, pore structure and surface chemistry of ACs also have crucial roles in the electrochemical performance of supercapacitors [1, 213].

Utilization of biomass waste offers the combined advantages of re-cycling, reduction in the use of non-renewable resources and contribution towards clean environment. For energy storage applications, researchers have investigated various biomass as carbon precursors for electrodes, such as neem leaves [9], waste tea leaves [214], coffee ground [107], rice husk [4], wheat straw [12], tree bark [215], among others. The worldwide production of citrus fruits production in 2016 was reported 124 million tonnes with ~67.0 million tonnes of oranges [145]. The fruit peels pose a serious disposal problem in regions with large production [146]. This underutilized bio-waste could be alternative good resource as precursor for the synthesis of value-added products, such as porous carbon. Studies have utilized orange peels for producing hydrochars as adsorbent for metallic ions from aqueous solutions [99, 151-154]. ACs have also been reported as adsorbents for dyes and organic contaminants [146, 149, 150]. There has been a study on the application of orange peel derived AC as cathode for lithium ion capacitor (LIC) [156], however, the study was restricted to only half-cell and not the whole LIC assembly and hence the specific energy could not be reported. Other also reported the application of orange peel derived AC on hybrid capacitor with MnO_2 [147].

In this work, porous carbon was synthesized from abundant and environmentally-friendly bio-waste, orange (*Citrus sinensis*) peel via chemical activation. The performance of the as-synthesized AC as electrode material was evaluated on capacitors. The orange peel derived AC was employed for fabrication of high specific energy lithium ion capacitors (LICs) and symmetric capacitor configurations for comparison purpose. The performance of the capacitors are evaluated and reported in terms of specific energy. Firstly, aqueous symmetric capacitor was fabricated and the specific energy was enhanced by replacing non-aqueous solution. Then, the specific energy of organic symmetric capacitors was further enhanced by pairing with insertion type $Li_4Ti_5O_{12}$ and pre-lithiated graphite (LiC_6) in the same organic electrolyte. Different material characterization and electrochemical measurement tests were carried out for detail study of the precursor material, and the as-synthesized AC as electrode for high energy capacitors.

6.2 Experimental

6.2.1 Precursor material

The orange peels were collected from oranges purchased in a local supermarket, Singapore. Yellow colored fine orange peel powder (OP) was obtained following the procedure described in Section 3.1 (Chapter 3). The sample powder was collected in clean dry bottles, and stored in desiccators until used.

6.2.2 Synthesis of porous activated carbon

The OP was charred to yield OP derived char (OPC), and porous AC was synthesized impregnating OPC with KOH (OPC:KOH = 1:2) following the procedures described in Section 3.6, Chapter 3. The resultant product was designated as OP-AC and stored in desiccators for further studies.

6.2.3 Physico-chemical properties

Characterization of the OP-AC was carried out for the elemental composition, textural, morphological (microstructure), nanostructural features and surface

chemistry. The tests performed were elemental analysis, thermogravimetric analysis (TGA), field emission-scanning electron microscopy (FE-SEM), transmission electron microscopy (TEM), X-ray diffraction (XRD), Raman spectroscopy and X-ray photoelectron spectroscopy (XPS) following the procedures described in relevant sections in Chapter 3. The surface area of OP-AC was obtained from the BET method with the adsorption in the relative pressure (P/P_o) of 0.10. The total pore volume (V_T) was derived from the amount of Nitrogen adsorbed at a relative pressure of 0.95. The micropore volume (V_{micro}) and micropore surface area (S_{micro}) were obtained from t-plot method with a relative pressure of 0.15-0.5. The PSD was measured from the desorption points using DFT pore size distribution.

6.2.4 Electrochemical measurements

6.2.4.1 OP-AC||OP-AC in aqueous electrolyte

Symmetric assembly (OP-AC||OP-AC) was tested in aqueous electrolyte. For the electrodes preparation, weighed amounts of OP-AC (85 wt%), carbon black (10 wt%) and polyvinylidene fluoride (PVDF, 5 wt%), as a binder were mixed. The mixture was ground in an agate mortar, and then measured amount of N-Methyl-2-pyrrolidone (NMP) solution was added and mixed thoroughly to form thick slurry. The prepared slurry was coated on the toray carbon paper in 1 cm^2 area, and the coated papers were placed in vacuum at 60 °C for overnight. CV studies of symmetric supercapacitors (OP-AC||OP-AC) were performed in an aqueous electrolyte (1 M H_2SO_4) between a potential range of 0-0.8 V at different sweep rates.

6.2.4.2 OP-AC||OP-AC in non-aqueous electrolyte

The electrochemical performance of OP-AC||OP-AC was studied by testing in organic electrolyte in two electrode coin-cell (CR2016) assembly. The electrodes were prepared with OP-AC (80 wt%), carbon black (10 wt%) and teflonized acetylene black (10 wt%, TAB-2) binder using ethanol as solvent. The mixture was ground in an agate mortar, thoroughly mixed and the homogenous slurry was pressed over thick stainless-steel mesh of 0.25 mm thick with 2 cm^2 area

(Goodfellow, UK), and then placed in vacuum oven at 60 °C for overnight. For the supercapacitors assembly, two symmetric electrodes were separated with Whatman paper (Cat. No. 1825-047, UK) and employed 1 M lithium hexafluorophosphate ($LiPF_6$) in ethylene carbonate (EC):di-methyl carbonate (DMC) as electrolyte.

6.2.4.3 LIC with metal oxide (OP-AC||$Li_4Ti_5O_{12}$)

For LIC assembly with metal oxide (OP-AC||$Li_4Ti_5O_{12}$), the electrode was prepared with $Li_4Ti_5O_{12}$ (80 wt%), carbon black (10 wt%) and teflonized acetylene black (10 wt%, TAB-2) in ethanol. The cell was fabricated as described earlier for non-aqueous electrolyte in which $Li_4Ti_5O_{12}$ and OP-AC were employed as negative and positive electrodes, respectively.

6.2.4.4 LIC with graphite (OP-AC||LiC_6)

For LIC assembly with graphite (OP-AC||LiC_6), graphite (Aldrich, USA) was electrochemically pre-lithiated prior to LIC fabrication. In such process, the electrode was cycled in half-cell configuration for two complete cycles and discharged to 0.005 V *vs.* Li (at specific current of 100 mA g^{-1}) in Swagelok fittings, and dismantled. Then, LiC_6 was subsequently paired with OP-AC under the optimized loadings by re-filling fresh electrolyte in coin-cell (CR2016) configuration.

Galvanostatic charge-discharge (GCD) and electrochemical impedance spectroscopy (EIS) measurements were performed for studying electrochemical performance of the fabricated assemblies. GCD measurements were performed in Arbin BT 2000 battery tester at room temperature conditions. EIS measurements were conducted in Solartron workstation (1470E) using 1 M H_2SO_4 (aqueous) and 1 M $LiPF_6$ in EC:DMC (organic) electrolytes. The frequency was set from 100 kHz to 0.1 Hz in the presence of an ac perturbation of 10 mV at open-circuit voltage for all the studied systems of supercapacitors.

6.3 Results and Discussion

6.3.1 Elemental and proximate contents

The elemental and proximate analysis results of OP and elemental composition of OP-AC from this study are presented and discussed in in Section 5.1, Chapter 5.

6.3.2 Textural properties

The results of nitrogen adsorption-desorption studies of OP-AC are presented in Section 5.3.5 and Figure 5.5a (Chapter 5), which suggests a combination of both type I and IV isotherms. The BET surface area is calculated to be 1901 $m^2\ g^{-1}$ with S_{micro} of 1407 $m^2\ g^{-1,}$ and total pore volume of 0.94 cc g^{-1}. Majority of the pores have narrow width of 11.26 Å. Specific surface area of electrode material plays an important role in the accumulation of charge carriers for the double layer formation across the electrode/electrolyte interface, and contributes in electrical energy of the supercapacitors.

6.3.3 Morphological and pore properties

The FE-SEM images of OP-AC are provided in Figure 5.6a and b in Section 5.3.6, Chapter 5, which illustrates well-developed pores and porous network-like structures. Furthermore, the porous nanostructure of the sample is clearly observed in the TEM image (Figure 5.6e). The intercalation of K^+ ions in activation process using KOH as an activating agent helps to create interconnected pores. High specific surface area and well-developed porous structure of carbon material offer positive effects in the electrochemical performance thereby providing more active sites for the electrical double layer formation and allowing fast ion diffusion. The BET specific surface areas for the AC from OP obtained in this study and reported in previous publications are summarized in Table 6.1. OP-AC has the highest surface area, which is good for supercapacitor applications.

Table 6.1. Processes, products, carbon content, BET specific surface area and applications of orange peel based-resultant products.

Process	Resultant product	C%	S_{BET} (m^2 g^{-1})	Application	Ref.
chemical	activated carbon	82.5	1090	adsorbents (dyes)	[146]
hydrothermal, pyrolysis	biochars	62.0-78.7	-	adsorbent (Cu II)	[151]
Pyrolysis	biochars	50.6-77.8	-	adsorbents (organic pollutants)	[99]
hydrothermal	hydrochar	68	-	-	[154]
chemical	activated carbon	-	-	adsorbent (Direct Blue-86)	[154]
hydrothermal, chemical	hydrochars, activated hydrochars	65.8-84.2	117-618	Adsorbents	[149]
chemical, microwave	activated carbon	72.7	1105	Adsorbents (Methylene blue)	[150]
chemical	activated carbon	-	4.3-1207	supercapacitors	[156]
pyrolysis	activated carbon	-	500	supercapacitors	[147]
chemical	activated carbon	82.8	1901	supercapacitors	This study

6.3.4 Structural properties and Surface chemistry

The XRD, Raman spectroscopy and XPS analysis of OP-AC were carried out for studying the structural properties of OP-AC. The results from these tests are described and illustrated in Section 5.3.7 and Figure 5.9 (Chapter 5). In summary, the observed peaks from XRD pattern suggest amorphous semi-graphitic carbon, and the I_D/I_G ratio of 0.99 from Raman spectroscopy indicates the existence of substantial amounts of defects and disordered structures in the sample. The XPS results shows the presence of abundant carbon functionalities (sp^2 C=C and

sp^3 C–C) and oxygen containing functional groups (C=O and C–O) on the sample surface. The presence of rich oxygen containing functional groups on the surface of sample is beneficial for better electrochemical processes.

6.3.5 Electrochemical performance

The EDLC performance of OP-AC was evaluated using symmetric cell configuration in aqueous medium (1 M H_2SO_4) with a positive sweep potential range from 0 to 0.8 V. The cyclic voltammetry (CV) studies are conducted to ensure the electrical double layer behavior *via* non-Faradaic process in the electrode/electrolyte interface. Figure 6.1a demonstrates quasi-rectangular shaped traces, which confirms the double layer formation and good capacitive behavior. The specific capacitance of the symmetric system is about 90 F g^{-1} at sweep rate of 20 mV s^{-1}. The CV curves retain their quasi-rectangular shape even at higher scan rate of 100 mV s^{-1}, indicating high power capability of the OP-AC. This good capacitive behavior of OP-AC logically led to fabricate the high energy supercapacitors with different hybrid cell assemblies using organic electrolyte.

GCD curves of the OP-AC sample obtained at different specific current are shown in Figure 6.1b. From the plot, it is noted that the cell showed less ohmic drop even at high current density, and the calculated specific capacitance is also very close in agreement with the value obtained from CV curve. The calculated capacitance value (90 F g^{-1}) in an aqueous electrolyte is higher compared to the previously reported value of 51.7 F g^{-1} [156]. Prior to the fabrication of supercapacitor in asymmetric fashion with insertion type electrodes, symmetric configuration with organic solution (1 M $LiPF_6$ in EC:DMC) was tested. In the case of symmetric configuration, there is no need of balancing the load between the electrodes and thus formulation of electrode with the same mass loading is sufficient. On the other hand, in asymmetric configuration, the potential is split according to the charge storage capacity of the individual electrodes. The OP-AC obeys the non-Faradaic charge storage process, whereas $Li_4Ti_5O_{12}$ and graphite undergo the intercalation process. Therefore, mass loading between the two

electrodes are very crucial to yield the high specific energy [216]. In this regard, all the three electrodes employing OP-AC, $Li_4Ti_5O_{12}$ and graphite were studied in the

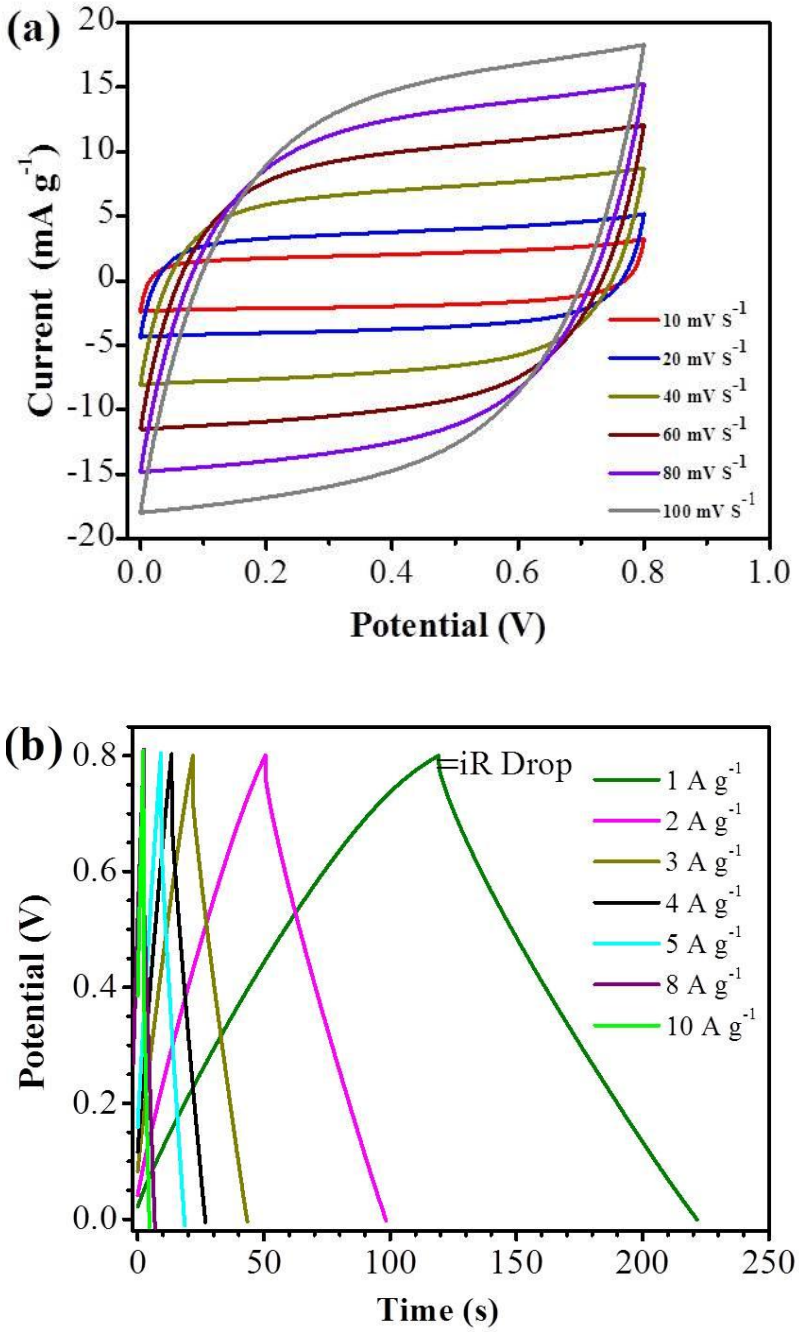

Figure 6.1. Cyclic voltammogram at different scan rates (a), and GCD curves at different current rates (b) of OP-AC in symmetric supercapacitor configuration (Electrolyte: 1 M H_2SO_4).

single electrode configuration with metallic Li. Based on the single electrode/half-cell performances of the materials, the mass loadings between the anode to cathode were adjusted to 1:3.4 (3 mg:10.2 mg) and 1:4.9 (3 mg:14.7 mg) ratios for OP-AC||Li4Ti5O12 and OP-AC||LiC_6, respectively (Figure 6.2, Figure 6.3 and Figure 6.4). The graphite is electrochemically pre-lithiated (LiC_6) prior to the fabrication of high voltage assembly with OP-AC. It was noted that the OP-AC sample delivered a capacitance of 112.5 F g^{-1} (Figure 6.4) at a potential window of 3-4.6 V in organic electrolyte. Whereas the previous report on orange peel derived activated carbon used as LIC's cathode delivered the capacitance of 51.7 F g^{-1} in 1 M $LiPF_6$ in EC/EMC/DMC (1:1:1 v/v) solution at sweep rate of 1 mV s^{-1} [156]. In comparison, the capacitance obtained (112.5 F g^{-1}) in this work is 2.2 times higher than the previously reported value (51.7 F g^{-1}) in organic electrolyte at the same voltage window.

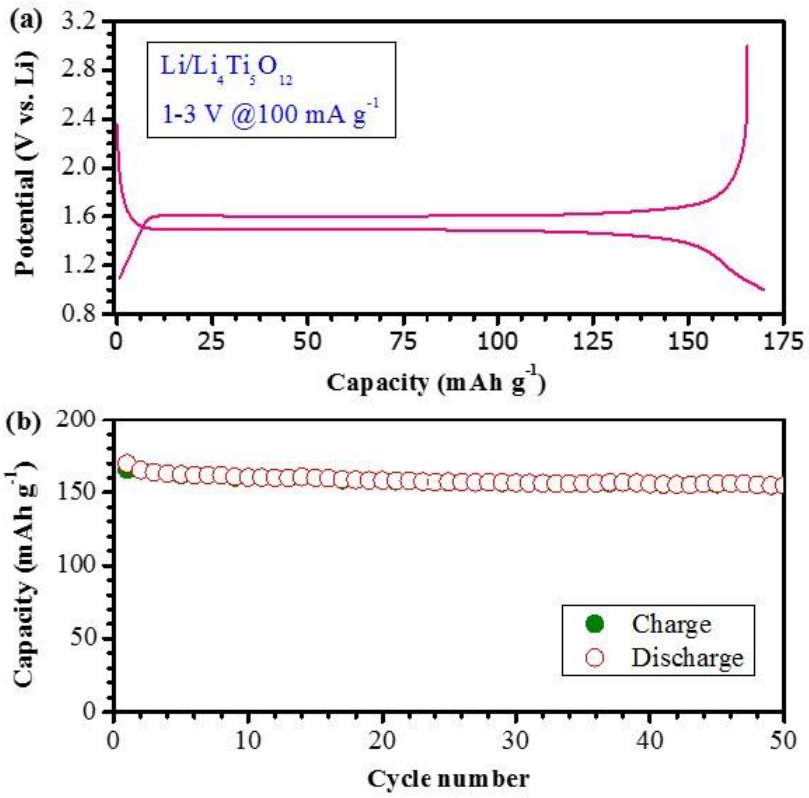

Figure 6.2. Galvanostatic charge-discharge curves of Li/$Li_4Ti_5O_{12}$ (Aldrich, USA) half-cells cycled between 1-3 V at constant current density of 100 mA g^{-1} (a), and Plot of discharge capacity *vs.* cycle number (b).

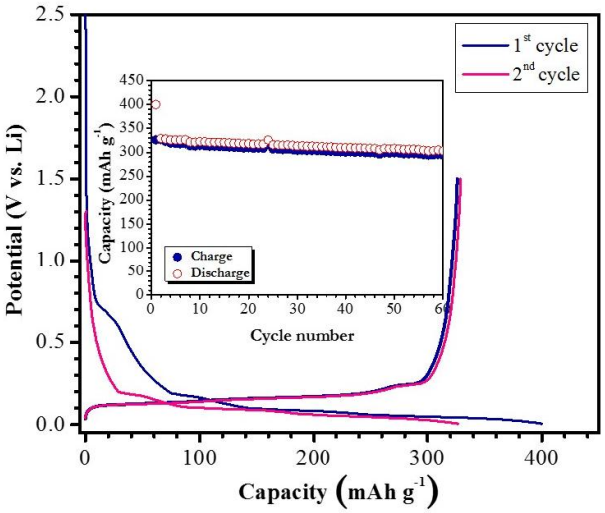

Figure 6.3. Galvanostatic charge-discharge curves of commercial graphite (Aldrich, USA) in half-cell assembly 0.005-1.5 V *vs.* Li at current density of 100 mA.

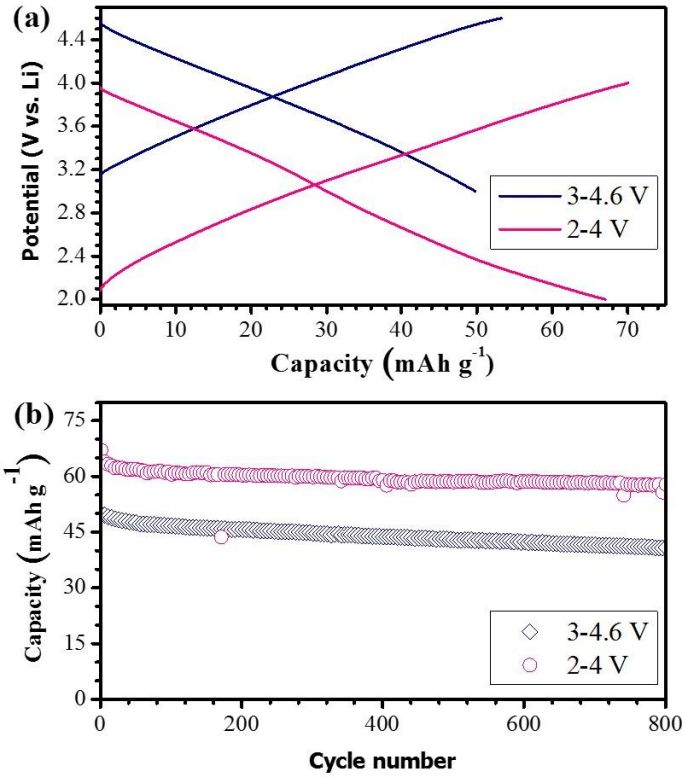

Figure 6.4. Typical galvanostatic charge-discharge curves of OP-AC in half-cell (single electrode) assembly at two different cut-off potentials at current density of 100 mA g^{-1} (a), and the 3-4.6 V *vs.* Li region has been used for the mass loading with $Li_4Ti_5O_{12}$, whereas 2-4 V *vs.* Li region has been used for LiC_6 (b).

Figure 6.5 (a-c) shows GCD studies of different capacitor configurations, such as OP-AC||OP-AC, OP-AC||$Li_4Ti_5O_{12}$ and OP-AC||LiC_6, respectively at different current densities. The current densities are determined from the total mass loading of both electrodes. Both aqueous and organic symmetric supercapacitors obey the non-Faradaic mechanism, and both anions and cations involve in the double layer formation with OP-AC electrode across the electrode/electrolyte interface. On the other hand, both LIC's (OP-AC||$Li_4Ti_5O_{12}$ and OP-AC||LiC_6) undergo two different mechanisms, e.g. Faradaic type in battery electrode ($Li_4Ti_5O_{12}$ and LiC_6) anode and non-Faradaic type in the OP-AC. More clearly, the Li^+ ions are inserted/extracted during charge-discharge process, while anions (PF_6^-) are involved in the double layer formation with OP-AC. Since the Li-insertion potential of graphite is <0.1 V *vs.* Li, there is no obvious deviation from the linear

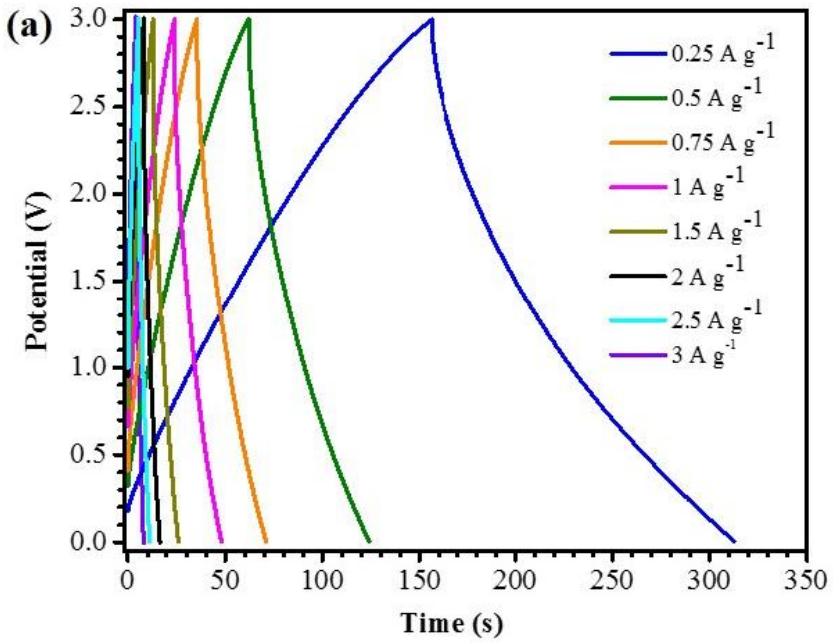

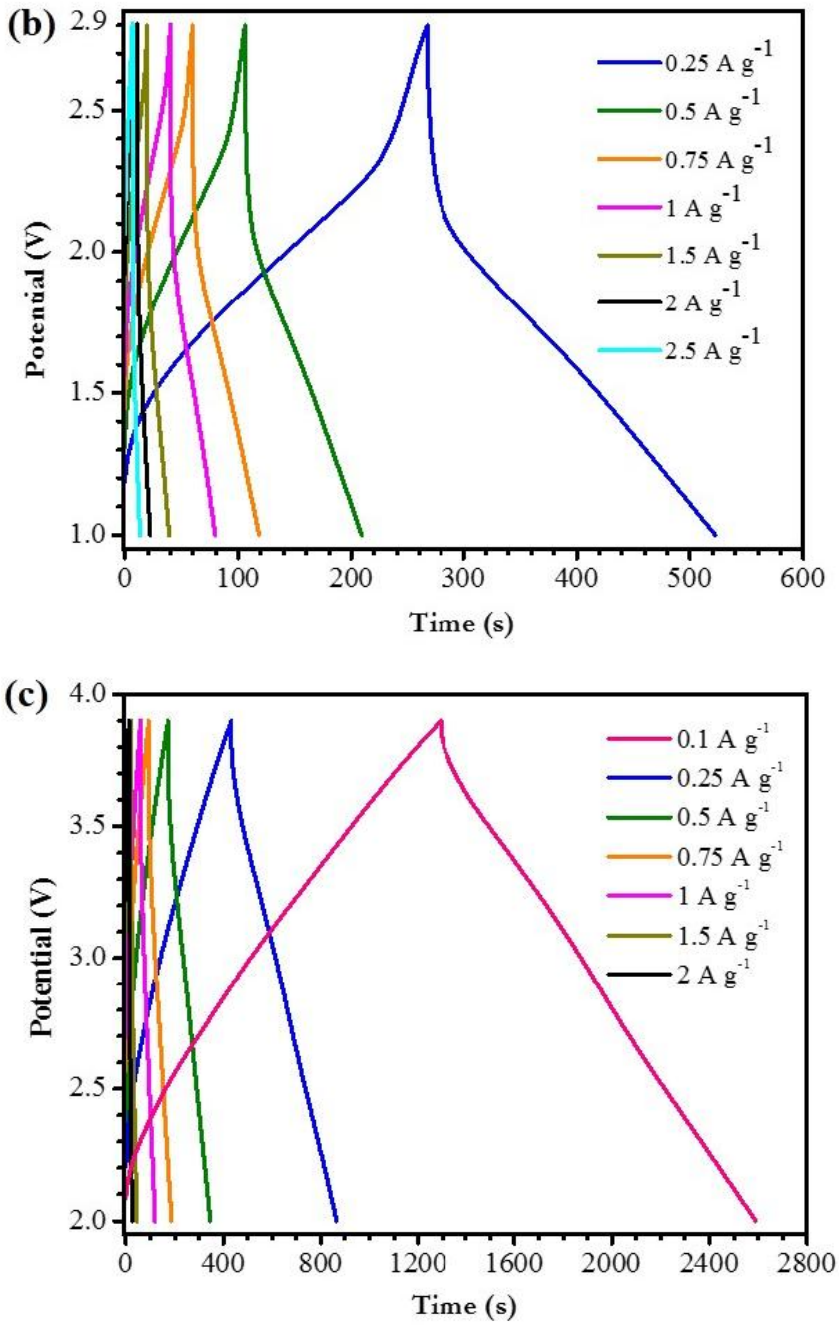

Figure 6.5. Typical GCD studies of OP-AC in different configurations: Symmetric configuration (OP-AC||OP-AC) with organic electrolyte (1 M $LiPF_6$ in EC:DMC) (a), LIC assembly with metal oxide (OP-AC||$Li_4Ti_5O_{12}$) (b), and LIC assembly with graphite (OP-AC||LiC_6) (c).

curves. However, the insertion potential of $Li_4Ti_5O_{12}$ is higher (~1.5 V *vs.* Li), hence non-linear curves are noted for the $Li_4Ti_5O_{12}$ based LIC. Irrespective of the

configurations, increasing current tends to decrease discharge time, which is primarily due to the limited involvement of the active material in the electrochemical reaction.

Specific energy and power of all four capacitors are summarized in Ragone plots (Figure 6.6). Here, the average working potential ($\Delta E = \frac{(E_{max}+E_{min})}{2}$, where E_{max} and E_{min} are the maximum and minimum potentials of the GCD cycle) of 0.4, 1.5, 2 and 2.95 V are considered for OP-AC||OP-AC (aqueous), OP-AC||OP-AC (organic), OP-AC||$Li_4Ti_5O_{12}$ and OP-AC||LiC_6 configurations, respectively. Accordingly, the specific energy (E_{sp}) and specific power (P_{sp}) are obtained using the following equation:

$$P_{sp} \times t \text{ and } P_{sp} = \frac{\Delta E \times i}{m}$$

where:
m is active mass loading of both electrodes (kg), *t* is discharge time (s), and *i* is applied current (A).

The maximum specific energy of ~8.0, ~16.3, ~35.3 and ~106.1 Wh kg^{-1} is noted for OP-AC||OP-AC (aqueous), OP-AC||OP-AC (organic), OP-AC||$Li_4Ti_5O_{12}$ and OP-AC||LiC_6 configurations, respectively (Table 6.2). A notable improvement in the specific energies is achieved by altering the electrolyte and electrode materials. Slightly lower current rates (0.1 A g^{-1}) are applied for OP-AC||LiC_6 assembly compared to other three configurations to realize the high specific energy. It is well known fact that, graphite always exhibits poor rate performance upon high current operation. Nevertheless, OP-AC||LiC_6 cell delivered the specific energy of ~21 Wh kg^{-1} even at high power capability of 5.9 kW kg^{-1}. The reported specific energy in present work is much higher than previously reported values [217-219] as shown in Table 6.2.

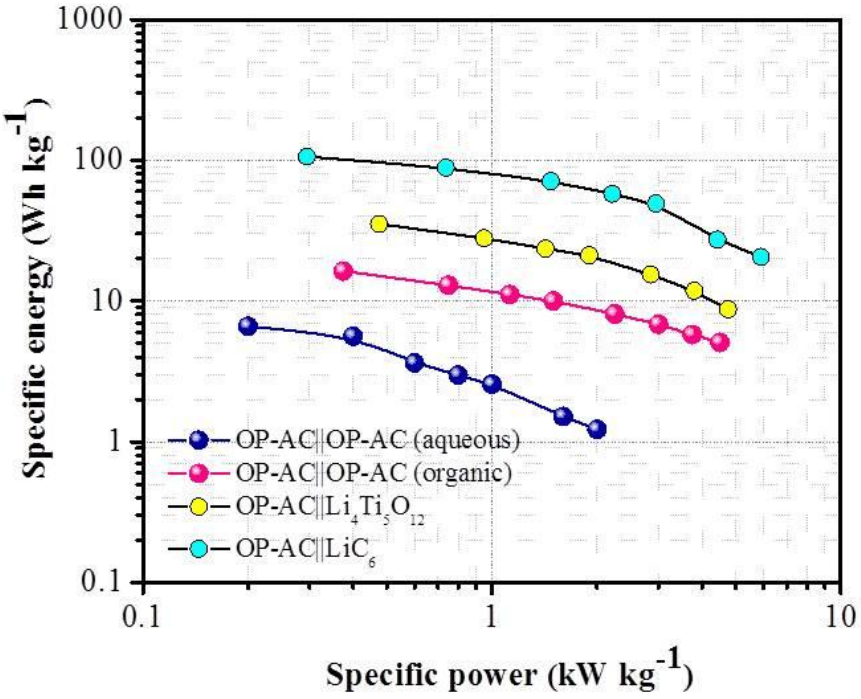

Figure 6.6. Ragone plot of OP-AC based different supercapacitors assemblies in aqueous and organic electrolytes.

In supercapacitors, cycling ability is considered one of the important parameters irrespective of symmetric or hybrid configurations. In this regard, cycling studies were conducted for all four cells at specific current of 1 A g^{-1}. The obtained values were normalized (Figure 6.7). Retentions of ~85.8, ~87.0 ~82.2 and ~58.8% were noted after 2500 cycles for OP-AC||OP-AC (aqueous), OP-AC||OP-AC (organic), OP-AC||$Li_4Ti_5O_{12}$ and OP-AC||LiC_6 configurations, respectively (Table 6.2). High specific energy was acquired for graphite based LIC (OP-AC||LiC_6), but it rendered poor cycling stability compared to other three configurations. This inferior cycling stability of the graphite based LIC (OP-AC||LiC_6) configuration is expected because graphite always has the high current testing issues. An improved cycling stability was noted for $Li_4Ti_5O_{12}$ based LIC (OP-AC||$Li_4Ti_5O_{12}$) compared to graphite based one. The performance of both LICs could be improved by adopting the carbon coating and matching to symmetric supercapacitor performance. Further efforts are in progress to enhance the electrochemical activity without compromising the energy and power capability issues.

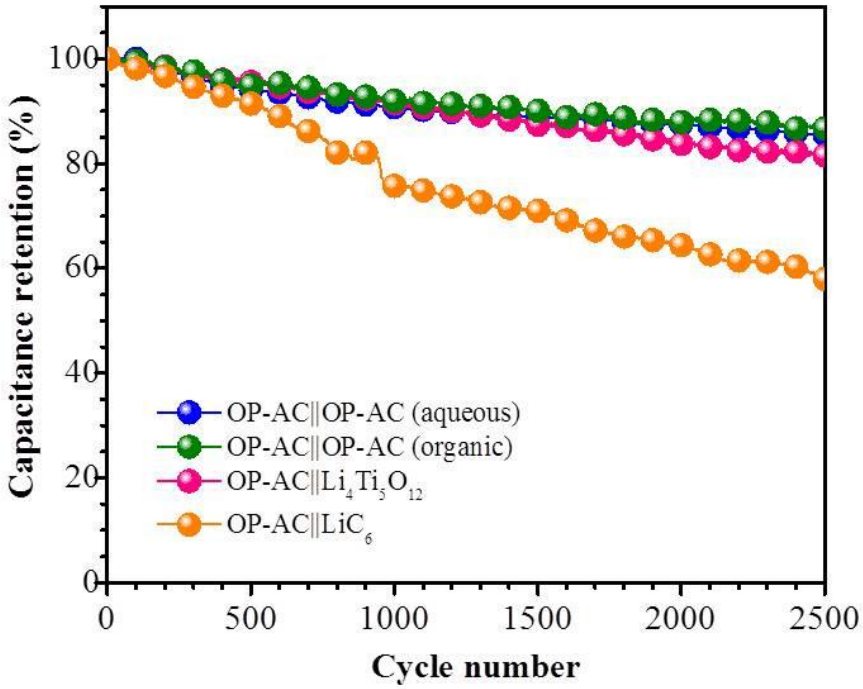

Figure 6.7. Cycling profiles of OP-AC based different supercapacitors assemblies tested in aqueous and organic electrolytes at current density of 1 A g^{-1}.

EIS is an informative technique to study charge storage kinetics and conductive properties of the electrode materials. Figure 6.8 shows the Nyquist plot for the studied systems of supercapacitors. Impedance plot of the cells depict a lower charge transfer resistance which lies in the range from 2 to 5 Ω, indicating the fast ion conducting behavior of the OP-AC, LiC_6 and $Li_4Ti_5O_{12}$ electrode materials. The deep extent of the linear spike obtained from the Nyquist plot in the lower frequency region suggests the good capacitive behavior of the electrode. In addition, the exceeding 45° inclined angle and the vertical line close to the 90° also reveals very good charge storage behavior of the electrode materials used in the cell fabrications [220].

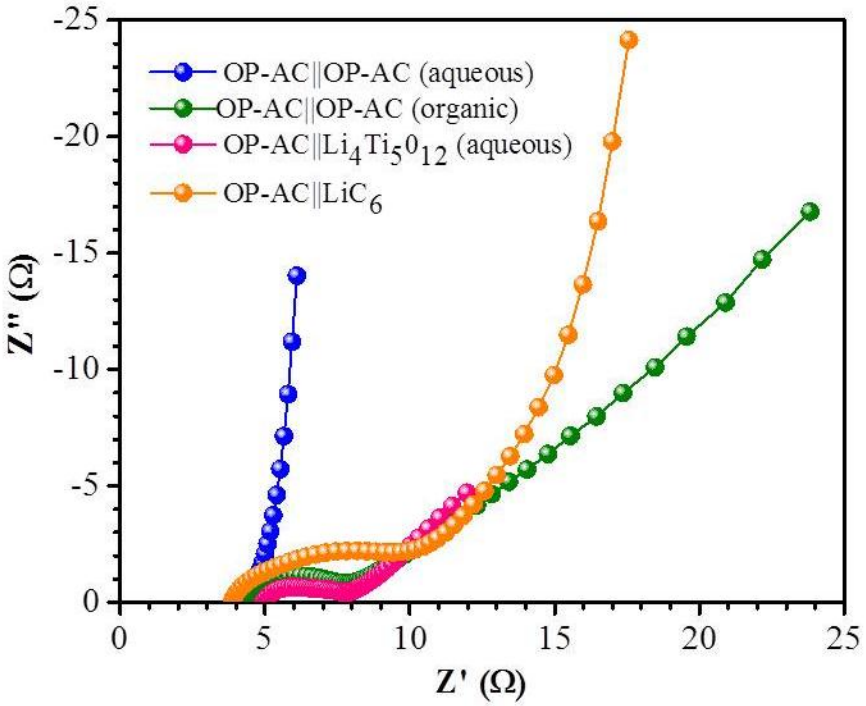

Figure 6.8. Nyquist plots of OP-AC based different supercapacitors assemblies tested in aqueous and organic electrolytes recorded between 100 kHz to 0.1 Hz wih an ac perturbation of 10 mV.

Table 6.2. Comparison of specific energy and cycling stability of various supercapacitors.

Electrode			Electrolyte	Specific Energy ($Wh\ kg^{-1}$)	Maximum cycles (Retention %)	Reference
Positive	**Negative**	**System**				
AC	Pre-lithiated Graphene	Hybrid	Organic	61.7	After 300 cycles (74%)	[217]
	Pre-lithiated Graphite			~28		
URGO	Li-Graphite	Hybrid	Organic	106	After 1000 cycles (~97%)	[218]
HRGO				~75		
AC				~80		
AC	Hard carbon with SLMP	Hybrid	Organic	82	After 600 cycles (~97%)	[219]
OP-AC	Tested against Li	Half cell	1 M $LiPF_6$	-	-	[147]
OP-AC||MnO_2	Tested against Hg/HgO	Three electrodes	6 M KOH	-	After 5000 cycles (~70%)	[147]
OP-AC	1) Pre-lithiated Graphite	Hybrid	1 M $LiPF_6$	1) ~106.1	1) 58.8 %	This study
	2) $Li_4Ti_5O_{12}$	Hybrid	1 M $LiPF_6$	2) ~35.3	2) 82.2 %	
	3) OP-AC	Symmetric	1 M $LiPF_6$	3) ~16.3	3) 85.8 %	
	4) OP-AC	Symmetric	1 M H_2SO_4	4) ~7.0	4) 87.0 %	

After 2500 cycles

AC = Activated carbon, URGO = urea reduced graphitic oxide, HRGO = hydrazine reduced graphitic oxide, OP-AC = orange peel derived AC, OP-AC = orange peel derived AC (OPC:KOH = 1:2 by weight)

To sum up, in this work, high surface area AC with well-developed pores and porous network-like structure was derived from bio-waste (orange peel), which was employed as the positive electrode in LICs. The BET surface area obtained in this study is much higher (1901 $m^2 g^{-1}$ vs previously reported 1207 $m^2 g^{-1}$). *For the first time, the fabrication of whole LIC assembly using OP-AC (i.e., OP-AC) to deliver high energy is reported. The calculated capacitance for the assembly is 112.5 F g^{-1}, which is more than twice that previously reported (51.7 F g^{-1})* [147].

6.4 Conclusions

The work has successfully demonstrated the feasibility of using bio-waste derived porous carbons as promising electrode materials towards the fabrication of high energy LICs. The orange peel derived activated carbon (OP-AC) is employed as electrode for the fabrication of high specific energy LIC with LiC_6. The OP-AC||LiC_6 capacitor can deliver maximum specific energy of 106.1 Wh kg^{-1}. Metal oxide based LIC (OP-AC||$Li_4Ti_5O_{12}$), symmetric supercapacitor with aqueous and organic solutions are also explored for comparison. The findings offer new opportunities to explore abundant, low cost, renewable bio-waste as potential carbon source for the development of high specific energy LICs and asymmetric supercapacitors.

CHAPTER 7

Bio-Waste Carbon Based Pseudo-capacitive Electrode for Aqueous Supercapacitors

The findings of this chapter are included in the original research paper: M. Maharjan, M. Ulaganathan, T. M. Lim, High surface area activated carbon for high energy aqueous supercapacitor. (Manuscript submitted, under review)

7.1 Introduction

The increasing energy demand has prompted the development of high performance energy storage systems in order to meet energy need of this 21st century. Supercapacitors offer potential applications as energy storage devices, such as portable electronics, electric vehicles, uninterruptable power supplies etc. due to their highly reversible charge storage process, longer cycle life and higher power density [45, 49, 221]. However, limited specific energy of supercapacitors is considered as the key issue [53, 206]. Thus, there has been increasing research interests to improve the performance of supercapacitors via different approaches, such as using favorable electrode materials, modifying textural properties of carbons, employing various electrolytes [4-5] and developing novel highly efficient energy storage devices.

Activated carbon (AC) is the primary choice for supercapacitor electrodes due to its attractive features, such as high surface area, good electrical conductivity, chemical stability, low cost, and environmental-friendliness [102, 222]. However, electrodes used in supercapacitors at present are made mainly from non-renewable resources, such as coal, coke. There is a need to search for potential alternative carbon precursors to decrease the increasing shortages of non-renewable resources and lower the environmental impact from greenhouse gases emission. Biomass has drawn huge attention for AC preparation due to its low cost, abundance and environmental friendliness. Researchers have investigated various biomass as

carbon source for electrodes [8-13] via various synthesis routes towards supercapacitor applications [1-7]. A literature review shows that Lychee (*Litchi chinensis*) peel, low cost agro-waste, has been scarcely investigated for its conversion to carbon materials [157], and none has reported its use as electrode for capacitor applications.

In recent years, there is a growing research interest on pseudocapacitors due to their high specific energies. Many metal oxides/hydroxides, such as MnO_2, NiO, RuO_2, $Ni(OH_2)$, $Co(OH)_2$, and conducting polymers (e.g., polyaniline, PANI) or carbon-based materials (e.g., graphene) are known as pseudo-capacitive materials. These materials undergo a fast redox reaction to deliver the capacitive responses and exhibit much higher specific energies than the carbon-based supercapacitors [223]. Graphene (Gr) exhibits high charge-discharge rates and good cycling stability, but delivers lower capacitance. Whereas, PANI displays higher capacitance but delivers poor cycle life and poor rate capability [223]. The electrochemical performances of commercial AC and conducting polymer, PANI composites on supercapacitors have been extensively investigated [224-229]. However, data on asymmetric capacitors comprising biomass derived AC and PANI or Gr/PANI electrodes are scare [230]. So far, lychee peel derived AC and Gr/PANI have not been investigated as electrode combinations in asymmetric supercapacitors. Detailed characterization study of a new precursor will be useful to know its intrinsic properties and potential applications.

In this work, AC is derived from a new precursor, a bio-waste lychee peel. The electrochemical performances of the synthesized AC as electrode material were evaluated in both the symmetric and asymmetric cell configurations. Furthermore, physico-chemical properties of the synthesized AC were studied in detail by various characterization tests.

7.2 Experimental

7.2.1 Carbon precursor

The lychee peels were collected from lychee fruit purchased from a local supermarket, Singapore. Reddish coloured fine lychee peel powder (LP) was obtained following the procedures described in Section 3.1 (Chapter 3). The sample powder was collected in clean dry bottles, and stored in desiccators until used.

7.2.2 Synthesis of porous activated carbon

The LP was charred to get LP derived char (LPC), and porous AC was synthesized impregnating LPC with KOH (LPC:KOH = 1:2) following the procedures described in Section 3.6, Chapter 3. The resultant product was designated as LP-AC, collected in clean dry bottles and stored in desiccators for further studies.

7.2.3 Synthesis of Gr/PANI

Firstly, 50 mg of graphene oxide (GO) was dispersed in 100 mL of Milli-Q water by ultra-sonication. The given aniline monomer was distilled under reduced pressure prior to its use. Aniline monomer was dispersed in the pre-prepared GO solution and then sonicated for 1 h to obtain homogeneous adsorption of aniline monomer onto the surface of GO. Besides, 1 M HCl solution (20 mL) was prepared to contain 10 mmol of ammonium persulfate (APS), and this solution was slowly added to the GO/aniline mixture previously prepared. The mixture was stored at 0-5 °C for allowing the polymerization of aniline monomer followed by stirring for 12 h. The resulting powder was first filtered, and then washed with 1 M HCl, water and ethanol sequentially to obtain the colorless filtrate. The powder obtained was kept at 60 °C under vacuum for 12 h.

7.2.4 Material characterization

The LP-AC was analyzed for the elemental composition, physico-chemical, textural and morphological (microstructure) properties. The tests performed were elemental analysis, proximate analysis, thermogravimetric analysis (TGA), field emission-scanning electron microscopy (FE-SEM), X-ray diffraction (XRD), Raman

spectroscopy, Fourier transformer infrared (FT-IR) spectroscopy and X-ray photoelectron spectroscopy (XPS) following the procedures described in relevant sections in Chapter 3. The surface area of LP-AC was obtained from the BET method with the adsorption in the relative pressure (P/P_o) of 0.13. The total pore volume (V_T) was derived from the amount of Nitrogen adsorbed at a relative pressure of 0.99. The micropore volume (V_{micro}) and micropore surface area (S_{micro}) were obtained from t-plot method with a relative pressure of 0.15-0.5. The PSD was measured from the desorption points using DFT pore size distribution.

The carbonization behavior of LP and LPC impregnated with KOH was studied using Simultaneous TG-DTA/DSC Apparatus (Model: STA449 F3 Jupiter) under Nitrogen flow of 60 mL min^{-1}. The weight loss (TG) of both samples was recorded under the same dynamic-isothermal settings with a temperature of 50-950 °C at 20 K min^{-1} heating rate. The experiments were performed by loading approximately 10 mg of the samples on the same TG pan.

7.2.5 Electrochemical measurements

The electrodes for symmetric cell tests were made by mixing LP-AC (85 wt%), carbon black (10 wt% and PVDF (5 wt%). The mixture was ground in an agate mortar, a measured amount of N-Methyl-2-pyrrolidone (NMP) solution was added and mixed thoroughly to form homogenous slurry. The slurry was coated on the toray carbon paper in 1 cm^2 area, and then placed in vacuum oven at 60 °C for overnight. The total weight of the each electrode mass is about 3 mg cm^{-2}. Similarly, for asymmetric cell test, the electrodes were fabricated with loading of about 3.2 mg cm^{-2} of Gr/PANI for positive electrode and about 7 mg cm^{-2} of LP-AC for negative electrode. Cyclic voltammetry (CV) measurements of symmetric (LP-AC||LP-AC) as well as asymmetric (Gr/PANI||LP-AC) assemblies were carried out at room temperature condition in 1 M H_2SO_4 solution between the sweep potential of 0-0.8 V and 0-1.6 V, respectively at various sweep rates of 10-100 mV s^{-1} for both systems. Galvanostatic charge-discharge (GCD) and Electrochemical impedance spectroscopy (EIS) measurements were carried out for

both symmetric and asymmetric assemblies. Electrochemical measurements were performed with Solartron, 1470E electrochemical workstation.

The specific capacitances (C_{sp}) of symmetric and asymmetric assemblies were obtained from the equation below:

$$C_{sp} = I \times \Delta t / m \times \Delta V$$

where:

C_{sp} is the specific capacitance (F g^{-1}), I is the current (A), Δt is the discharge time (s), m (g) is the total mass of active material of the electrodes (g), and ΔV is the discharge voltage range (V).

In an asymmetric supercapacitor, the balance of the charge flow between the positive and the negative electrodes is necessary for optimum performance (i.e., $q^{+}=q^{-}$). The charge stored by each electrode depends on its specific capacitance (C_{sp}), the potential range of the charge-discharge process (ΔV) and the mass of the electrode (m). The mass ratio between the positive and negative electrodes in order to obtain equal charge flow ($q^{+}=q^{-}$) can be obtained from the equation below:

$$m^{-}/m^{+} = (C^{+} X \Delta V^{+})/(C^{-} X \Delta V^{-})$$

where:

m^{-}, m^{+}, C^{-}, C+, ΔV^{-} and ΔV^{+} are mass, a real or specific capacitance and potential range of positive and negative electrode obtained from the three electrode system.

The gravimetric specific capacitance is obtained from:

$$C = 4 \text{ x } (I \text{ x } \Delta t / m_{tot} \text{ x } \Delta V)$$

where:

I (A) is the current, Δt (s) is the discharge time, m_{tot} (g) is the total mass of the two electrodes, and ΔV (V) is the discharge voltage range. In present study, 1:2 ratio of both electrode mass loading was used;

The specific energy is calculated from the equation below:

$E = 1/2\ C(\Delta V)^2\ (1/3600)$

where:

C is the gravimetric specific capacitance and V is the maximum potential (1.6 V) applied in this work.

The power density (PD) is calculated from the equation below:

$P = E/\Delta t$ X 3600

where:

E is specific energy and Δt is the discharge time.

7.3 Results and Discussion

7.3.1 Elemental composition and proximate results

The elemental analysis results show high carbon content in lychee peel (LP), and the carbon content increased from 43.5% in LP to 67.4% in LP-AC (Table 7.1). The proximate analysis of LP showed the moisture content of 13.0%, VM of 83.3%, ash of 3.7% and FC of 13.0%. The high VM and low ash contents of LP suggest that the precursor material as biomass is suitable for its conversion into AC for further applications.

Table 7.1 Elemental composition of LP and LP-AC (wt%).

Sample	C%	H%	N%	S%	O%[a)]
LP	43.5	6.1	1.1	0.3	49.0
LP-AC	67.4	3.0	0.3	0.3	29.0

[a)]Estimated by difference

7.3.2 Combustion behavior

Thermogravimetric analysis (TGA) was carried out to know combustion behavior of LP and LPC impregnated with KOH (melting point of KOH = 360 °C) in weight

ratio of LPC:KOH = 1:2. The pyrolysis profile of LP exhibited a gradual weight loss up to ~150°C, which could be attributed to moisture release (Figure 7.1a). A significant mass loss is observed above 150 to 368°C (~53% by weight) which could be due to the release of volatiles. There is a gradual weight loss from 368 to

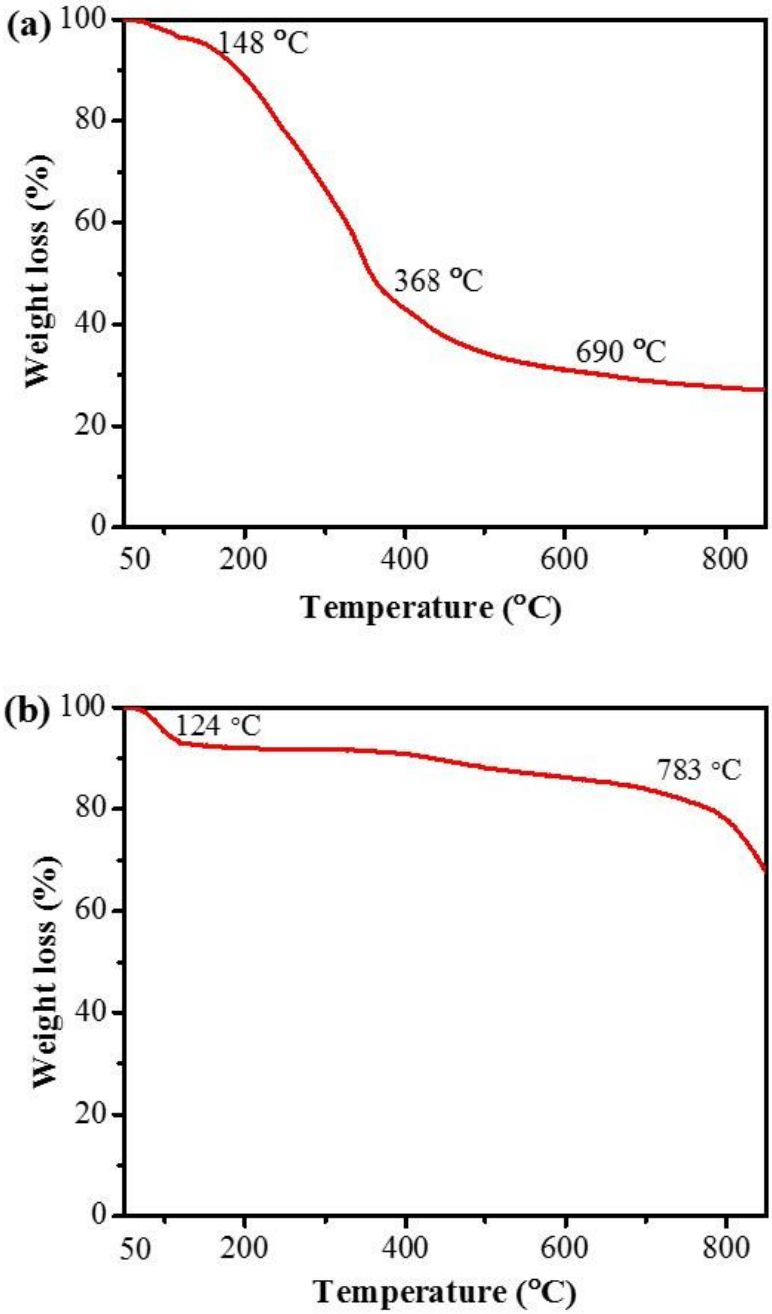

Figure 7.1. TGA curves: LP (a), and LPC impregnated with KOH (b).

700°C, and weight loss above 700 °C is minimal. The weight loss above 800 °C loss is observed negligible. Figure 7.1b illustrates TGA profile of LPC impregnated with KOH. There is a considerable weight loss up to ~124 °C (~7% by weight), which could be ascribed to moisture loss. A gradual weight loss occurred above 124 to ~783 °C (~20% by weight) may be due to the release of remaining organic or volatile matters. However, a sharp weight loss occurred afterwards, which could be due to decomposition of KOH and more gases release. The overall weight loss of LP is ~74.0%, whereas it is ~68.0% for LPC impregnated with KOH, which is expected since LPC is charred product of LP. It is clearly seen that the impregnation of LPC with KOH increased heat stability of the precursor.

7.3.3 Nitrogen adsorption-desorption studies

Figure 7.2a presents the nitrogen adsorption-desorption isotherms of LP-AC, which shows an association of type I and IV isotherms with a combination of both micro- and mesopores [196]. The existence of dominant micropores in the sample is obvious from the Nitrogen adsorption at very low relative pressure as well as the pore size distribution (PSD) curve with a large fraction of pores centered at pore width below 2 nm (Figure 7.2b). The BET surface area, micropore surface area (S_{micro}) and mesopore surface area are calculated to be 1601, 1436 and 165 $m^2\ g^{-1}$, respectively. The total pore volume is 0.86 $cm^3\ g^{-1}$ with micropore volume (V_{micro}) of 0.60 $cm^3\ g^{-1}$. The porous structure and the formation of some large pores in the sample is described in previous section.

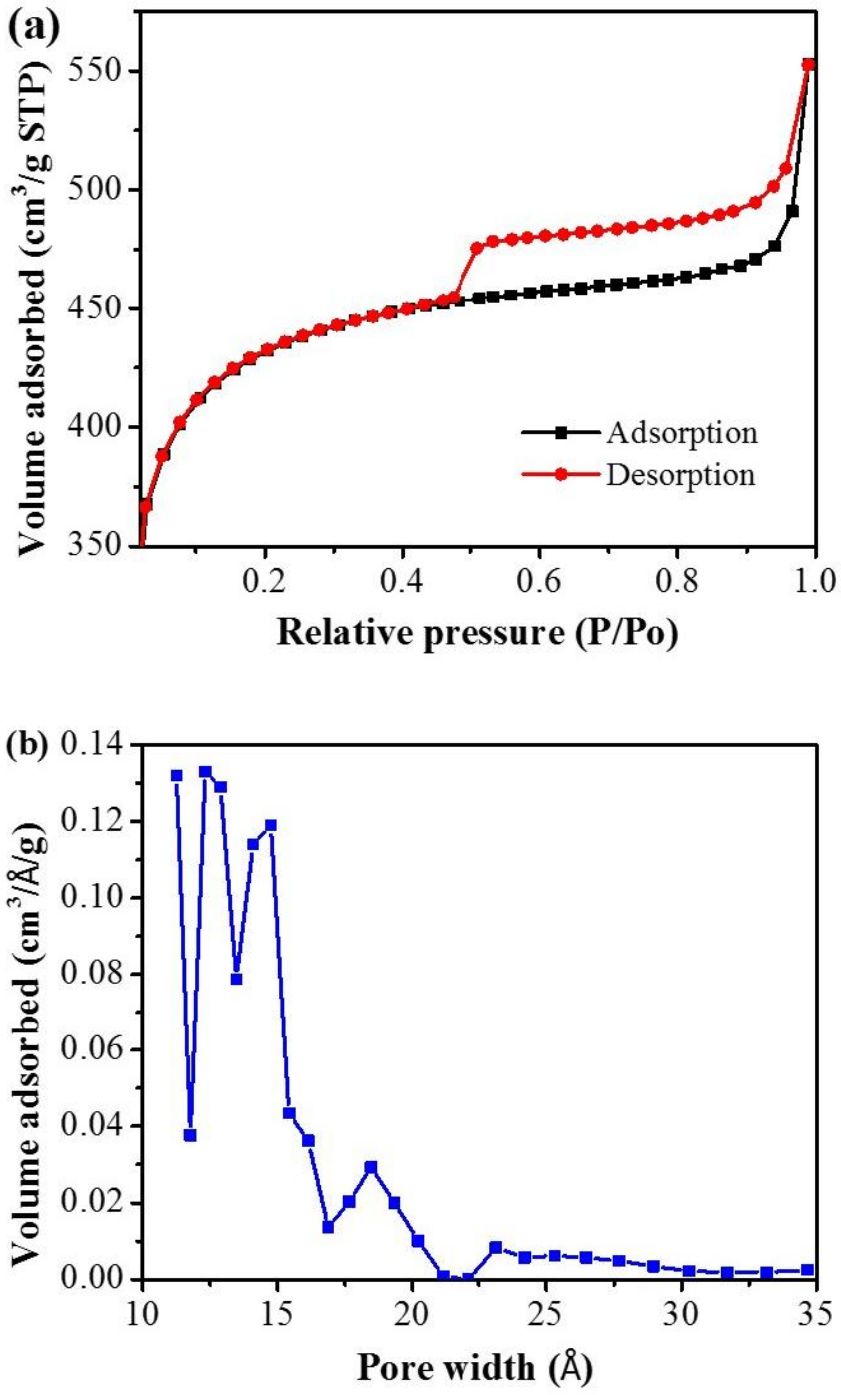

Figure 7.2. Nitrogen adsorption-desorption isotherms (a), and Pore width distribution (b) of LP-AC.

7.3.4 Morphological characterization

The surface morphology of the LP-AC was examined by the electron micrographs using field emission - scanning electron microscopy (FESEM, JEOL-7600F) operated at 5kV. FESEM 7600F equipped with electron disruptive X-ray spectroscope (EDX, Oxford Xmax80 LN_2 Free) was used for elemental mappings of the samples. FE-SEM images of the LP-AC with different magnifications with pores of varied size are provided in Figure 7.3a and b. High surface area AC with porous network provides more active sites for the electrical double layer formation and allows smooth diffusion of ions, which contribute in high specific capacitance of the electrode. Figure 7.4a illustrates the EDX spectrum of LP-AC, and Figure 7.4b and c show mapping spectra of carbon and oxygen. The mapping spectra clearly display the existence of C and O rich phase in the LP-AC.

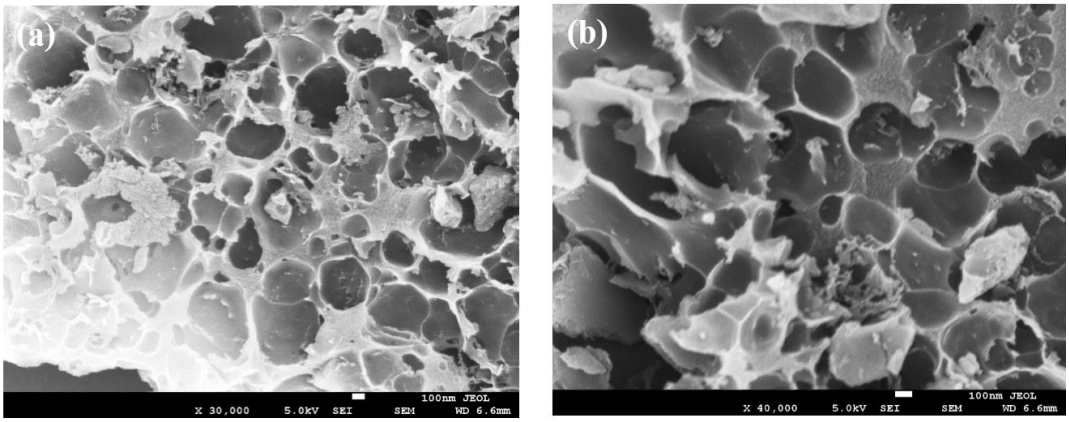

Figure 7.3. FE-SEM images at different magnifications: 30000 (100 nm) and 40000 (100 nm) of LP-AC.

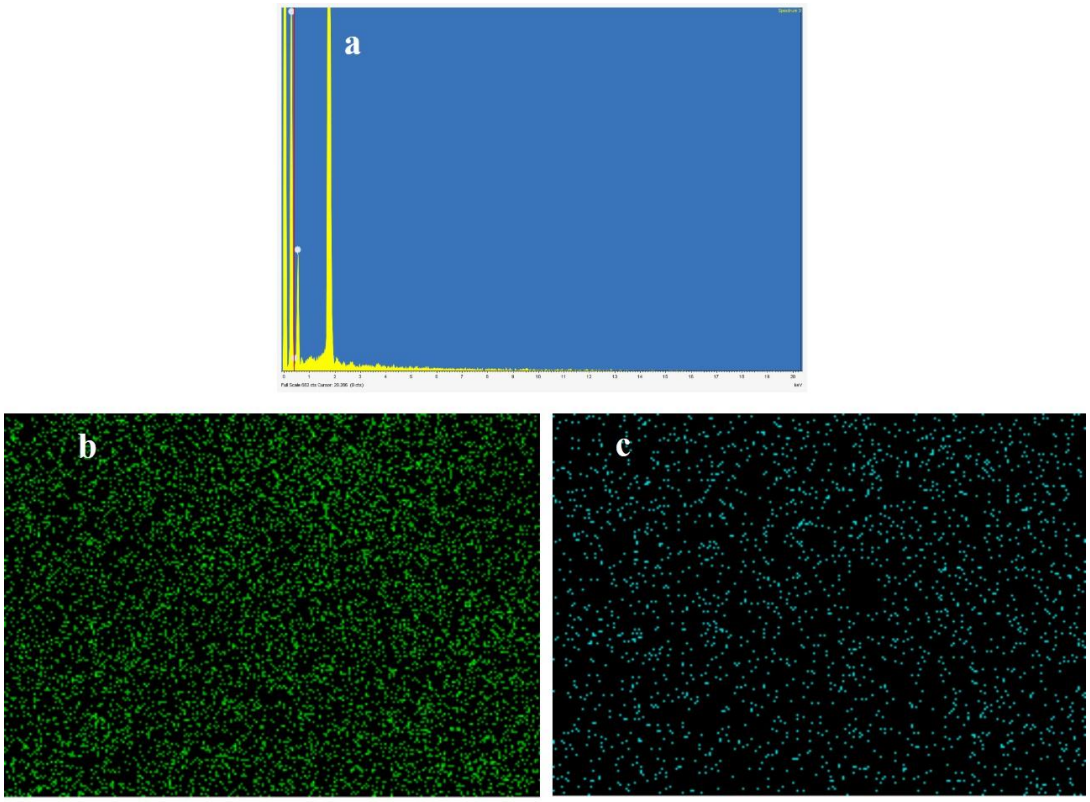

Figure 7.4. EDX spectrum (a), and mapping spectra of carbon (b), and mapping spectra of oxygen (c) of LP-AC.

7.3.5 Structural properties

The X-ray diffraction (XRD) pattern of LP-AC is illustrated in Figure 7.5a. The observed characteristic reflections at 2θ values of 29° and 43° correspond to the (002) and (110) planes of the graphite structure, respectively. The observed disorder effects indicate amorphous semi-graphitic carbons [166]. Further, the crystallographic structure of carbon of LP-AC was studied using Raman spectroscopy. In the graphitic materials, D band is corresponding to the disordered, edges and defects mediated zone-edge (near K-point) phonons and G band is associated to the E_{2g} phonon of C sp^2 atoms [198]. Figure 7.5b presents the Raman spectrum of LP-AC. The characteristic reflection observed at ~1370 cm^{-1} corresponds to D band, whereas the reflection at ~1610 cm^{-1} is the G band. The ratio of the intensities of D and G bands (I_D/I_G) is a measure of defects in the

carbonaceous materials, and is calculated to be 0.99 which infers predominant sp^2 type carbon in LP-AC.

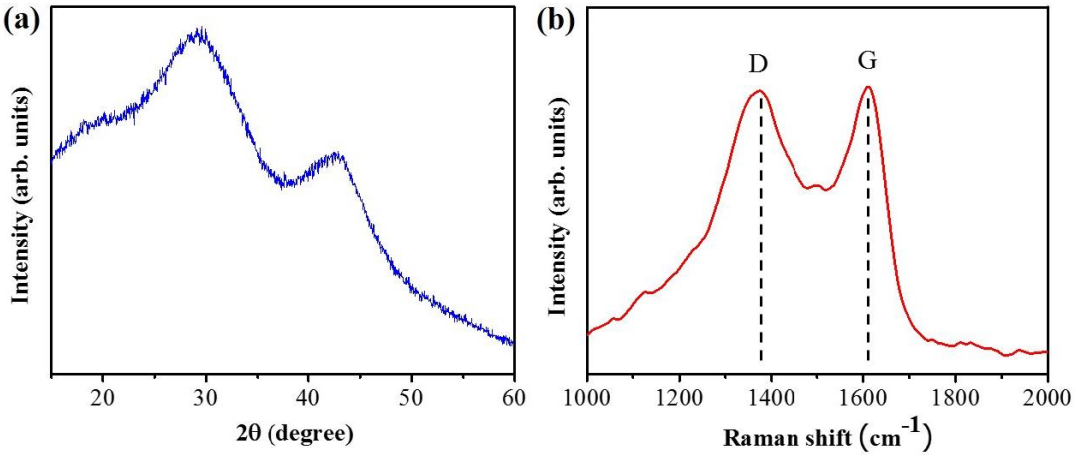

Figure 7.5. X-ray diffraction pattern (a), and Raman spectrum (b) of LP-AC.

7.3.6 Surface chemistry

In order to obtain quantitative information on surface functional groups of LP-AC, X-ray photoelectron spectroscopy (XPS) analysis was carried out. XPS survey spectrum of LP-AC shows the presence of different functional groups on its surface (Figure 7.6a). The high resolution de-convoluted C 1s spectra display well resolved peaks corresponding to carbon atoms in various chemical environments (Figure 7.6b). The characteristics binding energies positioned around 284.6, 286.1, and 288.5 eV correspond to sp^2 graphitic C, C-O and C=O, respectively [169, 170]. In the sample, the existence of a well-resolved peak with binding energy of 283.1 eV is observed. The functional groups obtained from curve fitting of C 1s XPS spectra are 58.3, 16.8, 12.8 and 12.1% for the peaks centered at binding energies of 284.6, 286.1, 283.1, and 288.5 eV, respectively. According to the previously reported findings, the presence of a small amount of oxygen-containing functional groups in carbonaceous materials enhances electrode performances and provides the long-term cycling stability [206].

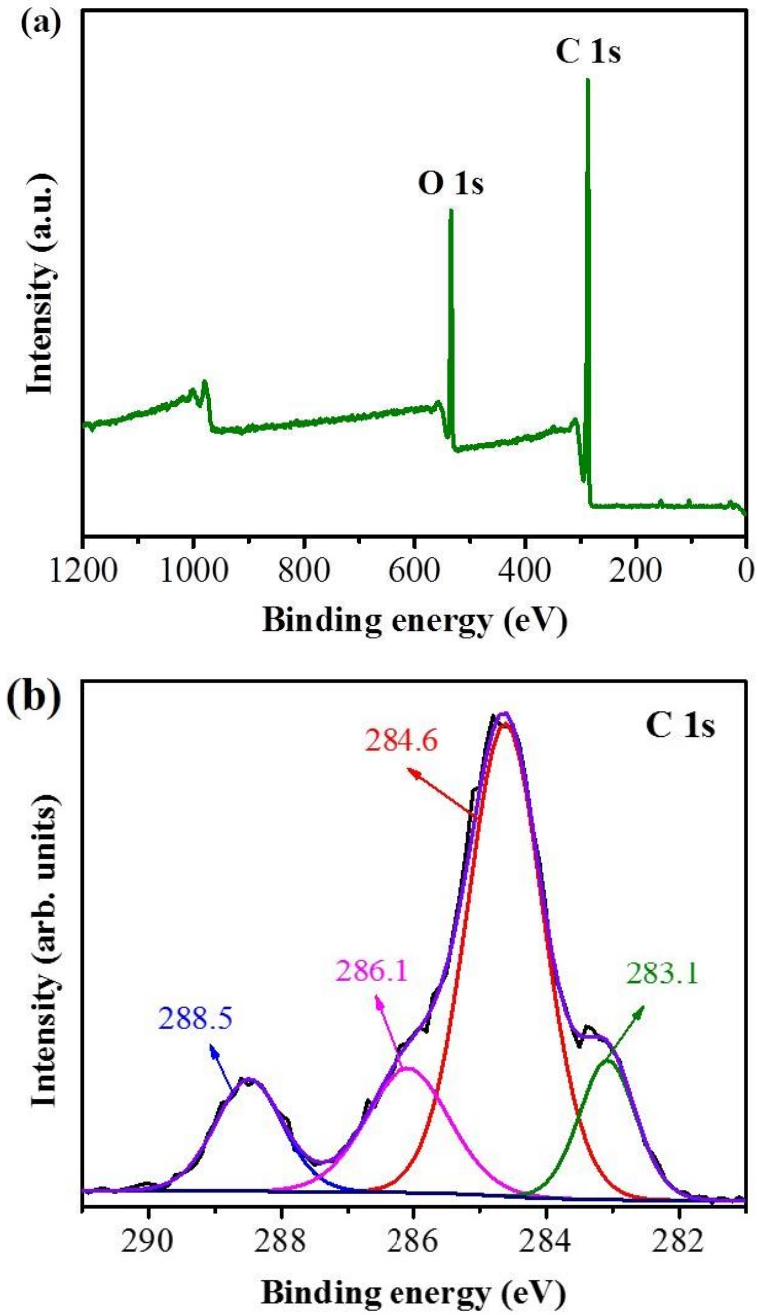

Figure 7.6. XPS survey spectrum (a), and XPS spectra of C 1s (b) of LP-AC.

The presence of surface functional groups in LP-AC was further corroborated from Fourier transformer infrared (FT-IR) spectra analysis. The presence of different functional groups on the sample surface can be clearly seen in the obtained FT-IR spectra (Figure 7.7). The signals observed in LP and LP-AC

correspond to stretching vibrations of alcohols or phenolic groups (O-H bend/stretch), saturated hydrocarbons, ethers, lipids or carbonates as given in Section 4.5.4.1, Chapter 4. The peaks observed also correspond to the stretching vibrations of lactones, quinones or carboxylic acids (COOH).

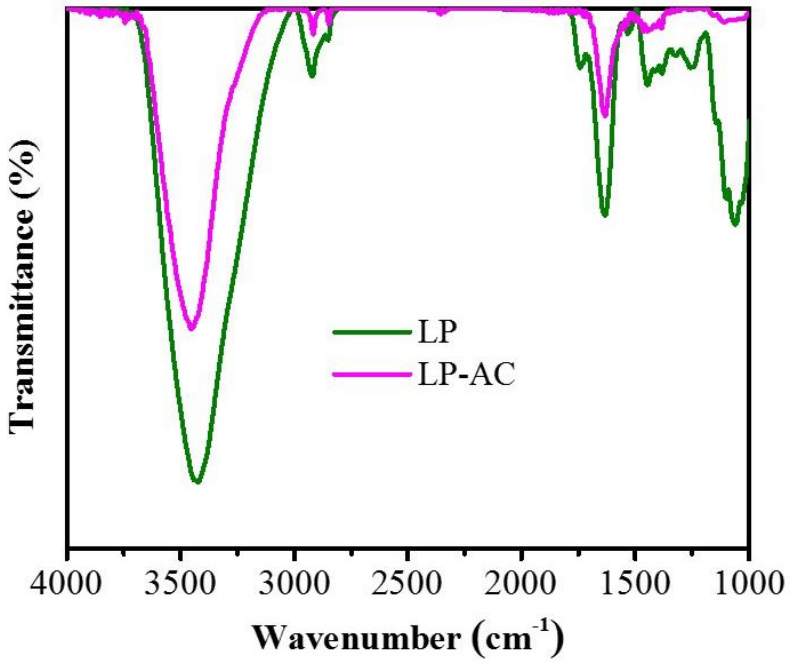

Figure 7.7. FT-IR spectra of LP and LP-AC.

7.4 Electrochemical properties

The LP-AC was evaluated as electrode for electric double layer capacitor (EDLC) using symmetric cell assembly (LP-AC||LP-AC). The CV curves for the symmetric capacitors were examined in 1 M H_2SO_4 aqueous electrolyte in the potential range of 0 to 0.8 V at various scan rates from 10-100 mV s^{-1} and the results are given in Figure 7.8a. The obtained quasi-rectangular shaped curves infer to the double-layer formation and good capacitive behavior of LP-AC. It is clearly seen that the CV curves are well preserved even at higher scan rate of 100 mV s^{-1}, indicating a fast CV response towards quick potential sweep and excellent rate capability. Figure 7.8b presents the GCD curves of LP-AC in the voltage window of 0 to 0.8 V at current densities of 0.25 to 5.0 A g^{-1}. It is apparent that the potential drop, usually

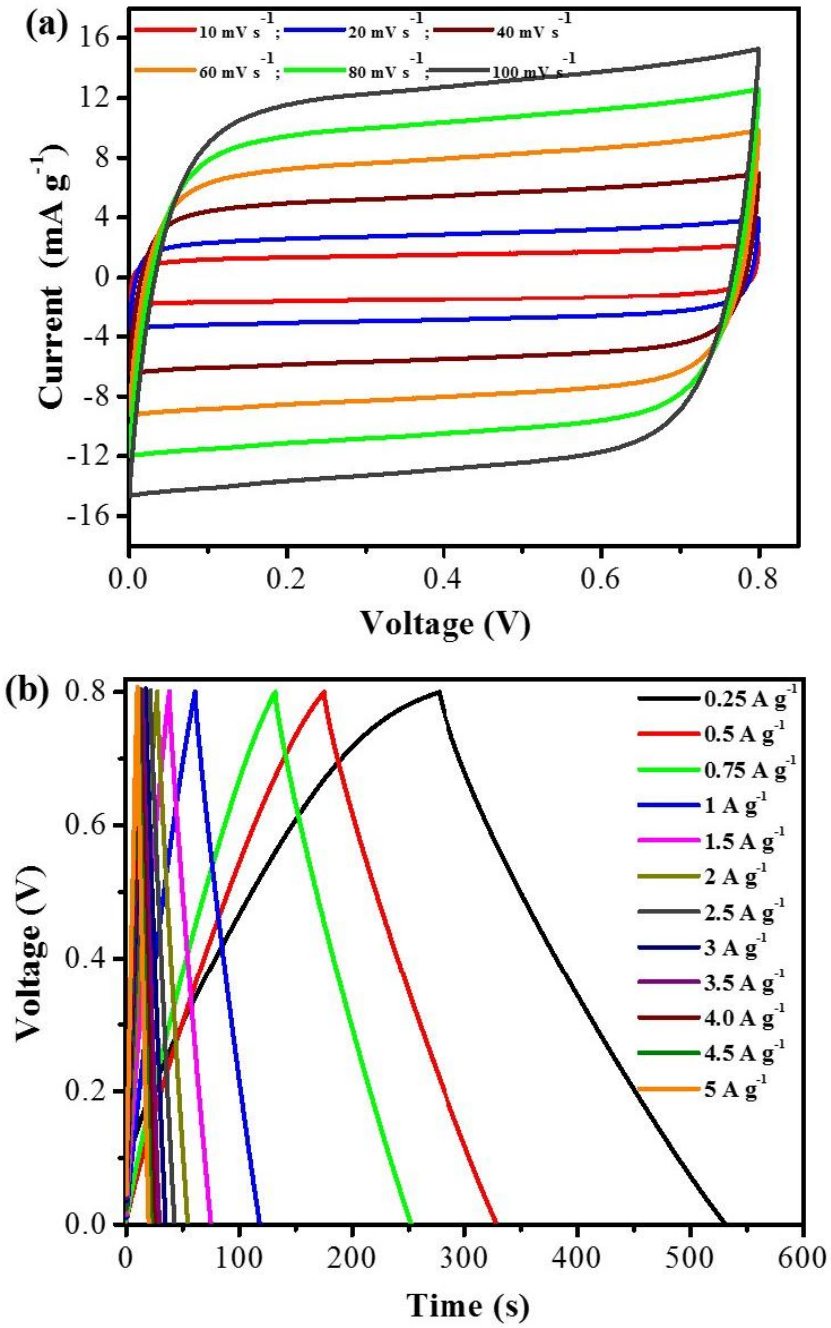

Figure 7.8. CV curves (a), and GCD curves (b) of the symmetric cell configuration (LP-AC||LP-AC) in 1 M H_2SO_4 electrolyte.

caused by the internal resistance of the assembly, is very low. The cell delivered a specific capacitance of 105 F g^{-1} at a current density of 0.25 A g^{-1}. The capacitance drops as scan rate or current density increases, which is ascribed to the rate-limited

diffusion of electrolyte ions into the electrode. The specific capacitance of 67.5 F g^{-1} is calculated at current density of 5 A g^{-1}, which is 64.2% retention compared to the capacitance at 0.25 A g^{-1}. The charge-discharge curves at different current densities are not completely symmetrical due to kinetic irreversibility of the ions on the electrode. During the test, at low current densities, the ions have enough time to intercalate and de-intercalate. This makes the ions able to access both the outer surface and inner pores. On the other hand, at high current densities, the ions are able to reach only at the outer surface of the electrode, which results in decrease of specific capacitance due to the reduced diffusion time.

In order to find the specific capacitance of the Gr/PANI composite electrode, the electrode was tested in 1 M H_2SO_4 at a potential window of 0 to 1 V (Figure 7.9a). The obtained CV curve shows the oxidation and reduction peaks which indicate the pseudo-capacitive behavior of the polymer. The specific capacitance of the polymer composite was evaluated from the GCD curves. Figure 7.9b shows the GCD curves of Gr/PANI composite. This composite electrode delivered a specific capacitance of 190 F g^{-1} at 1 A g^{-1}. Thus, based on the specific capacitive behavior of both electrodes, the asymmetric supercapacitor was

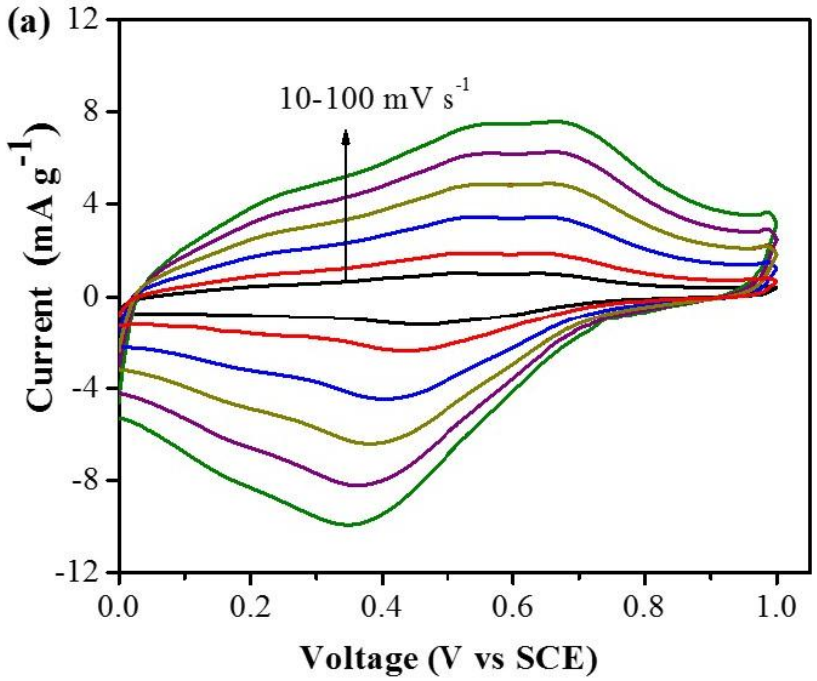

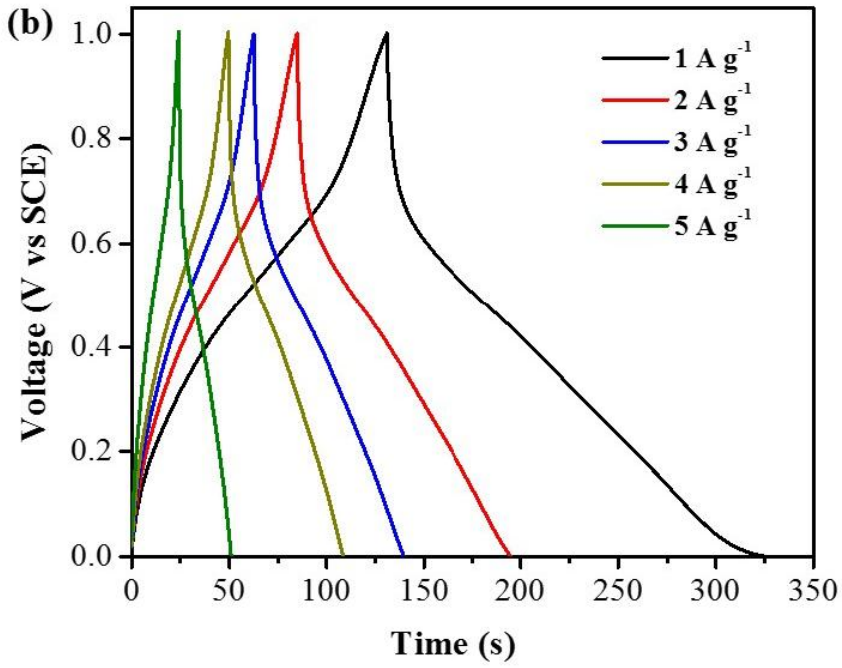

Figure 7.9. CV curves (a), and GCD curves (b) of the Gr/PANI composite electrode tested in 1 M H_2SO_4 electrolyte.

fabricated and evaluated by using the synthesized LP-AC and Gr/PANI as negative and positive electrodes, respectively.

In the hybrid capacitors, the voltage window of the cell was increased to 1.6 V. There was a large inconsistence in the performances between two electrodes, hence, it is necessary to balance the mass of the electrode with respect to the other in order to ensure the efficient utilization of each electrode and optimal cycling stability. Figure 7.10a illustrates the CV curves of the asymmetric supercapacitor at sweep rate of 10 to 100 mV s^{-1} in the potential range of 0.0 to 1.6 V in 1 M H_2SO_4 solution. The shape of CV profiles exhibit the combined contribution of both the electric double-layer and pseudo-capacitance properties of the cell. The increasing current with respect to the scan rate trend implies the quick rate capability of the asymmetric capacitor. Figure 7.10b displays the GCD curves at various current densities. The nearly symmetric shape of charge-discharge curves indicates good reversible electrochemical reactions. It is noted that the asymmetric cell delivered a

specific capacitance of ~141.0 F g^{-1} at a current density of 0.5 A g^{-1}. Here, both electrode mass has been included in the capacitance calculation.

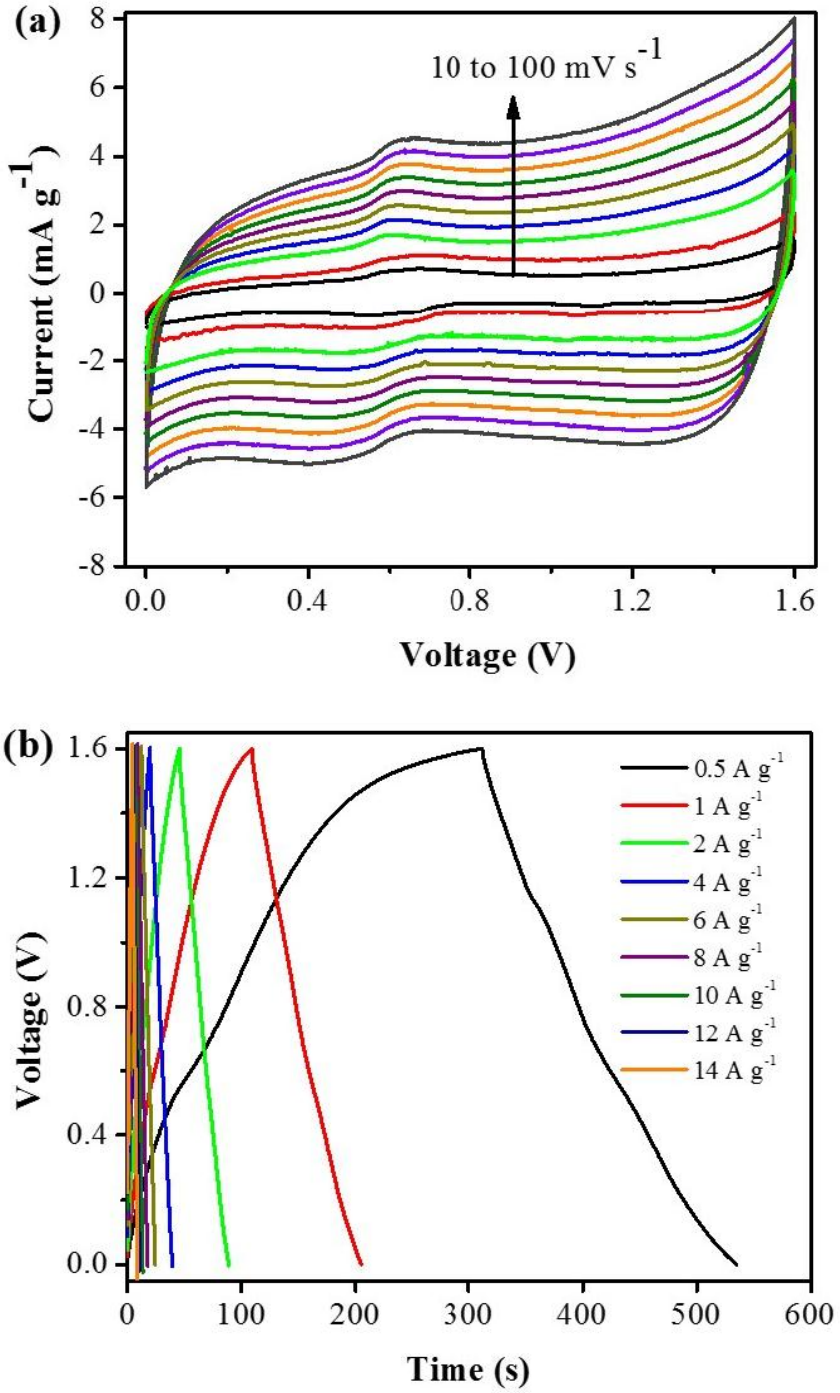

Figure 7.10. CV curves (a), and GCD curves (b) of the Gr/PANI||LP-AC asymmetric supercapacitor.

Figure 7.11 illustrates the Ragone plot of the symmetric and asymmetric supercapacitors tested. For the symmetric supercapacitor, specific energy of 9.4 Wh kg^{-1} is achieved, whilst the asymmetric assembly delivered much higher specific energy of ~50.0 Wh kg^{-1}. In this study, this higher specific energy achieved for asymmetric assembly could be attributed to pseudo-capacitive mechanism of redox active material in addition to interfacial double-layer mechanism of the as-synthesized high surface area LP-AC.

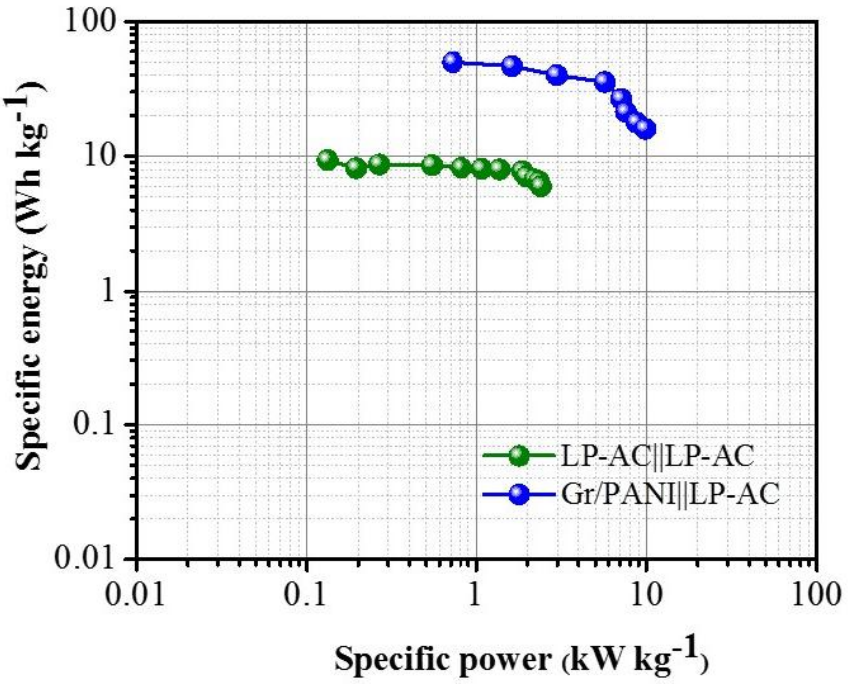

Figure 7.11. Ragone plot of the symmetric (LP-AC||LP-AC) and asymmetric (Gr/PANI||LP-AC) cells.

Figure 7.12 shows the comparative capacitance retention from cycling studies for the symmetric and asymmetric supercapacitors at current rate of 2 A g^{-1}. The charge-discharge curves of both devices maintained nearly symmetric shape, indicating a good reversible electrochemical activity. Both the devices exhibited good cycling stability with capacitance retention above 80% after 5000 cycles. Earlier studies on asymmetric supercapacitors employing bio-waste based AC and

PANI or Gr/PANI||AC is scarce [231]. Table 7.2 shows electrochemical performance some previous studies on the commercial AC||PANI combination and results of the present study. It can be seen that the asymmetric cell using LP-AC and Gr/PANI composite as negative and positive electrodes in present study exhibited better electrochemical performances.

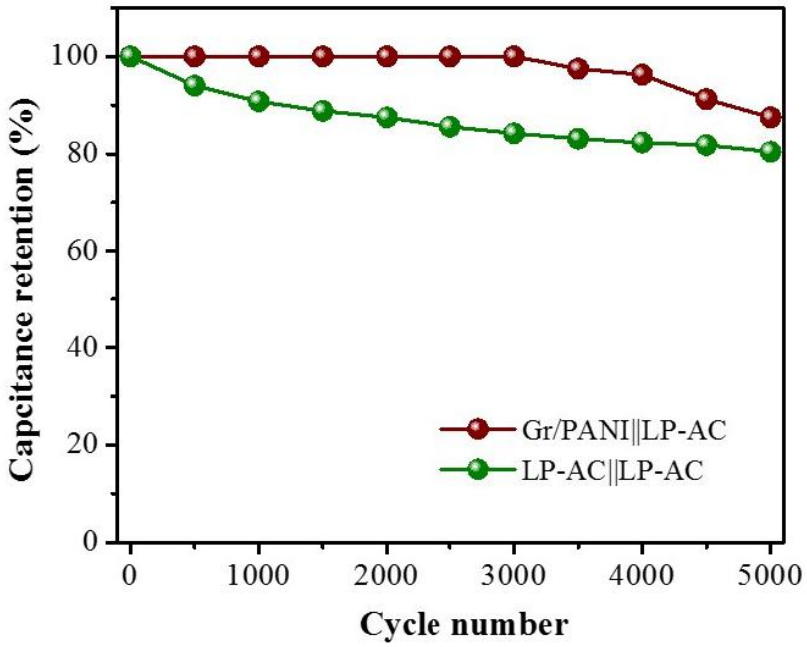

Figure 7.12. Comparative cycling stability of symmetric (LP-AC||LP-AC) and asymmetric (Gr/PANI||LP-AC) cells.

Figure 7.13 illustrates the Nyquist plots obtained from EIS studies for the symmetric and asymmetric supercapacitors, and Gr/PANI vs. SCE. The internal resistance of the electrodes caused by electrolyte and current collectors at the high frequency is smaller for Gr/PANI||LP-AC (~1.0 Ω) than Gr/PANI and LP-AC||LP-AC (~2.5 Ω). The smaller this value, the electrode performs better due to the efficient access of electrolyte ions to the surface and shortened ion diffusion path. The slope of the 45° portion of the curve which is called as the Warburg resistance results from the frequency dependence of ion diffusion /transport in the electrolyte/electrode interface. The vertical curves demonstrate a nearly ideal capacitive behavior. Further, the exceeding 45° inclined angle and the vertical lines

at low frequency close to 90° suggest a pure capacitive behavior and low diffusion resistance of ions in the electrodes [220]. This facilitates the diffusion of electrolyte ions into the electrode and results in facile and reversible redox reactions.

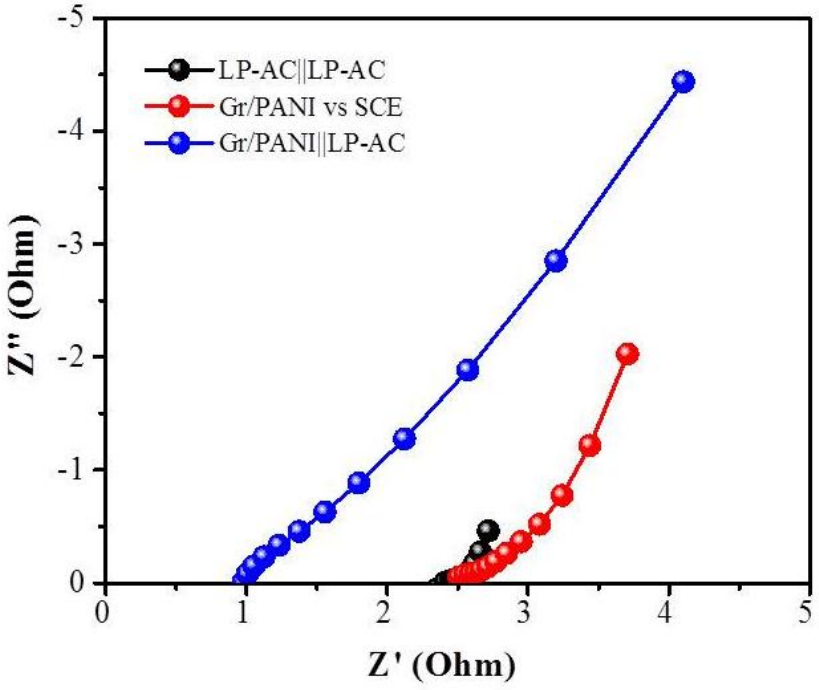

Figure 7.13. Nyquist plots for the symmetric and asymmetric supercapacitors, and Gr/PANI vs. SCE.

To sum up, Lychee peels waste derived porous carbon (LP-AC) with BET surface area of 1601 m^2 g^{-1} was evaluated for the energy storage applications. *For the first time, LP-AC was evaluated as electrode for supercapacitors in both symmetric and asymmetric cell configurations in aqueous electrolyte.* The assembled symmetric cell configuration (Gr/PANI||LP-AC) delivered high specific energy of about 9.4 Wh kg^{-1}. The specific energy was further increased to ~50.0 Wh kg^{-1} in an asymmetric cell assembly in which Gr/PANI composite and LP-AC were used as positive and negative electrodes, respectively. The asymmetric cell exhibited good cycling stability with the initial capacitance retention above 80.0% after 5000 cycles.

Table 7.2. Electrochemical performance of PANI/AC configurations in aqueous electrolyte.

Electrode	Electrolyte	Surface area[#] ($m^2 g^{-1}$)	Current	Potential (V)	Specific capacitance ($F g^{-1}$)	Cycling stability	Energy ($Wh kg^{-1}$)	Reference
PANI/AC (composite)	1 M H_2SO_4	1778	1 mA	0-0.6	180	~1000 (91%)	-	[224]
PANI/AC (composite)	1 M H_2SO_4	875-2312	1.27 mA	0-0.8	~70	300 (97%)	-	[227]
PANI/AC (composite)	0.5 M H_2SO_4	-	1 A	-0.2-0.7	382	50 (97%)	-	[228]
PANI/AC (composite)	1 M H_2SO_4	-	1 A	0-0.8	238	600 (86%)	-	[229]
PANI/Graphite	6 M H_2SO_4	-	1 A	0-0.8	2136	1000 (91%)	24	[232]
AC/PANI	1 M H_2SO_4	702	0.5 A	-0.2-0.7	244	1000 (92%)	47.5	[233]
PANI||AC (hybrid)	6 M KOH	-	0.5-20 mA	1-1.6	380	4000 (80%)	18	[230]
Gr/PANI||LP-AC (asymmetric)	1 M H_2SO_4	1601	0.5 A	0-1.6	~141	5000 (81%)	~50	This study

7.4 Conclusion

Lychee peel waste was utilized as a novel alternative precursor for synthesis of high surface area activated carbon (LP-AC) via chemical activation, and the as-prepared LP-AC was evaluated as electrode material for symmetric (LP-AC||LP-AC) and asymmetric (Gr/PANI||LP-AC) assemblies in aqueous electrolyte. The specific capacitance value of 105 F g^{-1} and specific energy of 9.4 Wh kg^{-1} of symmetric cell are increased to ~141.0 F g^{-1} and ~50.0 Wh kg^{-1} with asymmetric supercapacitor fabricated using Gr/PANI as cathode and LP-AC as anode. Furthermore, the asymmetric cell also displays good cycling stability with capacitance retention above 80.0% after 5000 cycles. The efficient charge storage behavior of the LP-AC as a promising electrode opens up the possibility of utilizing low-cost, sustainable and environmentally-friendly bio-waste for the fabrication of high-performance supercapacitors.

CHAPTER 8

Conclusions and Recommendations

8.1 Overall conclusions

The intensive research of the high surface area carbons synthesized from abundantly available orange peels waste showed OP-AC and OP-AC1 to be promising electrodes for VRB applications. BET analysis revealed that the synthesized OP-AC and OP-AC1 are mostly microporous with high surface area of 1901 m^2 g^{-1} and 1916 m^2 g^{-1}, respectively. The dominant micropores in the synthesized ACs might have been formed due to KOH used as activating agent. CV results showed improved electrocatalytic activity in both positive and negative side redox couples for the OP-AC and OP-AC1 modified electrodes compared with the pristine electrode. The oxygen-containing functional groups present on the surface of the ACs further contributed in facilitating charge transfer during redox reactions. The impedance studies show reduced charge transfer resistance for the ACs modified electrodes, indicating better contacts between porous felt and electrode plates. Consequently, the VRB performance in a static cell shows higher voltage and energy efficiencies for OP-AC electrode than the pristine electrode at all current densities tested. The improved electrocatalytic activity of the ACs can be attributed to the synergistic effect of high surface area and the presence of rich oxygen-containing functional groups.

Further, the additional study performed by using surface modified OP-AC1 (T-OP-AC) exhibited better electrochemical kinetics of the redox reactions in the order of T-OP-AC > OP-AC1 > graphite. The findings indicate that the rich oxygen functionalities facilitate the charge transfer processes by providing more active sites for the redox reactions and improving the wettability of the electrode. Hence, the electrochemical performance of the as-synthesized AC as electrode for the VRB applications could be enhanced via a very simple surface modification. The results suggest the ACs to be a promising electrode for VRB applications. The OP-AC and

OP-AC1 synthesized from low cost bio-waste can be considered as potential precursors to produce conducting plastics electrode to lower the VRB stack cell weight and overall cost.

Additionally, the feasibility of using OP-AC as promising electrode towards the fabrication of high specific energy LICs was successfully demonstrated. The fabricated LIC using the OP-AC with pre-lithiated graphite (LiC_6) delivered specific energy of ~106 Wh kg^{-1}. Metal oxide based LIC (OP-AC||$Li_4Ti_5O_{12}$), symmetric supercapacitor with aqueous and organic solutions were also explored for comparison. A systematic improvement from the specific energy of ~8 to 106 Wh kg^{-1} was noted from aqueous to LIC assembly. The findings offer new opportunities to explore abundant, low cost, renewable biomass waste as potential carbon source for the development of high specific energy LICs.

The other porous carbon synthesized from lychee peel waste (LP-AC) with surface area of 1601 m^2 g^{-1} was evaluated as electrode for supercapacitors in symmetric (LP-AC||LP-AC) and asymmetric (Gr/PANI||LP-AC) cell configurations. Performance tests showed that the asymmetric cell assembly could deliver specific capacitance of ~141 F g^{-1} at 0.5 A g^{-1} and specific energy to ~50 Wh kg^{-1} as compared to the specific capacitance of 105 F g^{-1} at a current density of 0.25 A g^{-1} and specific energy of 9.4 Wh kg^{-1} for the symmetric cell configuration. The high specific capacitance and specific energy are attributed to the well-developed microporous structures to facilitate fast ions transport, while high surface area accommodate more ions in the electrode, which subsequently enhance its electrochemical performance. The asymmetric cell showed good cycling stability with the initial capacitance retention above 80% after 5000 cycles. The intriguing properties of LP-AC make it a promising alternative electrode material for the development of high-performance aqueous supercapacitors.

8.2 Recommendations

Based on the research works and findings of this study, some recommendations for future studies are made:

- **Optimization of activated carbon preparation**

  In the present study, high surface area ACs have been successfully synthesized from renewable low cost five fruit peels. The ACs are synthesized with the same processing conditions, i.e., sample char to KOH ratio of 1:2 (except for OP-AC1 with OPC:KOH = 1:1.5), activation temperature, activation duration, and inert gas flow rate. The activation variables are supposed to play important roles in the pore structure and textural characteristics of the resultant carbons. Thus, further study for optimization of activation conditions for AC preparation using any one of the present bio-waste samples (preferably orange peel waste) will provide useful additional data. In such future study, sample to KOH ratio, activation temperature and activation duration and gas flow rate should be varied in order to investigate influence of individual variables on the resultant ACs. This will provide the optimum processing conditions for the AC preparation with desired textural properties.

- **Synthesis of mesoporous carbons**

  All the ACs synthesized in the present study are predominantly microporous with pores having very narrow pore width. Such ACs with dominant microporosity might have limited the electrochemical performances due to the restriction in smooth movement of electrolyte ions in pores. KOH as an activating agent generally produces AC with high micropores, therefore, other chemicals, such as $ZnCl_2$ or other method should be employed for the preparation of mesoporous AC. The pore sizes of ACs have influence on the EDLC capacitances, and mesoporous ACs are expected to exhibit better performance, particularly for supercapacitors.

- **Synthesis of porous carbon retaining precursor oxygen**

  Carbons rich in high oxygen functionalities enhance electrochemical activity in VRB applications. The bio-waste samples contain high oxygen as revealed from ultimate analysis. If the carbon synthesis process that retains the original oxygen of the precursor materials can be employed, it will help increase the oxygen functionalities in the resultant carbon product. This will

help save the efforts and resources required for surface modification of the as-synthesized carbon.

- **Synthesis of porous carbon from mixed bio-waste and study feasibility for its applications**

  In present study, only pure sources of bio-waste fruit peels are used as precursors for ACs preparation. The present findings show bio-waste fruit peels are promising precursor materials for electrode material for energy storage applications. It will be interesting to investigate the textural properties of carbon products from mixed bio-waste (e.g., from juice producers), and study feasibility for application of the products.

- **Supplement with the solid state conductivity and surface wettability or carbon samples vis-à-vis graphite**

  In future studies, the relevant current findings should be supplemented with the solid state conductivity and surface wettability (contact angle data) or carbon samples vis-à-vis graphite in relevant works.

- **Testing using other electrolytes**

  Besides, electrode properties, the electrochemical performance of supercapacitors largely depend on the electrolyte used in the testing. In the present study, the electrochemical performances of electrodes are performed mostly in aqueous electrolyte. Supercapacitors tests using redox additive electrolytes should also be investigated to see the difference between capacitance or energy realized compared with the electrolytes used in this study. Further, tests using redox additives in organic electrolytes and adjustment of variables as required will be of interest.

- **Testing the electrode performance in G2 VRB**

  In this study, electrochemical measurements for VRB applications were performed using the first generation electrolyte (G1 VRB). Since the second generation cell (G2 VRB) is more promising in generating higher energy

density, future study should carry out experiments using G2 VRB which will provide comparative performance data for the bio-waste derived AC.

Furthermore, the VRB cell cycling test in flow cell will provide data for practical applications of the synthesized ACs as electrodes, and future study should consider this.

References

[1] I.I.G. Inal, S.M. Holmes, A. Banford, Z. Aktas, The performance of supercapacitor electrodes developed from chemically activated carbon produced from waste tea, Applied Surface Science 357, Part A (2015) 696-703.

[2] V. Sricharoenchaikul, C. Pechyen, D. Aht-ong, D. Atong, Preparation and Characterization of Activated Carbon from the Pyrolysis of Physic Nut (Jatropha curcas L.) Waste, Energy & Fuels 22(1) (2008) 31-37.

[3] Y. Li, X. Zhang, R. Yang, G. Li, C. Hu, The role of H3PO4 in the preparation of activated carbon from NaOH-treated rice husk residue, RSC Advances 5(41) (2015) 32626-32636.

[4] K. Le Van, T.T. Luong Thi, Activated carbon derived from rice husk by NaOH activation and its application in supercapacitor, Progress in Natural Science: Materials International 24(3) (2014) 191-198.

[5] J. Wang, S. Kaskel, KOH activation of carbon-based materials for energy storage, Journal of Materials Chemistry 22(45) (2012) 23710-23725.

[6] M. Ulaganathan, A. Jain, V. Aravindan, S. Jayaraman, W.C. Ling, T.M. Lim, M.P. Srinivasan, Q. Yan, S. Madhavi, Bio-mass derived mesoporous carbon as superior electrode in all vanadium redox flow battery with multicouple reactions, Journal of Power Sources 274 (2015) 846-850.

[7] W. Tang, Y. Zhang, Y. Zhong, T. Shen, X. Wang, X. Xia, J. Tu, Natural biomass-derived carbons for electrochemical energy storage, Materials Research Bulletin 88 (2017) 234-241.

[8] P. Sennu, V. Aravindan, Y.-S. Lee, High energy asymmetric supercapacitor with 1D@2D structured NiCo2O4@Co3O4 and jackfruit derived high surface area porous carbon, Journal of Power Sources 306 (2016) 248-257.

[9] M. Biswal, A. Banerjee, M. Deo, S. Ogale, From dead leaves to high energy density supercapacitors, Energy & Environmental Science 6(4) (2013) 1249-1259.

[10] Y. Guo, J. Qi, Y. Jiang, S. Yang, Z. Wang, H. Xu, Performance of electrical double layer capacitors with porous carbons derived from rice husk, Materials Chemistry and Physics 80(3) (2003) 704-709.

[11] S.T. Senthilkumar, B. Senthilkumar, S. Balaji, C. Sanjeeviraja, R. Kalai Selvan, Preparation of activated carbon from sorghum pith and its structural and electrochemical properties, Materials Research Bulletin 46(3) (2011) 413-419.

[12] X. Li, C. Han, X. Chen, C. Shi, Preparation and performance of straw based activated carbon for supercapacitor in non-aqueous electrolytes, Microporous and Mesoporous Materials 131(1–3) (2010) 303-309.

[13] A.E. Ismanto, S. Wang, F.E. Soetaredjo, S. Ismadji, Preparation of capacitor's electrode from cassava peel waste, Bioresource Technology 101(10) (2010) 3534-3540.

[14] L.A. Pfaltzgraff, M. De bruyn, E.C. Cooper, V. Budarin, J.H. Clark, Food waste biomass: a resource for high-value chemicals, Green Chemistry 15(2) (2013) 307-314.

[15] F. Cherubini, S. Bargigli, S. Ulgiati, Life cycle assessment (LCA) of waste management strategies: Landfilling, sorting plant and incineration, Energy 34(12) (2009) 2116-2123.

[16] M.-H. Kim, J.-W. Kim, Comparison through a LCA evaluation analysis of food waste disposal options from the perspective of global warming and resource recovery, Science of The Total Environment 408(19) (2010) 3998-4006.

[17] T.C. Chandra, M.M. Mirna, J. Sunarso, Y. Sudaryanto, S. Ismadji, Activated carbon from durian shell: Preparation and characterization, Journal of the Taiwan Institute of Chemical Engineers 40(4) (2009) 457-462.

[18] M.L. Perry, A.Z. Weber, Advanced Redox-Flow Batteries: A Perspective, Journal of the Electrochemical Society 163(1) (2016) A5064-A5067.

[19] A.Z. Weber, M.M. Mench, J.P. Meyers, P.N. Ross, J.T. Gostick, Q. Liu, Redox flow batteries: a review, Journal of Applied Electrochemistry 41(10) (2011) 1137.

[20] A. Parasuraman, T.M. Lim, C. Menictas, M. Skyllas-Kazacos, Review of material research and development for vanadium redox flow battery applications, Electrochimica Acta 101 (2013) 27-40.

[21] M. Ulaganathan, V. Aravindan, Q. Yan, S. Madhavi, M. Skyllas-Kazacos, T.M. Lim, Recent Advancements in All-Vanadium Redox Flow Batteries, Advanced Materials Interfaces 3(1) (2016) 1500309-n/a.

[22] M. Ulaganathan, V. Aravindan, Q. Yan, S. Madhavi, M. Skyllas-Kazacos, T.M. Lim, Recent Advancements in All-Vanadium Redox Flow Batteries, Advanced Materials Interfaces 3(1) (2016) n/a-n/a.

[23] https://energy.gildemeister.com/en. Accessed on 25 February 2018.

[24] http://proxhima.com/?page_id=818. Accessed on 25 February 2018.

[25] http://vanadiumbattery.com/index.php/profile/index/. Accessed on 25 February 2018.

[26] http://global-sei.com/company/outline.htm. Accessed on 25 February 2018.

[27] http://www.gec.com.cn/root/web/index.php. Accessed on 25 February 2018.

[28] https://openei.org/wiki/Prudent_Energy_Inc. Accessed on 25 February 2018.

[29] http://www.rongkepower.com. Accessed on 25 February 2018, .

[30] https://redtenergy.com/. Accessed on 25 February 2018.

[31] http://www.uetechnologies.com/. Accessed on 25 February 2018.

[32] https://h2aec.en.ec21.com/. Accessed on 25 February 2018.

[33] https://www.vsunenergy.com.au/. Accessed on 25 February 2018.

[34] V.J. L. Swette, Development of Electrodes for-the NASA Iron/Chromium Redox System and Factors Affecting Their Performance, http://ntrs.nasa.gov/archive/nasa/

casi.ntrs.nasa.gov/19850027158 1985027158.pdf (1984).

[35] P.G.P.A. R.J. Remick, Electrically rechargeable anionically active reduction–oxidation electrical storage-supply system, U.S. Patent 4,485,154 (1984).

[36] R.F. Savinell, C.C. Liu, R.T. Galasco, S.H. Chiang, J.F. Coetzee, Discharge Characteristics of a Soluble Iron-Titanium Battery System, Journal of The Electrochemical Society 126(3) (1979) 357-360.

[37] M. Skyllas-Kazacos, M.H. Chakrabarti, S.A. Hajimolana, F.S. Mjalli, M. Saleem, Progress in Flow Battery Research and Development, Journal of The Electrochemical Society 158(8) (2011) R55-R79.

[38] Li, B. Li, M. Gu, Z. Nie, X. Wei, C. Wang, V. Sprenkle, W. Wang, Nanorod Niobium Oxide as Powerful Catalysts for an All Vanadium Redox Flow Battery, Nano letters 14(1) (2014) 158-165.

[39] B. Sun, M. Skyllas-Kazacos, Modification of graphite electrode materials for vanadium redox flow battery application—I. Thermal treatment, Electrochimica Acta 37(7) (1992) 1253-1260.

[40] X. Rui, A. Parasuraman, W. Liu, D.H. Sim, H.H. Hng, Q. Yan, T.M. Lim, M. Skyllas-Kazacos, Functionalized single-walled carbon nanotubes with enhanced electrocatalytic activity for redox reactions in vanadium bromide redox flow batteries, Carbon 64 (2013) 464-471.

[41] S.M. Taylor, A. Pătru, D. Streich, M. El Kazzi, E. Fabbri, T.J. Schmidt, Vanadium (V) reduction reaction on modified glassy carbon electrodes – Role of oxygen functionalities and microstructure, Carbon 109 (2016) 472-478.

[42] A.K. Shukla, Electrochemical power sources, Resonance 6(8) (2001) 72-81.

[43] L.L. Zhang, X.S. Zhao, Carbon-based materials as supercapacitor electrodes, Chemical Society Reviews 38(9) (2009) 2520-2531.

[44] P.J. Hall, Epsrc, Energy-storage technologies and electricity generation, Energy Policy 36(12) (2008) 4352-4355.

[45] A. Nishino, Capacitors: operating principles, current market and technical trends, Journal of Power Sources 60(2) (1996) 137-147.

[46] D.C. Mahon PJ, Supercapacitors – nanostructured materials and nanoscale processes contributing to the next mobile generation, Aust. J. Chem. 54 (2001) 473-476.

[47] M. Conte, Supercapacitors Technical Requirements for New Applications, Fuel Cells 10(5) (2010) 806-818.

[48] R. Kötz, M. Carlen, Principles and applications of electrochemical capacitors, Electrochimica Acta 45(15–16) (2000) 2483-2498.

[49] A.G. Pandolfo, A.F. Hollenkamp, Carbon properties and their role in supercapacitors, Journal of Power Sources 157(1) (2006) 11-27.

[50] B.E. Conway, Electrochemical Supercapacitors—Scientific Fundamentals and Technological Applications, Kluwer, New York (1999).

[51] T.C.M. A.F. Burke, Materials for Electrochemical Energy Storage and Conversion—Batteries, Capacitors and Fuel Cells, Symposium, April 17–20, 1995, San Francisco, CA, Materials Research Society, Pittsburgh, PA (1995) 375.

[52] P. Simon, Y. Gogotsi, Materials for electrochemical capacitors, Nat Mater 7(11) (2008) 845-854.

[53] J.R. Miller, P. Simon, Electrochemical Capacitors for Energy Management, Science 321(5889) (2008) 651-652.

[54] W.C. West, M.C. Smart, E.J. Brandon, L.D. Whitcanack, G.A. Plett, Double-Layer Capacitor Electrolytes Using 1,3-D ioxolane for Low Temperature Operation, Journal of The Electrochemical Society 155(10) (2008) A716-A720.

[55] M. Mastragostino, C. Arbizzani, F. Soavi, Conducting polymers as electrode materials in supercapacitors, Solid State Ionics 148(3) (2002) 493-498.

[56] S.T. Senthilkumar, R.K. Selvan, J.S. Melo, Redox additive/active electrolytes: a novel approach to enhance the performance of supercapacitors, Journal of Materials Chemistry A 1(40) (2013) 12386-12394.

[57] M. Dahl, Y. Liu, Y. Yin, Composite Titanium Dioxide Nanomaterials, Chemical Reviews 114(19) (2014) 9853-9889.

[58] F. Cheng, J. Zhao, W. Song, C. Li, H. Ma, J. Chen, P. Shen, Facile controlled synthesis of MnO2 nanostructures of novel shapes and their application in batteries, Inorg Chem 45(5) (2006) 2038-44.

[59] M. Mastragostino, C. Arbizzani, R. Paraventi, A. Zanelli, Polymer Selection and Cell Design for Electric-Vehicle Supercapacitors, Journal of The Electrochemical Society 147(2) (2000) 407-412.

[60] S.-L. Kuo, N.-L. Wu, Investigation of Pseudocapacitive Charge-Storage Reaction of MnO2 · nH2O Supercapacitors in Aqueous Electrolytes, Journal of The Electrochemical Society 153(7) (2006) A1317-A1324.

[61] S.C. Pang, M.A. Anderson, T.W. Chapman, Novel Electrode Materials for Thin-Film Ultracapacitors: Comparison of Electrochemical Properties of Sol-Gel-Derived and Electrodeposited Manganese Dioxide, Journal of The Electrochemical Society 147(2) (2000) 444-450.

[62] M. Toupin, T. Brousse, D. Bélanger, Charge Storage Mechanism of MnO2 Electrode Used in Aqueous Electrochemical Capacitor, Chemistry of Materials 16(16) (2004) 3184-3190.

[63] G. Wang, L. Zhang, J. Zhang, A review of electrode materials for electrochemical supercapacitors, Chem Soc Rev 41(2) (2012) 797-828.

[64] J. Zhang, X.S. Zhao, On the configuration of supercapacitors for maximizing electrochemical performance, ChemSusChem 5(5) (2012) 818-41.

[65] F. Wang, S. Xiao, Y. Hou, C. Hu, L. Liu, Y. Wu, Electrode materials for aqueous asymmetric supercapacitors, RSC Advances 3(32) (2013) 13059-13084.

[66] A. Bazargan, Y. Yan, C.W. Hui, G. McKay, A Review: Synthesis of Carbon-Based Nano and Micro Materials by High Temperature and High Pressure, Industrial & Engineering Chemistry Research 52(36) (2013) 12689-12702.

[67] H. Zhang, X. Zhang, X. Sun, Y. Ma, Shape-controlled synthesis of nanocarbons through direct conversion of carbon dioxide, 3 (2013) 3534.

[68] M. Inagaki, CHAPTER 4 - Carbon Fibers, New Carbons - Control of Structure and Functions, Elsevier Science, Oxford, 2000, pp. 82-123.

[69] M. Inagaki, CHAPTER 5 - Porous Carbons, New Carbons - Control of Structure and Functions, Elsevier Science, Oxford, 2000, pp. 124-145.

[70] M. Inagaki, Creation of functional nano- and micro-spaces in carbon materials, Synth Metals 125 (2002) 139-266.

[71] M. Inagaki, L.R. Radovic, Nanocarbons, Carbon 40(12) (2002) 2279-2282.

[72] A.S. Fialkov, Carbon application in chemical power sources, Russian Journal of Electrochemistry 36(4) (2000) 345-366.

[73] https://www.google.com.sg/search?dcr=0&source=hp&ei=r4CoWru5LMPQ0AT-3rfACA&q=cost+of+grahite+&oq=cost+of+grahite+&gs_l=psy- Accessed on 11 March 2018.

[74] https://www.alibaba.com/product-detail/Graphite-Price-per-kg-per-ton_60591322371.html Accessed on 11 March 2018.

[75] https://nj-shunbo.en.made-in-china.com/product/ZCOQRLePfpVb/China-Graphite-Electrode-Pump-Synthetic-Graphite.html Accessed on 11 March 2018.

[76] https://www.alibaba.com/product-detail/Actived-Carbon_2008067467.html?spm=a2700.7735675.2017115.191.t646NF&s=p Accessed on 11 March 2018.

[77] https://www.alibaba.com/product-detail/Lowest-Price-wood-based-powder-activated_60378181889.html?spm=a2700.7735675.2017115.184.t646NF&s=p Accessed on 11 March 2018.

[78] https://www.alibaba.com/product-detail/Activated-carbon-coconut-activated-carbon-buyers_60652769211.html?spm=a2700.7735675.2017115.168.t646NF&s=p Accessed on 11 March 2018.

[79] http://markets.businessinsider.com/news/stocks/cru-graphite-electrode-prices-have-risen-sharply-due-to-supply-tightness-in-china-1002251145 Accessed on 11 March 2018.

[80] https://globenewswire.com/news-release/2018/01/04/1283386/0/en/Graphite-Electrodes-Market-Revenue-will-Reach-27-5-Billion-by-2022-Says-Esticast-Research-and-Consulting.html Accessed on 11 March 2018.

[81] M. Sevilla, A.B. Fuertes, R. Mokaya, High density hydrogen storage in superactivated carbons from hydrothermally carbonized renewable organic materials, Energy & Environmental Science 4(4) (2011) 1400-1410.

[82] S. Wenzhong, L. Zhijie, L. Yihong, Surface Chemical Functional Groups Modification of Porous Carbon, Recent Patents on Chemical Engineering 1(1) (2008) 27-40.

[83] C.-F. Chang, C.-Y. Chang, W.-T. Tsai, Effects of Burn-off and Activation Temperature on Preparation of Activated Carbon from Corn Cob Agrowaste by CO2 and Steam, Journal of colloid and interface science 232(1) (2000) 45-49.

[84] M.J. Lázaro, M.E. Gálvez, S. Artal, J.M. Palacios, R. Moliner, Preparation of steam-activated carbons as catalyst supports, Journal of Analytical and Applied Pyrolysis 78(2) (2007) 301-315.

[85] P. Kalyani, A. Anitha, Biomass carbon & its prospects in electrochemical energy systems, International Journal of Hydrogen Energy 38(10) (2013) 4034-4045.

[86] A. Jain, C. Xu, S. Jayaraman, R. Balasubramanian, J.Y. Lee, M.P. Srinivasan, Mesoporous activated carbons with enhanced porosity by optimal hydrothermal pre-treatment of biomass for supercapacitor applications, Microporous and Mesoporous Materials 218 (2015) 55-61.

[87] A.L. Cazetta, A.M.M. Vargas, E.M. Nogami, M.H. Kunita, M.R. Guilherme, A.C. Martins, T.L. Silva, J.C.G. Moraes, V.C. Almeida, NaOH-activated carbon of high surface area produced from coconut shell: Kinetics and equilibrium studies from the methylene blue adsorption, Chemical Engineering Journal 174(1) (2011) 117-125.

[88] W. Lv, F. Wen, J. Xiang, J. Zhao, L. Li, L. Wang, Z. Liu, Y. Tian, Peanut shell derived hard carbon as ultralong cycling anodes for lithium and sodium batteries, Electrochimica Acta 176 (2015) 533-541.

[89] A. Elmouwahidi, Z. Zapata-Benabithe, F. Carrasco-Marín, C. Moreno-Castilla, Activated carbons from KOH-activation of argan (Argania spinosa) seed shells as supercapacitor electrodes, Bioresource Technology 111 (2012) 185-190.

[90] I.I. Gurten, M. Ozmak, E. Yagmur, Z. Aktas, Preparation and characterisation of activated carbon from waste tea using K2CO3, Biomass and Bioenergy 37 (2012) 73-81.

[91] K.Y. Foo, B.H. Hameed, Mesoporous activated carbon from wood sawdust by K2CO3 activation using microwave heating, Bioresource Technology 111 (2012) 425-432.

[92] J. Deng, T. Xiong, F. Xu, M. Li, C. Han, Y. Gong, H. Wang, Y. Wang, Inspired by bread leavening: one-pot synthesis of hierarchically porous carbon for supercapacitors, Green Chemistry 17(7) (2015) 4053-4060.

[93] Y.J. Hwang, S.K. Jeong, J.S. Shin, K.S. Nahm, A.M. Stephan, High capacity disordered carbons obtained from coconut shells as anode materials for lithium batteries, Journal of Alloys and Compounds 448(1) (2008) 141-147.

[94] K.-l. Hong, L. Qie, R. Zeng, Z.-q. Yi, W. Zhang, D. Wang, W. Yin, C. Wu, Q.-j. Fan, W.-x. Zhang, Y.-h. Huang, Biomass derived hard carbon used as a high performance anode material for sodium ion batteries, Journal of Materials Chemistry A 2(32) (2014) 12733-12738.

[95] B. Xu, Y. Chen, G. Wei, G. Cao, H. Zhang, Y. Yang, Activated carbon with high capacitance prepared by NaOH activation for supercapacitors, Materials Chemistry and Physics 124(1) (2010) 504-509.

[96] L. wang, Z. Zhang, Y. Qu, Y. Guo, Z. Wang, X. Wang, A novel route for preparation of high-performance porous carbons from hydrochars by KOH activation, Colloids and Surfaces A: Physicochemical and Engineering Aspects 447 (2014) 183-187.

[97] Y. Lv, F. Zhang, Y. Dou, Y. Zhai, J. Wang, H. Liu, Y. Xia, B. Tu, D. Zhao, A comprehensive study on KOH activation of ordered mesoporous carbons and their supercapacitor application, Journal of Materials Chemistry 22(1) (2012) 93-99.

[98] M.J. Prauchner, F. Rodríguez-Reinoso, Chemical versus physical activation of coconut shell: A comparative study, Microporous and Mesoporous Materials 152 (2012) 163-171.

[99] M.M. Titirici, A. Thomas, S.-H. Yu, J.-O. Müller, M. Antonietti, A Direct Synthesis of Mesoporous Carbons with Bicontinuous Pore Morphology from Crude Plant Material by Hydrothermal Carbonization, Chemistry of Materials 19(17) (2007) 4205-4212.

[100] Z. Liu, F.-S. Zhang, Removal of lead from water using biochars prepared from hydrothermal liquefaction of biomass, Journal of Hazardous Materials 167(1–3) (2009) 933-939.

[101] M. Sevilla, A.B. Fuertes, The production of carbon materials by hydrothermal carbonization of cellulose, Carbon 47(9) (2009) 2281-2289.

[102] E. Frackowiak, F. Béguin, Carbon materials for the electrochemical storage of energy in capacitors, Carbon 39(6) (2001) 937-950.

[103] L. Wang, Y. Guo, B. Zou, C. Rong, X. Ma, Y. Qu, Y. Li, Z. Wang, High surface area porous carbons prepared from hydrochars by phosphoric acid activation, Bioresource Technology 102(2) (2011) 1947-1950.

[104] L. Wei, G. Yushin, Nanostructured activated carbons from natural precursors for electrical double layer capacitors, Nano Energy 1(4) (2012) 552-565.

[105] J. Mi, X.-R. Wang, R.-J. Fan, W.-H. Qu, W.-C. Li, Coconut-Shell-Based Porous Carbons with a Tunable Micro/Mesopore Ratio for High-Performance Supercapacitors, Energy & Fuels 26(8) (2012) 5321-5329.

[106] R. Wang, P. Wang, X. Yan, J. Lang, C. Peng, Q. Xue, Promising Porous Carbon Derived from Celtuce Leaves with Outstanding Supercapacitance and CO2 Capture Performance, ACS Applied Materials & Interfaces 4(11) (2012) 5800-5806.

[107] T.E. Rufford, D. Hulicova-Jurcakova, Z. Zhu, G.Q. Lu, Nanoporous carbon electrode from waste coffee beans for high performance supercapacitors, Electrochemistry Communications 10(10) (2008) 1594-1597.

[108] N. Sudhan, K. Subramani, M. Karnan, N. Ilayaraja, M. Sathish, Biomass-Derived Activated Porous Carbon from Rice Straw for a High-Energy Symmetric Supercapacitor in Aqueous and Non-aqueous Electrolytes, Energy & Fuels 31(1) (2017) 977-985.

[109] T.E. Rufford, D. Hulicova-Jurcakova, E. Fiset, Z. Zhu, G.Q. Lu, Double-layer capacitance of waste coffee ground activated carbons in an organic electrolyte, Electrochemistry Communications 11(5) (2009) 974-977.

[110] M.R. Jisha, Y.J. Hwang, J.S. Shin, K.S. Nahm, T. Prem Kumar, K. Karthikeyan, N. Dhanikaivelu, D. Kalpana, N.G. Renganathan, A.M. Stephan, Electrochemical characterization of supercapacitors based on carbons derived from coffee shells, Materials Chemistry and Physics 115(1) (2009) 33-39.

[111] V. Subramanian, C. Luo, A.M. Stephan, K.S. Nahm, S. Thomas, B. Wei, Supercapacitors from Activated Carbon Derived from Banana Fibers, The Journal of Physical Chemistry C 111(20) (2007) 7527-7531.

[112] D. Kalpana, S.H. Cho, S.B. Lee, Y.S. Lee, R. Misra, N.G. Renganathan, Recycled waste paper—A new source of raw material for electric double-layer capacitors, Journal of Power Sources 190(2) (2009) 587-591.

[113] M.S. Balathanigaimani, W.-G. Shim, M.-J. Lee, C. Kim, J.-W. Lee, H. Moon, Highly porous electrodes from novel corn grains-based activated carbons for electrical double layer capacitors, Electrochemistry Communications 10(6) (2008) 868-871.

[114] L. Wei, M. Sevilla, A.B. Fuertes, R. Mokaya, G. Yushin, Polypyrrole-Derived Activated Carbons for High-Performance Electrical Double-Layer Capacitors with Ionic Liquid Electrolyte, Advanced Functional Materials 22(4) (2012) 827-834.

[115] K. Jurewicz, K. Babeł, Efficient Capacitor Materials from Active Carbons Based on Coconut Shell/Melamine Precursors, Energy & Fuels 24(6) (2010) 3429-3435.

[116] X. Li, W. Xing, S. Zhuo, J. Zhou, F. Li, S.-Z. Qiao, G.-Q. Lu, Preparation of capacitor's electrode from sunflower seed shell, Bioresource Technology 102(2) (2011) 1118-1123.

[117] Y.-J. Kim, B.-J. Lee, H. Suezaki, T. Chino, Y. Abe, T. Yanagiura, K.C. Park, M. Endo, Preparation and characterization of bamboo-based activated carbons as electrode materials for electric double layer capacitors, Carbon 44(8) (2006) 1592-1595.

[118] C. Kim, J.-W. Lee, J.-H. Kim, K.-S. Yang, Feasibility of bamboo-based activated carbons for an electrochemical supercapacitor electrode, Korean Journal of Chemical Engineering 23(4) (2006) 592-594.

[119] F.-C. Wu, R.-L. Tseng, C.-C. Hu, C.-C. Wang, Physical and electrochemical characterization of activated carbons prepared from firwoods for supercapacitors, Journal of Power Sources 138(1–2) (2004) 351-359.

[120] L. Wei, M. Sevilla, A.B. Fuertes, R. Mokaya, G. Yushin, Hydrothermal Carbonization of Abundant Renewable Natural Organic Chemicals for High-Performance Supercapacitor Electrodes, Advanced Energy Materials 1(3) (2011) 356-361.

[121] S. Zhao, C.-Y. Wang, M.-M. Chen, J. Wang, Z.-Q. Shi, Potato starch-based activated carbon spheres as electrode material for electrochemical capacitor, Journal of Physics and Chemistry of Solids 70(9) (2009) 1256-1260.

[122] J. Yang, Y. Liu, X. Chen, Z. Hu, G. Zhao, Carbon Electrode Material with High Densities of Energy and Power, Acta Physico-Chimica Sinica 24(1) (2008) 13-19.

[123] F.-C. Wu, R.-L. Tseng, C.-C. Hu, C.-C. Wang, Effects of pore structure and electrolyte on the capacitive characteristics of steam- and KOH-activated carbons for supercapacitors, Journal of Power Sources 144(1) (2005) 302-309.

[124] C.-C. Hu, C.-C. Wang, F.-C. Wu, R.-L. Tseng, Characterization of pistachio shell-derived carbons activated by a combination of KOH and CO2 for electric double-layer capacitors, Electrochimica Acta 52(7) (2007) 2498-2505.

[125] T.E. Rufford, D. Hulicova-Jurcakova, K. Khosla, Z. Zhu, G.Q. Lu, Microstructure and electrochemical double-layer capacitance of carbon electrodes prepared by zinc chloride activation of sugar cane bagasse, Journal of Power Sources 195(3) (2010) 912-918.

[126] S. Wei-Jiang, W. Xiao-Zhong, X. Wei, Z. Jin, Z. Shu-Ping, Bagasse-based Nanoporous Carbon for Supercapacitor Application, ÎÞ»ú²ÄÁÏÑ§±¨ (2010).

[127] M. Olivares-Marín, J.A. Fernández, M.J. Lázaro, C. Fernández-González, A. Macías-García, V. Gómez-Serrano, F. Stoeckli, T.A. Centeno, Cherry stones as

precursor of activated carbons for supercapacitors, Materials Chemistry and Physics 114(1) (2009) 323-327.

[128] F.-C. Wu, R.-L. Tseng, C.-C. Hu, C.-C. Wang, The capacitive characteristics of activated carbons—comparisons of the activation methods on the pore structure and effects of the pore structure and electrolyte on the capacitive performance, Journal of Power Sources 159(2) (2006) 1532-1542.

[129] C.S.K. Lin, L.A. Pfaltzgraff, L. Herrero-Davila, E.B. Mubofu, S. Abderrahim, J.H. Clark, A.A. Koutinas, N. Kopsahelis, K. Stamatelatou, F. Dickson, S. Thankappan, Z. Mohamed, R. Brocklesby, R. Luque, Food waste as a valuable resource for the production of chemicals, materials and fuels. Current situation and global perspective, Energy & Environmental Science 6(2) (2013) 426-464.

[130] J. Gustavsson, U. Cederberg, C. Sonesson, R. van Otterdijk, A. Meybeck, Global food losses and food waste: extent, causes and prevention, Food and Agriculture Organization (FAO) of the United Nations, available at: http://large.stanford.edu/courses/2012/ph240/briggs1/docs/mb060e00.pdf (2011).

[131] "Global Food Loss and Food Waste", UN Food and Agricultural Organisation (FAO), http://www.fao.org/food-loss-and-food-waste/en/.

[132] http://www.nea.gov.sg/energy-waste/waste-management/waste-statistics-and-overall-recycling. Accessed on 25 February 2018.

[133] https://watchmywaste.com.au/food-waste-greenhouse-gas-calculator/. Accessed on 25 February 2018.

[134] A.M. Balu, V. Budarin, P.S. Shuttleworth, L.A. Pfaltzgraff, K. Waldron, R. Luque, J.H. Clark, Valorisation of Orange Peel Residues: Waste to Biochemicals and Nanoporous Materials, ChemSusChem 5(9) (2012) 1694-1697.

[135] C.M. Galanakis, Recovery of high added-value components from food wastes: Conventional, emerging technologies and commercialized applications, Trends in Food Science & Technology 26(2) (2012) 68-87.

[136] Y. Abu-Rukah, O. Al-Kofahi, The assessment of the effect of landfill leachate on ground-water quality—a case study. El-Akader landfill site—north Jordan, Journal of Arid Environments 49(3) (2001) 615-630.

[137] M. Schuhmacher, J.L. Domingo, Long-term study of environmental levels of dioxins and furans in the vicinity of a municipal solid waste incinerator, Environment International 32(3) (2006) 397-404.

[138] M. Lorber, P. Pinsky, P. Gehring, C. Braverman, D. Winters, W. Sovocool, Relationships between dioxins in soil, air, ash, and emissions from a municipal solid waste incinerator emitting large amounts of dioxins, Chemosphere 37(9–12) (1998) 2173-2197.

[139] A. Bernstad, J. la Cour Jansen, Review of comparative LCAs of food waste management systems – Current status and potential improvements, Waste Management 32(12) (2012) 2439-2455.

[140] J. Huet, C. Druilhe, A. Trémier, J.C. Benoist, G. Debenest, The impact of compaction, moisture content, particle size and type of bulking agent on initial physical properties of sludge-bulking agent mixtures before composting, Bioresource Technology 114(0) (2012) 428-436.

[141] H.H. Khoo, T.Z. Lim, R.B.H. Tan, Food waste conversion options in Singapore: Environmental impacts based on an LCA perspective, Science of The Total Environment 408(6) (2010) 1367-1373.

[142] U. Sonesson, A. Björklund, M. Carlsson, M. Dalemo, Environmental and economic analysis of management systems for biodegradable waste, Resources, Conservation and Recycling 28(1–2) (2000) 29-53.

[143] M. Takata, K. Fukushima, N. Kino-Kimata, N. Nagao, C. Niwa, T. Toda, The effects of recycling loops in food waste management in Japan: Based on the environmental and economic evaluation of food recycling, Science of The Total Environment 432(0) (2012) 309-317.

[144] https://www.statista.com/topics/1621/fruit-production/ Accessed on 11 March 2018.

[145] Citrus Fruit - Fresh and Processed Statistical Bulletin 2016, Food and Agriculture Organization of the United Nations (FAO), 2017. Accessed on 11 March 2018.

[146] M.E. Fernandez, G.V. Nunell, P.R. Bonelli, A.L. Cukierman, Activated carbon developed from orange peels: Batch and dynamic competitive adsorption of basic dyes, Industrial Crops and Products 62 (2014) 437-445.

[147] K. Sun, H. Wang, H. Peng, Y. Wu, G. Ma, Z. Lei, Manganese oxide nanorods supported on orange peel-based carbon nanosheets for high performance supercapacitors, Int. J. Electrochem. Sci 10 (2015) 2000-2013.

[148] M. Thirumavalavan, Y.-L. Lai, J.-F. Lee, Fourier Transform Infrared Spectroscopic Analysis of Fruit Peels before and after the Adsorption of Heavy Metal Ions from Aqueous Solution, Journal of Chemical & Engineering Data 56(5) (2011) 2249-2255.

[149] M.E. Fernandez, B. Ledesma, S. Román, P.R. Bonelli, A.L. Cukierman, Development and characterization of activated hydrochars from orange peels as potential adsorbents for emerging organic contaminants, Bioresource Technology 183 (2015) 221-228.

[150] K.Y. Foo, B.H. Hameed, Preparation, characterization and evaluation of adsorptive properties of orange peel based activated carbon via microwave induced K2CO3 activation, Bioresource Technology 104 (2012) 679-686.

[151] F.-M. Pellera, A. Giannis, D. Kalderis, K. Anastasiadou, R. Stegmann, J.-Y. Wang, E. Gidarakos, Adsorption of Cu(II) ions from aqueous solutions on biochars prepared from agricultural by-products, Journal of Environmental Management 96(1) (2012) 35-42.

[152] A.B. Pérez-Marín, A. Ballester, F. González, M.L. Blázquez, J.A. Muñoz, J. Sáez, V.M. Zapata, Study of cadmium, zinc and lead biosorption by orange wastes using the subsequent addition method, Bioresource Technology 99(17) (2008) 8101-8106.

[153] A.B. Pérez-Marín, V.M. Zapata, J.F. Ortuño, M. Aguilar, J. Sáez, M. Lloréns, Removal of cadmium from aqueous solutions by adsorption onto orange waste, Journal of Hazardous Materials 139(1) (2007) 122-131.

[154] A.E. Nemr, O. Abdelwahab, A. El-Sikaily, A. Khaled, Removal of direct blue-86 from aqueous solution by new activated carbon developed from orange peel, Journal of Hazardous Materials 161(1) (2009) 102-110.

[155] A. Prasannan, T. Imae, One-Pot Synthesis of Fluorescent Carbon Dots from Orange Waste Peels, Industrial & Engineering Chemistry Research 52(44) (2013) 15673-15678.

[156] A.A. Arie, J.K. Lee, Activated Carbons from Orange Peel Waste as Supercapacitor Electrodes, Meeting Abstracts MA2013-01(11) (2013) 556.

[157] A. Bhatnagar, A.K. Minocha, Assessment of the biosorption characteristics of lychee (Litchi chinensis) peel waste for the removal of Acid Blue 25 dye from water, Environ Technol 31(1) (2010) 97-105.

[158] M. Ramananda Singh, P. Gupta, K. Gupta, The litchi (Litchi Chinensis) peels extract as a potential green inhibitor in prevention of corrosion of mild steel in 0.5M H2SO4 solution, Arabian Journal of Chemistry (2015).

[159] M. Thirumavalavan, Y.L. Lai, J.F. Lee, Fourier Transform Infrared Spectroscopic Analysis of Fruit Peels before and after the Adsorption of Heavy Metal Ions from Aqueous Solution, Journal of Chemical and Engineering Data 56(5) (2011) 2249-2255.

[160] http://www.ippa.info/commercial_production_of_pectin.htm Accessed on 25 February 2018

[161] B. Chen, Z. Chen, Sorption of naphthalene and 1-naphthol by biochars of orange peels with different pyrolytic temperatures, Chemosphere 76(1) (2009) 127-133.

[162] K.Y. Foo, B.H. Hameed, Preparation of activated carbon by microwave heating of langsat (Lansium domesticum) empty fruit bunch waste, Bioresource Technology 116 (2012) 522-525.

[163] A.A. Khan, W. de Jong, P.J. Jansens, H. Spliethoff, Biomass combustion in fluidized bed boilers: Potential problems and remedies, Fuel Processing Technology 90(1) (2009) 21-50.

[164] S. Vyazovkin, K. Chrissafis, M.L. Di Lorenzo, N. Koga, M. Pijolat, B. Roduit, N. Sbirrazzuoli, J.J. Suñol, ICTAC Kinetics Committee recommendations for collecting experimental thermal analysis data for kinetic computations, Thermochimica Acta 590 (2014) 1-23.

[165] Y. Sudaryanto, S.B. Hartono, W. Irawaty, H. Hindarso, S. Ismadji, High surface area activated carbon prepared from cassava peel by chemical activation, Bioresource Technology 97(5) (2006) 734-739.

[166] P. Sennu, V. Aravindan, M. Ganesan, Y.-G. Lee, Y.-S. Lee, Biomass-Derived Electrode for Next Generation Lithium-Ion Capacitors, ChemSusChem 9(8) (2016) 849-854.

[167] A. Stein, Z. Wang, M.A. Fierke, Functionalization of Porous Carbon Materials with Designed Pore Architecture, Advanced Materials 21(3) (2009) 265-293.

[168] P. Sennu, H.-J. Choi, S.-G. Baek, V. Aravindan, Y.-S. Lee, Tube-like carbon for Li-ion capacitors derived from the environmentally undesirable plant: Prosopis juliflora, Carbon 98 (2016) 58-66.

[169] Q. Wang, L. Jiao, H. Du, Y. Si, Y. Wang, H. Yuan, Co3S4 hollow nanospheres grown on graphene as advanced electrode materials for supercapacitors, Journal of Materials Chemistry 22(40) (2012) 21387-21391.

[170] G. Wang, J. Zhang, S. Kuang, S. Liu, S. Zhuo, The production of cobalt sulfide/graphene composite for use as a low-cost counter-electrode material in dye-sensitized solar cells, Journal of Power Sources 269 (2014) 473-478.

[171] H.D. Yoo, E. Markevich, G. Salitra, D. Sharon, D. Aurbach, On the challenge of developing advanced technologies for electrochemical energy storage and conversion, Materials Today 17(3) (2014) 110-121.

[172] B. Dunn, H. Kamath, J.-M. Tarascon, Electrical Energy Storage for the Grid: A Battery of Choices, Science 334(6058) (2011) 928-935.

[173] P. Alotto, M. Guarnieri, F. Moro, Redox flow batteries for the storage of renewable energy: A review, Renewable and Sustainable Energy Reviews 29 (2014) 325-335.

[174] G. Kear, A.A. Shah, F.C. Walsh, Development of the all-vanadium redox flow battery for energy storage: a review of technological, financial and policy aspects, International Journal of Energy Research 36(11) (2012) 1105-1120.

[175] C. Yao, H. Zhang, T. Liu, X. Li, Z. Liu, Carbon paper coated with supported tungsten trioxide as novel electrode for all-vanadium flow battery, Journal of Power Sources 218 (2012) 455-461.

[176] S. Winardi, S.C. Raghu, M.O. Oo, Q. Yan, N. Wai, T.M. Lim, M. Skyllas-Kazacos, Sulfonated poly (ether ether ketone)-based proton exchange membranes for vanadium redox battery applications, Journal of Membrane Science 450 (2014) 313-322.

[177] A. Bhattarai, N. Wai, R. Schweiss, A. Whitehead, T.M. Lim, H.H. Hng, Advanced porous electrodes with flow channels for vanadium redox flow battery, Journal of Power Sources 341 (2017) 83-90.

[178] M. Sevilla, R. Mokaya, Energy storage applications of activated carbons: supercapacitors and hydrogen storage, Energy & Environmental Science 7(4) (2014) 1250-1280.

[179] G.K. Parshetti, S. Chowdhury, R. Balasubramanian, Biomass derived low-cost microporous adsorbents for efficient CO2 capture, Fuel 148 (2015) 246-254.

[180] W. Li, J. Liu, C. Yan, The electrochemical catalytic activity of single-walled carbon nanotubes towards VO2+/VO2+ and V3+/V2+ redox pairs for an all vanadium redox flow battery, Electrochimica Acta 79 (2012) 102-108.

[181] C. Flox, M. Skoumal, J. Rubio-Garcia, T. Andreu, J.R. Morante, Strategies for enhancing electrochemical activity of carbon-based electrodes for all-vanadium redox flow batteries, Applied Energy 109 (2013) 344-351.

[182] W.N.-F. SU An-Qun, LIU Su-Qin, WU Tao, PENG Sui, Modification of Carbon Paper Electrode via Hydrothermal Oxidation Applied in the Vanadium Redox Battery, Acta Phys. -Chim. Sin., 2012, pp. 1387-1392.

[183] Z. Wang, L. Qie, L. Yuan, W. Zhang, X. Hu, Y. Huang, Functionalized N-doped interconnected carbon nanofibers as an anode material for sodium-ion storage with excellent performance, Carbon 55 (2013) 328-334.

[184] W. Li, D. Chen, Z. Li, Y. Shi, Y. Wan, J. Huang, J. Yang, D. Zhao, Z. Jiang, Nitrogen enriched mesoporous carbon spheres obtained by a facile method and its application for electrochemical capacitor, Electrochemistry Communications 9(4) (2007) 569-573.

[185] A. Laheäär, S. Delpeux-Ouldriane, E. Lust, F. Béguin, Ammonia Treatment of Activated Carbon Powders for Supercapacitor Electrode Application, Journal of The Electrochemical Society 161(4) (2014) A568-A575.

[186] K. Jurewicz, K. Babeł, A. Źiółkowski, H. Wachowska, Ammoxidation of active carbons for improvement of supercapacitor characteristics, Electrochimica Acta 48(11) (2003) 1491-1498.

[187] K. Okajima, K. Ohta, M. Sudoh, Capacitance behavior of activated carbon fibers with oxygen-plasma treatment, Electrochimica Acta 50(11) (2005) 2227-2231.

[188] S.W. Lee, N. Yabuuchi, B.M. Gallant, S. Chen, B.-S. Kim, P.T. Hammond, Y. Shao-Horn, High-power lithium batteries from functionalized carbon-nanotube electrodes, Nat Nano 5(7) (2010) 531-537.

[189] C.-T. Hsieh, H. Teng, Influence of oxygen treatment on electric double-layer capacitance of activated carbon fabrics, Carbon 40(5) (2002) 667-674.

[190] B. Sun, M. Skyllas-Kazakos, Chemical modification and electrochemical behaviour of graphite fibre in acidic vanadium solution, Electrochimica Acta 36(3–4) (1991) 513-517.

[191] C. Liu, B.B. Koyyalamudi, L. Li, S. Emani, C. Wang, L.L. Shaw, Improved capacitive energy storage via surface functionalization of activated carbon as cathodes for lithium ion capacitors, Carbon 109 (2016) 163-172.

[192] H. Oda, A. Yamashita, S. Minoura, M. Okamoto, T. Morimoto, Modification of the oxygen-containing functional group on activated carbon fiber in electrodes of an electric double-layer capacitor, Journal of Power Sources 158(2) (2006) 1510-1516.

[193] S.M. SANIP, A.F. ISMAIL, P.S. GOH, B.C. NG, M.S. ABDULLAH, T. SOGA, M. TANEMURA, H. YASUHIKO, PREPARATION AND

CHARACTERISTICS OF FUNCTIONALIZED MULTIWALLED CARBON NANOTUBES IN POLYIMIDE MIXED MATRIX MEMBRANE, Nano 05(04) (2010) 195-202.

[194] G. Lota, J. Tyczkowski, R. Kapica, K. Lota, E. Frackowiak, Carbon materials modified by plasma treatment as electrodes for supercapacitors, Journal of Power Sources 195(22) (2010) 7535-7539.

[195] T.A. Centeno, F. Stoeckli, The role of textural characteristics and oxygen-containing surface groups in the supercapacitor performances of activated carbons, Electrochimica Acta 52(2) (2006) 560-566.

[196] S. Storck, H. Bretinger, W.F. Maier, Characterization of micro- and mesoporous solids by physisorption methods and pore-size analysis, Applied Catalysis A: General 174(1–2) (1998) 137-146.

[197] A. Jänes, H. Kurig, E. Lust, Characterisation of activated nanoporous carbon for supercapacitor electrode materials, Carbon 45(6) (2007) 1226-1233.

[198] F. Tuinstra, J.L. Koenig, Raman Spectrum of Graphite, The Journal of Chemical Physics 53(3) (1970) 1126-1130.

[199] X. Rui, A. Parasuraman, W. Liu, D.H. Sim, H.H. Hng, Q. Yan, T.M. Lim, M. Skyllas-Kazacos, Functionalized single-walled carbon nanotubes with enhanced electrocatalytic activity for Br-/Br3- redox reactions in vanadium bromide redox flow batteries, Carbon 64 (2013) 464-471.

[200] B. Sun, M. Skyllas-Kazacos, Chemical modification of graphite electrode materials for vanadium redox flow battery application—part II. Acid treatments, Electrochimica Acta 37(13) (1992) 2459-2465.

[201] L. Yue, W. Li, F. Sun, L. Zhao, L. Xing, Highly hydroxylated carbon fibres as electrode materials of all-vanadium redox flow battery, Carbon 48(11) (2010) 3079-3090.

[202] S.M. Taylor, A. Pătru, E. Fabbri, T.J. Schmidt, Influence of surface oxygen groups on V(II) oxidation reaction kinetics, Electrochemistry Communications 75 (2017) 13-16.

[203] S. Rudolph, U. Schröder, I.M. Bayanov, D. Hage, Measurement, simulation and in situ regeneration of energy efficiency in vanadium redox flow battery, Journal of Electroanalytical Chemistry 728 (2014) 72-80.

[204] S. Corcuera, M. Skyllas-Kazacos, State-of-charge monitoring and electrolyte rebalancing methods for the vanadium redox flow battery, Eur. Chem. Bull. 1(12) (2012) 511-519.

[205] H. Tamai, M. Kunihiro, M. Morita, H. Yasuda, Mesoporous activated carbon as electrode for electric double layer capacitor, Journal of Materials Science 40(14) (2005) 3703-3707.

[206] P. Simon, Y. Gogotsi, Materials for electrochemical capacitors, Nature Materials 7(11) (2008) 845-54.

[207] X. Xia, Y. Zhang, Z. Fan, D. Chao, Q. Xiong, J. Tu, H. Zhang, H.J. Fan, Novel Metal@Carbon Spheres Core–Shell Arrays by Controlled Self-Assembly of Carbon Nanospheres: A Stable and Flexible Supercapacitor Electrode, Advanced Energy Materials 5(6) (2015) n/a-n/a.

[208] X. Xia, Y. Zhang, D. Chao, C. Guan, Y. Zhang, L. Li, X. Ge, I.M. Bacho, J. Tu, H.J. Fan, Solution synthesis of metal oxides for electrochemical energy storage applications, Nanoscale 6(10) (2014) 5008-5048.

[209] X.H. Xia, D.L. Chao, Y.Q. Zhang, Z.X. Shen, H.J. Fan, Three-dimensional graphene and their integrated electrodes, Nano Today 9(6) (2014) 785-807.

[210] V. Aravindan, J. Gnanaraj, Y.S. Lee, S. Madhavi, Insertion-type electrodes for nonaqueous Li-ion capacitors, Chemical Reviews 114(23) (2014) 11619-11635.

[211] K. Naoi, Y. Nagano, Li-Ion-Based Hybrid Supercapacitors in Organic Medium, Supercapacitors, Wiley-VCH Verlag GmbH & Co. KGaA, Weinheim, Germany, 2013, pp. 239-256.

[212] Y. Zhong, X. Xia, F. Shi, J. Zhan, J. Tu, H.J. Fan, Transition Metal Carbides and Nitrides in Energy Storage and Conversion, Advanced Science 3(5) (2016) n/a-n/a.

[213] E. Raymundo-Piñero, K. Kierzek, J. Machnikowski, F. Béguin, Relationship between the nanoporous texture of activated carbons and their capacitance properties in different electrolytes, Carbon 44(12) (2006) 2498-2507.

[214] C. Peng, X.-b. Yan, R.-t. Wang, J.-w. Lang, Y.-j. Ou, Q.-j. Xue, Promising activated carbons derived from waste tea-leaves and their application in high performance supercapacitors electrodes, Electrochimica Acta 87 (2013) 401-408.

[215] D. Momodu, M. Madito, F. Barzegar, A. Bello, A. Khaleed, O. Olaniyan, J. Dangbegnon, N. Manyala, Activated carbon derived from tree bark biomass with promising material properties for supercapacitors, Journal of Solid State Electrochemistry (2016) 1-14.

[216] A. Jain, V. Aravindan, S. Jayaraman, P.S. Kumar, R. Balasubramanian, S. Ramakrishna, S. Madhavi, M. Srinivasan, Activated carbons derived from coconut shells as high energy density cathode material for Li-ion capacitors, Scientific reports 3 (2013) Art 3002.

[217] J.J. Ren, L.W. Su, X. Qin, M. Yang, J.P. Wei, Z. Zhou, P.W. Shen, Pre-lithiated graphene nanosheets as negative electrode materials for Li-ion capacitors with high power and energy density, Journal of Power Sources 264 (2014) 108-113.

[218] J.H. Lee, W.H. Shin, M.-H. Ryou, J.K. Jin, J. Kim, J.W. Choi, Functionalized Graphene for High Performance Lithium Ion Capacitors, ChemSusChem 5(12) (2012) 2328-2333.

[219] W.J. Cao, J.P. Zheng, Li-ion capacitors with carbon cathode and hard carbon/stabilized lithium metal powder anode electrodes, Journal of Power Sources 213 (2012) 180-185.

[220] J. Yan, T. Wei, B. Shao, F. Ma, Z. Fan, M. Zhang, C. Zheng, Y. Shang, W. Qian, F. Wei, Electrochemical properties of graphene nanosheet/carbon black composites as electrodes for supercapacitors, Carbon 48(6) (2010) 1731-1737.

[221] A.K. Shukla, P.V. Kamath, Energy storage and retrieval, Resonance 1(6) (1996) 61-68.

[222] Y. Gogotsi, Not just graphene: The wonderful world of carbon and related nanomaterials, MRS Bulletin 40(12) (2015) 1110-1121.

[223] G.A. Snook, P. Kao, A.S. Best, Conducting-polymer-based supercapacitor devices and electrodes, Journal of Power Sources 196(1) (2011) 1-12.

[224] W.-C. Chen, T.-C. Wen, H. Teng, Polyaniline-deposited porous carbon electrode for supercapacitor, Electrochimica Acta 48(6) (2003) 641-649.

[225] M.J. Bleda-Martínez, E. Morallón, D. Cazorla-Amorós, Polyaniline/porous carbon electrodes by chemical polymerisation: Effect of carbon surface chemistry, Electrochimica Acta 52(15) (2007) 4962-4968.

[226] Y.-R. Lin, H. Teng, A novel method for carbon modification with minute polyaniline deposition to enhance the capacitance of porous carbon electrodes, Carbon 41(14) (2003) 2865-2871.

[227] H. Tamai, M. Hakoda, T. Shiono, H. Yasuda, Preparation of polyaniline coated activated carbon and their electrode performance for supercapacitor, Journal of Materials Science 42(4) (2007) 1293-1298.

[228] Q. Wang, J.-l. Li, F. Gao, W.-s. Li, K.-z. Wu, X.-d. Wang, Activated carbon coated with polyaniline as an electrode material in supercapacitors, New Carbon Materials 23(3) (2008) 275-280.

[229] Z.-H. Zhou, N.-C. Cai, Y. Zeng, Y.-H. Zhou, In situ Chemical Deposition of Polyaniline on Activated Carbon for Electrochemical Capacitors, Chinese Journal of Chemistry 24(1) (2006) 13-16.

[230] J.H. Park, O.O. Park, Hybrid electrochemical capacitors based on polyaniline and activated carbon electrodes, Journal of Power Sources 111(1) (2002) 185-190.

[231] L.L. Xinhong zhou, Shanmu Dong, Xiao Chen, A renewable bamboo carbon/polyaniline composite for a high-performance supercapacitor electrode material, Journal of Solid State Electrochemistry (2012).

[232] X. Li, L. Yang, Y. Lei, L. Gu, D. Xiao, Microwave-Assisted Chemical-Vapor-Induced in Situ Polymerization of Polyaniline Nanofibers on Graphite Electrode for High-Performance Supercapacitor, ACS Applied Materials & Interfaces 6(22) (2014) 19978-19989.

[233] X. zhou, L. Li, S. Dong, X. Chen, P. Han, H. Xu, J. Yao, C. Shang, Z. Liu, G. Cui, A renewable bamboo carbon/polyaniline composite for a high-performance supercapacitor electrode material, Journal of Solid State Electrochemistry 16(3) (2012) 877-882.